eXPRESS Polymer Letters Vol.4, No.5 (2010) 263
Available online at www.expresspolymlett.com
DOI: 10.3144/expresspolymlett.2010.33

Editorial corner – a personal view
Electrospinning a feasible nanotechnology

*Gy. Marosi**

Organic Chemistry and Technology Department of Budapest University of Technology and Economics, H-1111 Budapest, Műegyetem rkp. 3, Hungary

Electrospinning is the best example how a mature technology can rejuvenate when its right time arrives. The electrospinning method was born in 1902, when the simultaneous stretching and drying of polymer solution under the drawing force of electrostatic field was invented. Even the solvent-free melt alternative of the process was invented already in 1936. However, as the electrospinning method could not compete with the mass production technologies of fabrics, it was almost forgotten. The single exception was the military application of electrospun size exclusion membranes for removal of bacteria from infected water. The rejuvenation started in the nineties parallel with the increasing importance of nanotechnology. Comparing to the creation of other nanoobjects the productivity of continuous nanofiber formation by electrospinning is quite high. Therefore a wide range of potential applications for electrospun nanofiber and related assemblies has been identified, and increased exponentially. Nanofibers mimic the extracellular matrices (fibrous proteins) of living organisms. This similarity initiated the development of medical tools for tissue engineering and wound dressing made of polymer nanofibers including or covered with bioactive molecules, such as collagen, that support cell adhesion and proliferation. Drug delivery can utilize gelatine and other biodegradable nanofibers of hollow or core-shell structure. Enzymes immobilized on electrospun scaffolds catalyze the relevant biochemical processes. Rapid prototyping uses composite (such as hydroxyapatite containing) nanofibers for forming implant materials. Electrospun polyamide and polyacrylonitrile with carbon-nanotube content are used as conductive electronic units and similar composite nanofiber sensors of high absorbed-gas sensitivity are used for electronic nose application. Nanofibers of $LiFePO_4$/C content act as cathode material for Li-ion batteries. Electrospinning of emulsions, owing to drop breakup, results in fine distribution of the dispersed phases. Nanofibers in traditional composites may contribute to reinforcement and render them multifunctional (flame, chemical, environmental protection). These possibilities initiate development of new devices for mass-production of nanofibers.

Prof. Dr. György Marosi
Member of International Advisory Board

*Corresponding author, e-mail: gmarosi@mail.bme.hu

eXPRESS Polymer Letters Vol.4, No.5 (2010) 264–274
Available online at www.expresspolymlett.com
DOI: 10.3144/expresspolymlett.2010.34

Polyethylene/synthetic boehmite alumina nanocomposites: Structure, thermal and rheological properties

V. M. Khumalo[1], *J. Karger-Kocsis*[1,2*], *R. Thomann*[3]

[1]Department of Polymer Technology, Faculty of Mechanical Engineering and Built Environment, Tshwane University of Technology, Pretoria 0001, Republic of South Africa
[2]Department of Polymer Engineering, Faculty of Mechanical Engineering, Budapest University of Technology and Economics, H-1111 Budapest, Hungary
[3]Institut für Makromolekulare Chemie und Freiburger Materialforschungszentrum, Albert-Ludwigs-Universität Freiburg, Stefan-Meier-Str. 31, D-79104 Freiburg, Germany

Received 9 February 2010; accepted in revised form 4 March 2010

Abstract. Synthetic boehmite alumina (BA) has been incorporated up to 8 wt% in low density polyethylene (LDPE) and high density polyethylene (HDPE), respectively, by melt compounding. The primary nominal particle size of these two BA grades was 40 and 60 nm, respectively. The dispersion of the BA in polyethylene (PE) matrices was investigated by scanning and transmission electron microscopy techniques (SEM and TEM). The thermal (melting and crystallization), thermooxidative (oxidation induction temperature and time), and rheological behaviors of the nanocomposites were determined. It was found that BA is nanoscale dispersed in both LDPE and HDPE without any surface treatment and additional polymeric compatibilizer. BA practically did not influence the thermal (melting and crystallization) and rheological properties of the parent PEs. On the other hand, BA worked as a powerful thermooxidative stabilizer for LDPE, and especially for HDPE nanocomposites.

Keywords: *nanocomposite, polyethylene, boehmite alumina, thermooxidative stability, nanoparticle dispersion*

1. Introduction

Nowadays considerable research efforts are dedicated to produce nanocomposites with improved and/or novel properties compared to the unfilled versions. The nanofillers are either preformed (available initially in nm size range) or produced *in situ* via suitable methods (e.g. sol-gel chemistry, exfoliation of micrometer-sized agglomerates) [1]. Many of the nanofillers are of polar character which can be poorly dispersed in apolar thermoplastics, like polyethylene (PE) and polypropylene (PP). In order to enhance the dispersibility of the nanofillers in polyolefins their surfaces have to be modified by physical (e.g. stearic acid) and chemical treatments (e.g. silane grafting). An alternative and widely practiced way is to use polar polymers as compatibilizers for polyolefin/nanofiller systems. They are usually copolymers in linear and grafted forms. Introduction of compatibilizers is associated, however, with additional costs. Accordingly, researchers are looking for such nanofillers which can be easily and well dispersed without surface treatment and/or additional use of compatibilizers.

Synthetic boehmite alumina (BA) is a very promising candidate in this respect. Its primary particle size is in the range of tens of nanometer. The BA agglomerates can be broken up during melt com-

*Corresponding author, e-mail: karger@pt.bme.hu

pounding as shown recently in case of PP [2, 3]. It is noteworthy that BA is water dispersible and its particles became individually dispersed in the related aqueous media. Siengchin et al. made use of this property of BA and performed water-mediated melt compounding of BA with polyoxymethylene [4], polyamide-6 [5] and PP-based thermoplastic elastomer [6]. The BA, dispersed in water, was introduced in the molten polymer and subsequently evaporated. The latter was facilitated by the screw design of the extruder and by the additional use of a vacuum pump. The dispersion degree of BA was somewhat better for water-mediated than for traditional melt compounding in case of the thermoplastic elastomer [6]. This is a further proof that BA can well be incorporated without any treatment and additional polymeric additive in polyolefins.

BA with the chemical composition of AlO(OH) can be produced in particulates with different aspect ratios. The aspect ratio is increasing according to the ranking: platelet- < rod- < needle-like. The reinforcing and property modification potential of micro- and nanometer-scaled BA, with and without additional surface treatment, has been already checked in various thermoplastics (e.g. [2–13]).

Polyethylenes (PEs) were often modified in the past with nanofillers, like layered silicates in order to improve their mechanical, and especially barrier properties. BA was already incorporated in PE, however, mostly via *in situ* polymerization (i.e. BA served as catalyst support) [14–16]. By this method BA could well be dispersed in PE at very high concentration (up to 40 wt%) .This concentrate was used as PE/BA masterbatch in follow up melt compounding operations [15]. However, compared to studies devoted to PP/BA nanocomposites, less work addressed the effects of BA in polyethylene-based systems.

Accordingly, the present work was aimed at studying the effects of BA in PEs. In order to get a deeper understanding on the structure-property relationships in the related nanocomposites two BA grades and two PE types, viz. low- (LDPE) and high-density PE (HDPE), were involved in this study. The low aspect ratio (platelet-shaped) BA was not surface-modified and its content in the PEs was varied between 0 and 8 wt%.

2. Experimental

2.1. Materials

Disperal® 40 and Disperal® 80 grades of Sasol GmbH (Hamburg, Germany) were used as BA nanofillers. Their characteristics are listed in Table 1.

Table 1. Characteristics of the BAs used

Property	Unit	Disperal® 40	Disperal® 80
Al_2O_3 - content	[%]	82.5	83.4
Surface area	[m^2/g]	105.0	88.0
Loose bulk density	[g/cm^3]	0.57	0.38
Particle size: < 25 μm	[%]	21.0	48.6
Particle size: < 45 μm	[%]	45.4	80.7
Particle size < 90 μm	[%]	92.3	100.0
Crystallite size (021)	[nm]	39.6	74.4
Pore volume total	[ml/g]	0.700	0.870
Median pore size	[nm]	23.3	N/A

LDPE grade LT388 (melt flow index at 190°C/2.16 kg: 10 dg/min; density: 0.922 g/cm^3) from Sasol (Sasolburg, South Africa) and HDPE grade F 7740F2 (melt flow index at 190°C/2.16 kg: 0.4 dg/min; density: 0.946 g/cm^3) from Safripol (Bryanston, South Africa) were used throughout this study.

2.2. Preparation of nanocomposites

Samples of HDPE and LDPE with BA were prepared via melt mixing using a Haake Rheomix OS internal mixer equipped with Polylab OS RheoDrive4 (Thermo Fischer Scientific, Karlsruhe, Germany). Mixing occurred for 8 min at 175°C at 60 rpm for both PEs. Sheets of ca. 2 mm thickness have been produced by compression molding using a Carver press (Wabash, Indiana, USA). The temperature agreed with that of the mixing (=175°C) and the pressure was set for 2 MPa. After ca. 5 min holding time the press was cooled by water and the sheets were demolded.

2.3. Testing

2.3.1. BA dispersion

The dispersion state of the BA particles in the PEs was studied by scanning electron microscopy (SEM) using a FEI Quanta 250 FEG device (FEI, Hillsboro, Oregon, USA). Specimens were cryomicrotomed with a Diatome diamond knife at T = –120°C using a Leica EM UC6 ultramicrotome

equipped with a cryo-chamber. The cryocut surfaces of the specimens were inspected in SEM (acceleration voltage 5 kV) without sputtering, using a high resolution vCD detector for backscattered electrons. The morphology of the samples was also studied in a transmission electron microscope (TEM). The TEM device (Zeiss LEO 912 Omega, Oberkochen, Germany) was working at an acceleration voltage of 120 kV. Thin specimens (ca. 50 nm), prepared by cryocutting with the above ultramicrotome at $T = -120$°C, were subjected to TEM investigations without any staining.

2.3.2. Thermal properties (melting and crystallization)

Differential scanning calorimetric (DSC) tests were run on a PerkinElmer DSC Q2000 (Exton, PA, USA) in the temperature range of 50–200°C. The heating and cooling rates were 20°C/min. The melting peak temperature (T_m), melting enthalpy (ΔH_m), crystallization peak temperature (T_c) and crystallization enthalpy (ΔH_c) were determined. For the 100% crystalline PE a melting enthalpy of ΔH_m = 293 J/g [17] was accepted.

2.3.3. Thermooxidative behavior

Thermogravimetric analysis (TGA) was conducted in a Q500 device of TA Instruments (New Castle, DE, USA) at a heating rate of 20°C/min. Tests were run in oxygen atmosphere in the temperature range from room temperature (*RT*) to 700°C.

The oxygen induction temperature and time (OIT) were determined in a DSC-4 (PerkinElmer DSC 4). Two kinds of tests were made:

– Dynamic OIT (temperature ramp) method: the sample is heated in oxygen at a linear heating rate (10°C/min). The characteristic temperature of the beginning of the oxidation process is determined by the exothermic degradation-induced deviation from the baseline. Note that the scientific literature often prefers the term oxidation onset temperature (OOT) instead of dynamic OIT [18].
– Static OIT (isothermal) method: the sample is heated (from 60°C with 80°C/min) in an inert gas (nitrogen) atmosphere over the melting point to a selected test temperature ($T = 220$°C). This temperature was then kept constant. After reaching the selected temperature (2 min) it has been kept constant for 0.5 min prior to switching the nitrogen gas for oxygen. The oxidative reaction of exothermic feature normally occurs after a certain time period. The OIT value was determined as the time where a deviation from the base line takes place due to the strong exothermic degradation. Because the time was counted from the beginning of the DSC measurement, the OIT value was given by the actual elapsed time – 2.5 min. Recall that 2.5 min was required to reach the isothermal condition of the static OIT measurements.

2.3.4. Rheology

The melt rheology of the nanocomposites was analyzed by an MCR 501 dynamic oscillatory rheometer (Anton Paar Physics, Ostfildern, Germany) working under controlled strain conditions. The test geometry was parallel plate, the diameter of the plates was 25 mm. Compression molded disks of ca. 2 mm thickness were placed between the plates hold at $T = 175$°C. The thickness of the gap was set for 1.5 mm by squeezing the initial PE disk. Frequency sweep tests were carried out at $T = 175$°C. During the measurement a small amplitude (1%) oscillatory shear was applied to the samples. The storage and loss shear moduli ($G'$and G'', respectively) and the dynamic viscosity $|\eta^*|$ were measured as a function of angular frequency (ω) in the range 0.01–100 rad/s.

3. Results and discussion

3.1. BA dispersion

Figure 1 shows SEM pictures taken from the cryocut surfaces of LDPE and HDPE composites with 4 wt% BA40. One can recognize that BA is finely and rather uniformly dispersed in the related matrices.

BA remains in fine dispersion also when introduced in higher amount as demonstrated in Figure 2. The high magnification SEM picture in Figure 2b already indicates that the BA particles are agglomerated. Nevertheless, their mean particle size is on submicrometer scale and thus the related compounds can be termed as nanocomposites.

TEM pictures substantiate that the designation nanocomposite is correctly used (cf. Figure 3). The

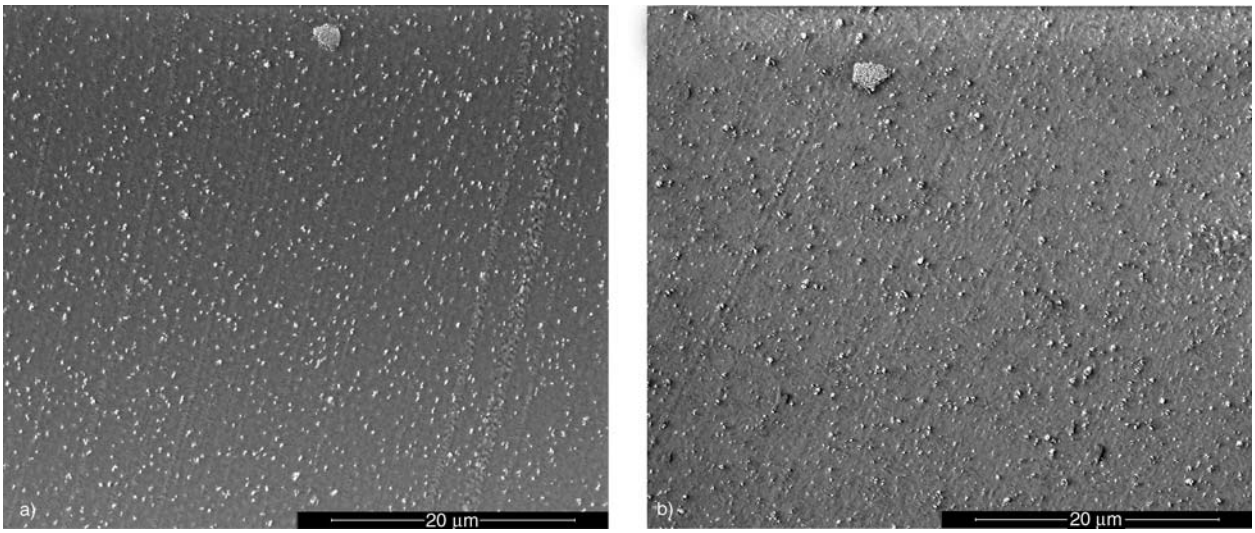

Figure 1. SEM micrographs taken from the cryocut surfaces of LDPE4%BA40 (a) and HDPE4%BA40 (b), respectively

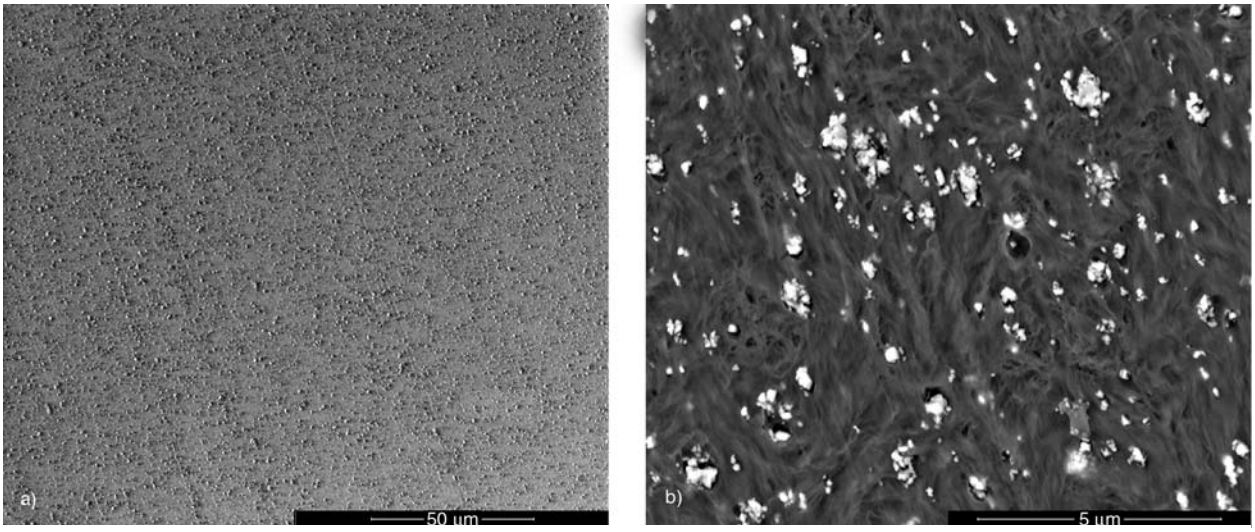

Figure 2. SEM micrographs at various magnifications taken from the cryocut surface of HDPE8%BA80

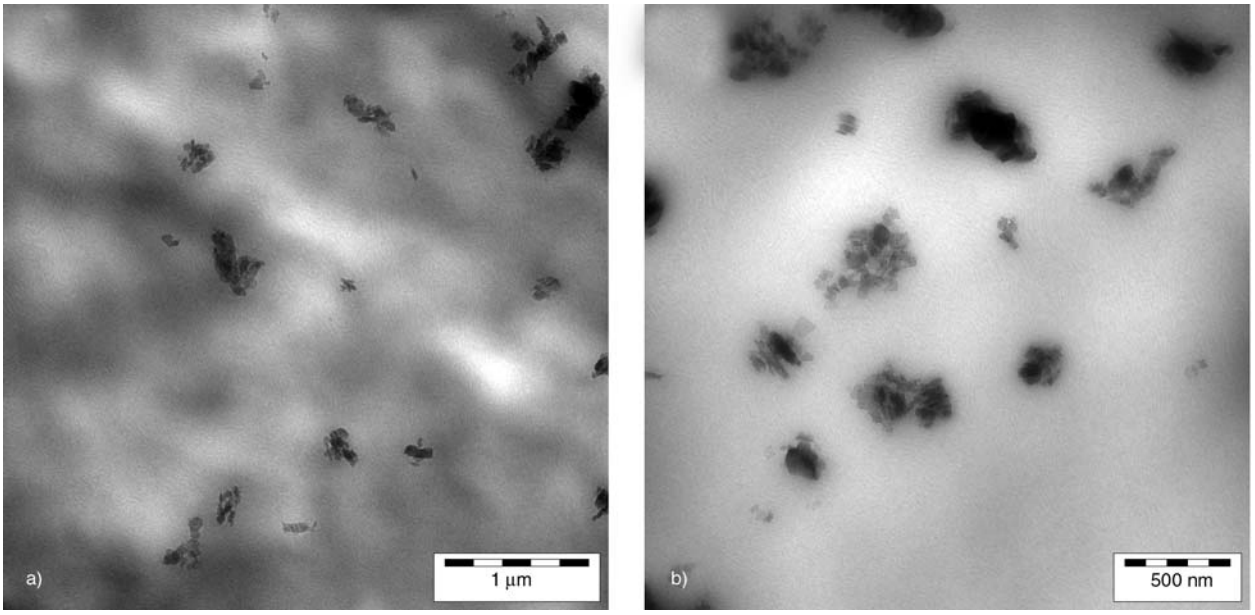

Figure 3. TEM micrographs at various magnifications taken of HDPE4%BA40

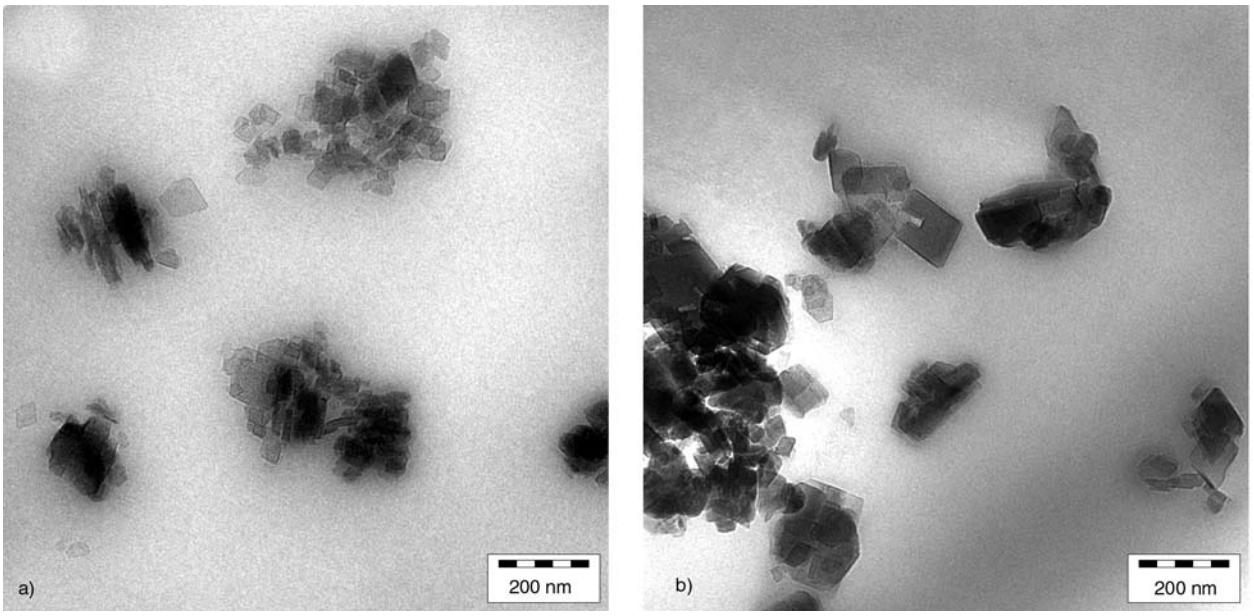

Figure 4. TEM micrographs taken of HDPE4%BA40 (a) and HDPE4%BA80 (b), respectively.
Note: the primary crystallite sizes of BA40 and BA80 are 40 and 74 nm, respectively (cf. Table 1).

difference in the primary crystallite sizes of the BA grades used is well perceptible by comparing the TEM pictures in Figure 4.

The above morphological results confirm that BA can finely be dispersed in PEs even without using coupling agent and polymeric compatibilizer.

3.2. Thermal properties (melting and crystallization)

DSC scans monitored during the 1st and 2nd heating, and cooling are shown for the LDPE/BA40 nanocomposites in Figure 5a and 5b, respectively. It is clearly seen that BA did not affect the melting behavior of the LDPE in the corresponding nanocomposites. A similar conclusion can be drawn by considering the DSC melting traces of the HDPE/BA nanocomposites – cf. Table 2.

However, the crystallization traces in Figure 5b indicate that BA worked as a weak nucleation agent for the crystallization of LDPE. This is obvious due to the shift of the crystallization peak towards higher temperature.

In order to quantify the effects of BA on the melting and crystallization of HDPE and LDPE the DSC traces were analyzed. The melting was characterized by two temperatures, namely peak maximum ($T_{m,\max}$) and final melting ($T_{m,final}$), and the crystallinity value (X_m). The latter was determined by considering the actual melting enthalpy in respect to the 100% crystalline PE (293 J/g as disclosed above [17]). Note that for the crystallinity calculation the BA content of the samples has been considered. The crystallization behavior was characterized again by two temperatures, namely peak maximum ($T_{c,\max}$) and initiation of the crystalliza-

Table 2. Melting and crystallization characteristics of the PE/BA nanocomposites from DSC measurements

Materials	1st melting			Crystallization			2nd melting		
	$T_{m,max}$ [°C]	$T_{m,final}$ [°C]	X_m [%]	$T_{c,max}$ [°C]	$T_{c,initial}$ [°C]	X_m [%]	$T_{m,max}$ [°C]	$T_{m,final}$ [°C]	X_m [%]
Neat HDPE	132.0	145.3	55.3	115.0	119.0	58.0	132.0	147.0	58.0
HDPE4%BA40	131.2	144.3	57.2	116.0	125.0	60.0	132.0	145.5	59.0
HDPE8%BA40	132.0	144.0	58.0	117.3	130.0	56.4	132.2	145.0	58.0
HDPE4%BA80	132.0	145.5	62.0	112.1	119.0	63.1	133.4	149.3	55.1
HDPE8%BA80	131.0	145.0	59.0	116.0	121.4	61.3	132.0	146.3	60.5
Neat LDPE	112.0	127.0	33.2	97.0	104.0	38.4	112.0	126.1	39.0
LDPE4%BA40	111.3	126.1	39.1	98.5	108.0	40.2	111.5	124.0	40.0
LDPE8%BA40	111.0	122.5	37.0	99.1	109.5	37.3	111.0	123.1	37.1
LDPE4%BA80	111.1	124.0	40.3	99.1	110.5	38.2	111.2	126.5	40.0
LDPE8%BA80	111.3	126.0	35.0	99.0	114.0	35.0	111.4	126.1	36.2

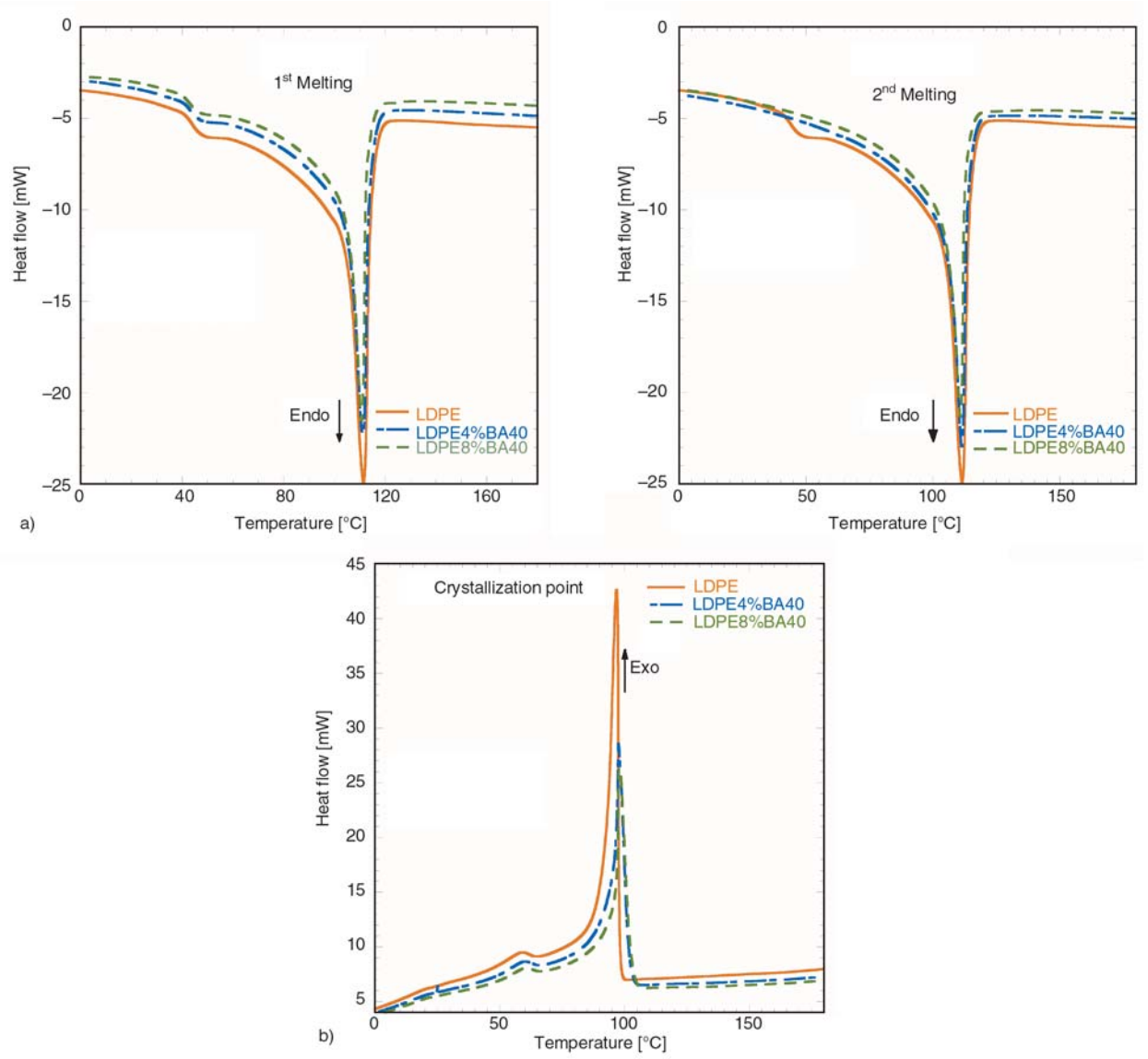

Figure 5. a) DSC heating scans on the LDPE nanocomposites containing 4 and 8 wt% BA40, respectively. Note: heating rate 20°C/min. b) DSC cooling scans on the LDPE nanocomposites containing 4 and 8 wt% BA40, respectively. Note: cooling rate 20°C/min.

tion ($T_{c,initial}$). The crystallinity achieved was also calculated (supposing 293 J/g for the 100% crystallinity). The data related to LDPE and HDPE nanocomposites are summarized in Table 2. It is noteworthy that the weak nucleation effect of BA turns more clearly when $T_{c,initial}$ instead of $T_{c,max}$ values are considered. However, to clarify the nucleation effect of BA on PEs DSC tests at lower cooling rates should be performed.

Data from the 1st heating scans may also suggest that BA increased the crystallinity of both the LDPE and HDPE samples. However results from 2nd heating do not support such effect. It is noteworthy that data from the 2nd heating are relevant as the samples have the same thermal history. BA acted as weak nucleation agent that is proved by the enhanced $T_{c,initial}$ and $T_{c,max}$ values for the PE/BA nanocomposites. It is interesting to note that BA80 was less efficient nucleating agent than BA40 in HDPE. On the other hand, the opposite tendency was observed for the LDPE/BA nanocomposites.

3.3. Thermooxidative properties (TGA, OIT)

3.3.1. TGA

The TGA curves registered for the LDPE and HDPE nanocomposites are displayed in Figures 6 and 7.

One can recognize that the BA acted in most nanocomposites as an additional thermooxidative

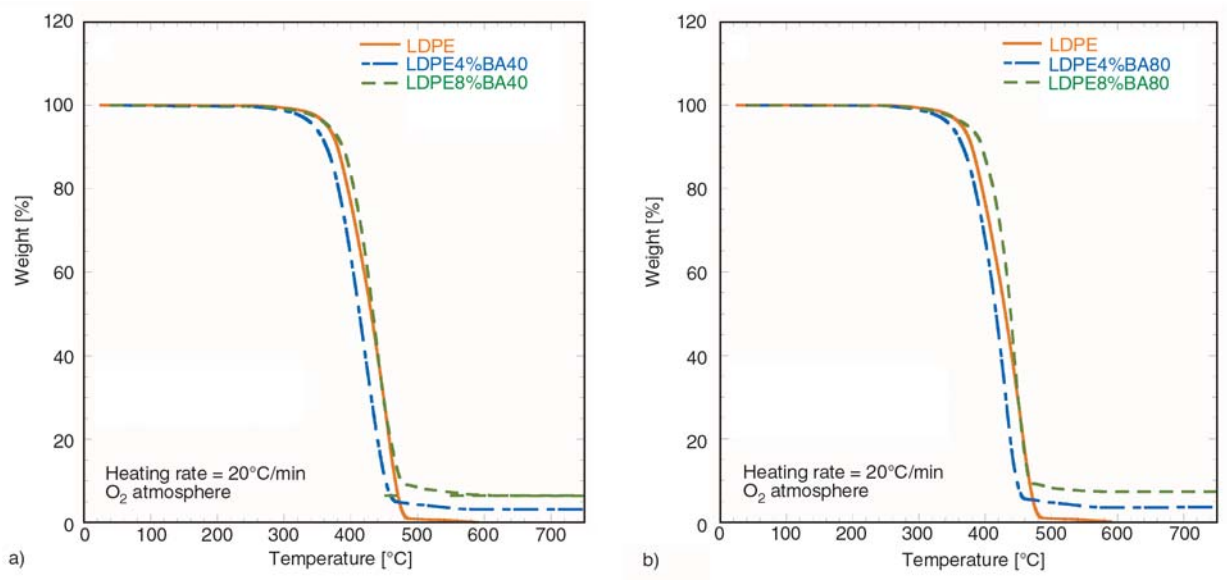

Figure 6. TGA traces of the LDPE nanocomposites with BA40 (a) and BA80 (b)

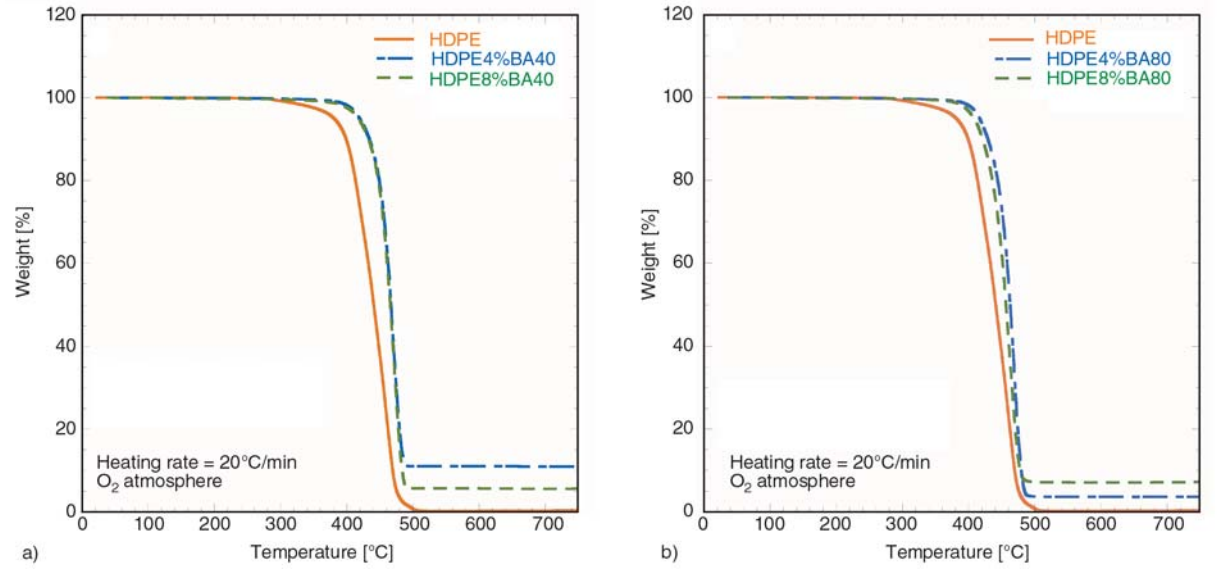

Figure 7. TGA traces of the HDPE nanocomposites with BA40 (a) and BA80 (b)

stabilizer. Its effect was quantified based on the TGA traces by those temperatures which were associated with a weight loss of 2 and 10%, respectively (cf. Table 3). The TGA data in Table 3 dis-

Table 3. TGA and OIT results for the PEs and PE/BA nanocomposites

Materials	TGA			OIT	
	–2 wt% loss [°C]	–10 wt% loss [°C]	Residue [%]	Dynamic [°C]	Static [min]
HDPE Ref	345	400	0.2	235.5	11.0
HDPE4%BA40	347	406	3.4	244.7	21.0
HDPE8%BA40	354	415	6.7	243.8	24.0
HDPE4%BA80	355	408	3.5	–	31.0
HDPE8%BA80	351	423	11.0	–	28.0
LDPE Ref	341	380	0.3	210.8	2.7
LDPE4%BA40	334	381	4.7	–	3.1
LDPE8%BA40	334	387	6.4	215.6	3.0
LDPE4%BA80	338	384	4.6	–	2.6
LDPE8%BA80	352	412	7.1	–	3.2

Notes: – sample not tested. Static OIT data derived from two parallel tests.

play that BA incorporation increased those temperatures where 2 and 10 wt% weight losses, respectively, occurred.

Improved thermooxidative stability owing to the presence of BA has been reported for polyoxymethylene [4]. Interestingly, BA incorporation also improved the stability to photochemical degradation in polyolefins [10, 19]. To clarify the mechanism of BA for improving the thermooxidative stability of PEs (and other polymers) is a very challenging and acute task.

3.3.2. OIT measurements

In order to gain a deeper insight in the thermooxidative action of BA, dynamic and static OIT measurements were performed. The determination of oxidation induction time (OIT_{time}) and oxidation induction temperature (OIT_{temp}) are widely used methods in the thermal analysis of polymers.

Dynamic OIT measurements were aimed at finding a suitable temperature at which the static (i.e. isothermal) OIT tests can be carried out. Figure 8 shows the primary results of the dynamic OIT measurements on the example of LDPE, HDPE, and HDPE8%BA40.

The DSC traces in Figure 8 indicate that the exothermal degradations of HDPE and LDPE start at about 240 and 215°C, respectively. As a consequence we have selected $T = 220$°C to perform the isothermal OIT measurements. It should be noted that $T = 220$°C may be a bit high for LDPE and related nanocomposites and thus differences between their OIT values may not be so pronounced.

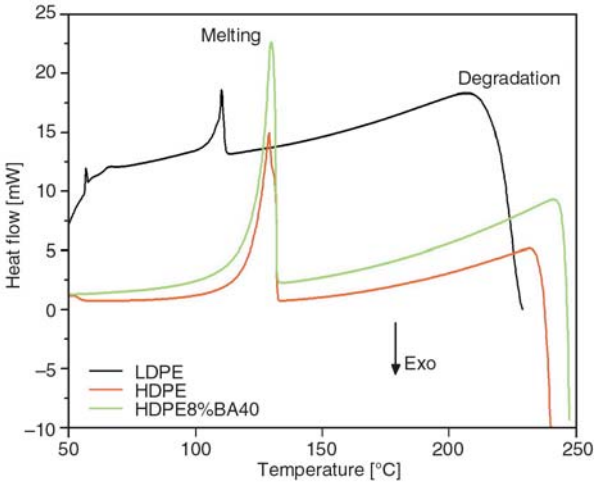

Figure 8. Dynamic OIT measurements on the examples of LDPE, HDPE, and HDPE8%BA40

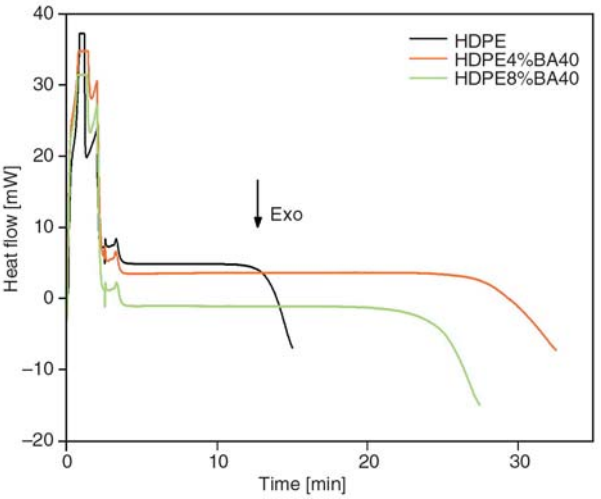

Figure 9. Static (isothermal) OIT curves monitored for HDPE and HDPE/BA40 nanocomposites

Figure 9 displays characteristics static OIT curves registered for HDPE and HDPE/BA nanocomposites.

Figure 9 and the corresponding data in Table 3 already show that the static OIT did not change linearly with the BA content. In addition, according to the TGA results the actual BA content in the sample did not always agree with the nominal BA content. The latter is most probably linked with the sample weight. Nevertheless, BA incorporating enhanced the static OIT. The relative improvement in OIT was more pronounced for HDPE than for LDPE. The improvement in the thermooxidative stability can be explained either by a change in the chemical pathway of the thermal decomposition, or by sorption (physical) effects caused by the nanofiller (e.g. [20]). It is intuitive, that the thermal stability of PE absorbed on the BA surface is higher than that of the bulk due to reduced molecular mobility. This should be valid also for systems with rather weak filler/matrix interaction as in our case. It should also be born in mind, that the volatilization of decomposed gaseous products may also be hampered by the nanofillers of large specific surface area. The feeling of the authors is that the improved thermooxidative stability of PE/BA nanocomposites is due to the abovementioned absorption phenomena. To clarify this effect analytical studies are now in progress. Preliminary results already confirm that the enhanced stability to thermooxidative degradation is related with molecular absorption, in fact.

3.4. Rheological behavior

The rheological tests resulted in unexpected results. Incorporation of nanofillers in thermoplastics (including polyolefins) is generally associated with a marked increase in the melt viscosity, at least in the range of low frequencies (e.g. [21–23]). Parallel to that a steep enhancement in the shear storage modulus (G') can be noticed. These changes are usually assigned to a pseudo solid-like transition caused by the dispersed nanoparticles. The interactions between the nanoparticles and polymer chains hamper the mobility of the latter, increase the friction between them, and thus increase both the viscosity and elasticity of the melt. Moreover, the difference in the melt viscosity and the G' value at low shear rates are often considered as indicators for the fine dispersion and strong particulate filler/matrix interactions (e.g. [23, 24]). However, this is clearly not the case when having a look at the graphs depicted in Figures 10 and 11. The rheological behavior of the systems, as shown in Figures 10 and 11, suggests that there is no strong interaction between the BA and PE in our nanocomposites. This is very beneficial for the processing of such nanocomposites as their melt viscosity practically does not change with either type or amount of BA. To figure out the possible mechanisms behind this finding require, on the other hand, further investigations.

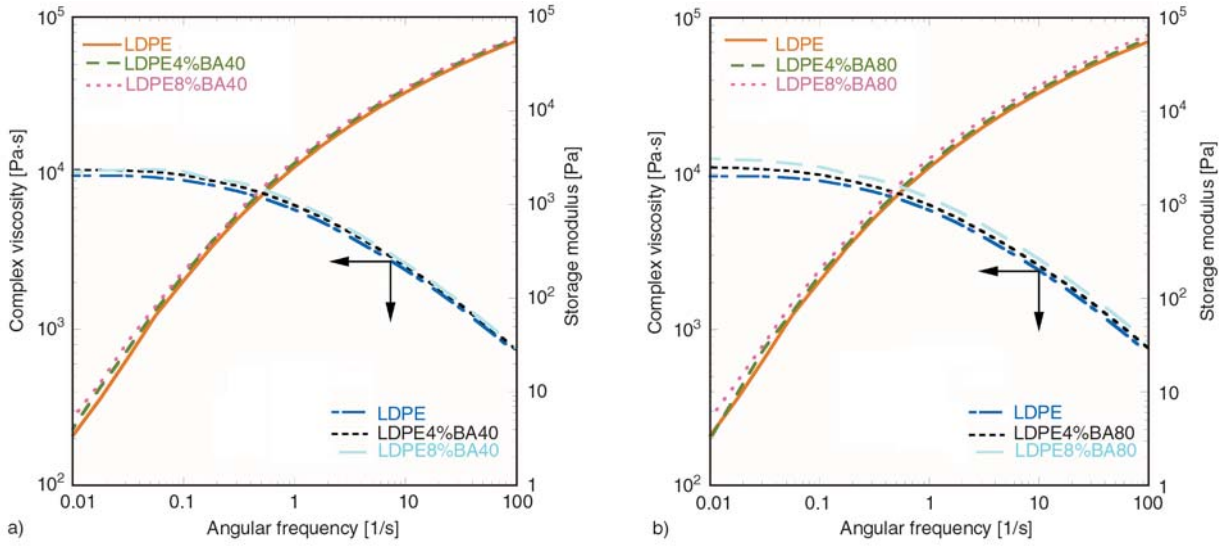

Figure 10. Complex viscosity $|\eta^*|$ and storage modulus (G') vs. angular frequency (ω) for LDPE (a) and LDPE/BA

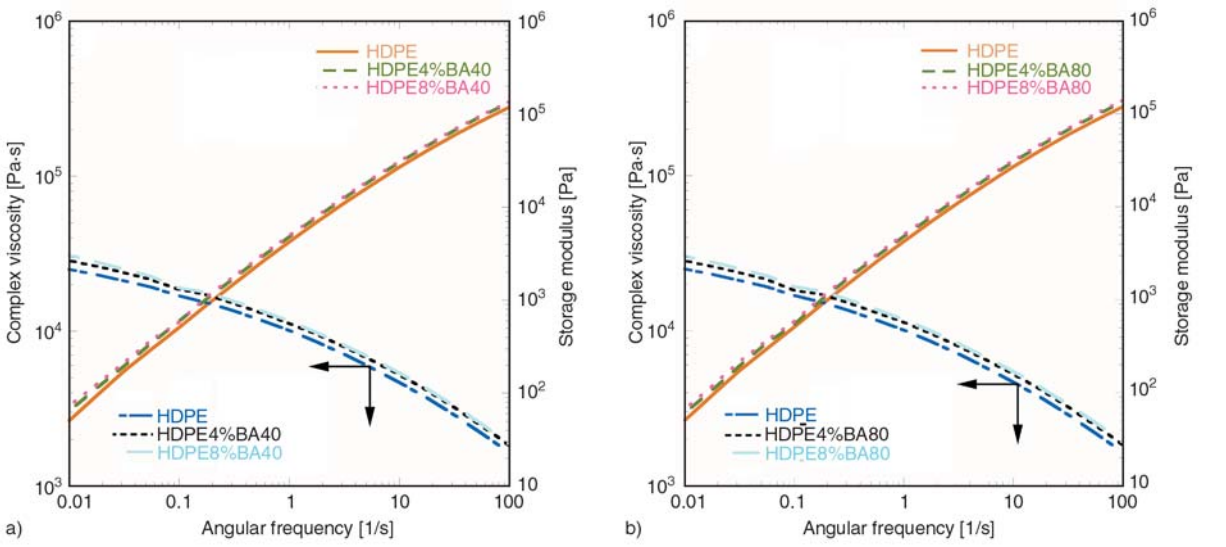

Figure 11. Complex viscosity $|\eta^*|$ and storage modulus (G') vs. angular frequency (ω) for HDPE (a) and HDPE/BA nanocomposites (b)

4. Conclusions

This work was devoted to determine the effects of synthetic boehmite alumina (BA) on the morphology, thermal, thermooxidative and rheological behavior of polyethylenes (PEs). BA was incorporated, up to 8 wt%, in both low- (LDPE) and high-density PE (HDPE) through melt compounding. It was established that BA was finely, and rather uniformly dispersed, though agglomerated, in the corresponding PEs. BA acted as a weak nucleating agent because it reduced slightly the undercooling (difference between the melting and crystallization temperatures) of both LDPE and HDPE. The nucleation capability of BA depended on the type, and in lesser extent also on the amount of the BA incorporated. Filling with BA strongly improved the stability to thermooxidative degradation of the corresponding PE matrix. The stabilizing effect of BA was more pronounced for HDPE than for LDPE. This finding is likely linked with the absorption of PE chains on the BA surface rather than with a synergistic effect of BA with the thermostabilizer initially present in the corresponding PE. Surprisingly, the melt rheology of the PE/BA nanocomposites was well matched with that of the parent PEs. This behavior is seldom for thermoplastic nanocomposites and has great practical relevance (i.e. similar processability as the plain PEs). Further investigations are needed, however, to reason this unexpected rheological performance.

Acknowledgements

The authors are indebted to Profs. S. Sinha Ray and O. C. Vorster (Nanocenter – Council for Scientific and Industrial Research , and Tshwane University of Technology, respectively, both in Pretoria, South Africa) for testing facilities and discussion of the results. The BA delivery, arranged by Dr. O. Torno (Sasol GmbH, Hamburg, Germany), is gratefully acknowledged.

References

[1] Karger-Kocsis J.: On the toughness of 'nanomodified' polymers and their traditional polymer composites. in 'Nano- and micro-mechanics of polymer blends and composites' (eds: Karger-Kocsis J., Fakirov S.) Hanser, Munich, 425–470 (2009).

[2] Streller R. C., Thomann R., Torno O., Mülhaupt R.: Isotactic poly(propylene) nanocomposites based upon boehmite nanofillers. Macromolecular Materials and Engineering, **293**, 218–227 (2008).
DOI: 10.1002/mame.200700354

[3] Streller R. C., Thomann R., Torno O., Mülhaupt R.: Morphology, crystallization behavior, and mechanical properties of isotactic poly(propylene) nanocomposites based on organophilic boehmites. Macromolecular Materials and Engineering, **294**, 380–388 (2009).
DOI: 10.1002/mame.200800360

[4] Siengchin S., Karger-Kocsis J., Thomann R.: Nanofilled and/or toughened POM composites produced by water-mediated melt compounding: Structure and mechanical properties. Express Polymer Letters, **2**, 746–756 (2008).
DOI: 10.3144/expresspolymlett.2008.88

[5] Siengchin S., Karger-Kocsis J.: Structure and creep response of toughened and nanoreinforced polyamides produced via the latex route: Effect of nanofiller type. Composites Science and Technology, **69**, 677–683 (2009).
DOI: 10.1016/j.compscitech.2009.01.003

[6] Siengchin S., Karger-Kocsis J.: Mechanical and stress relaxation behavior of Santoprene® thermoplastic elastomer/boehmite alumina nanocomposites produced by water-mediated and direct melt compounding. Composites Part A: Applied Science and Manufacturing, in press (2010).
DOI: 10.1016/j.compositesa.2010.02.009

[7] Siengchin S., Karger-Kocsis J., Thomann R.: Alumina-filled polystyrene micro- and nanocomposites prepared by melt mixing with and without latex precompounding: Structure and properties. Journal of Applied Polymer Science, **105**, 2963–2972 (2007).
DOI: 10.1002/app.26505

[8] Brostow W., Datashvili T., Huang B., Too J.: Tensile properties of LDPE+boehmite composites. Polymer Composites, **30**, 760–767 (2009).
DOI: 10.1002/pc.20610

[9] Brostow W., Datashvili T., Kao D., Too J.: Tribological properties of LDPE+boehmite composites. Polymer Composites, **31**, 417–425 (2010).
DOI: 10.1002/pc.20820

[10] Bocchini S., Morlat-Thérias S., Gardette J-L., Camino G.: Influence of nanodispersed boehmite on polypropylene photooxidation. Polymer Degradation and Stability, **92**, 1847–1856 (2007).
DOI: 10.1016/j.polymdegradstab.2007.07.002

[11] Özdilek C., Kazimierczak K., van der Beek D., Picken S. J.: Preparation and properties of polyamide-6-boehmite nanocomposites. Polymer, **45**, 5207–5214 (2004).
DOI: 10.1016/j.polymer.2004.05.029

[12] Özdilek C., Mendes E., Picken S. J.: Nematic phase formation of boehmite in polyamide-6 nanocomposites. Polymer, **47**, 2189–2197 (2006).
DOI: 10.1016/j.polymer.2006.01.043

[13] Özdilek C., Norder B., Picken S. J.: A study of the thermo-mechanical behavior of boehmite-polyamide-6 nanocomposites. Thermochimica Acta, **472**, 31–37 (2008).
DOI: 10.1016/j.tca.2008.03.008

[14] Xalter R., Pelascini F., Mülhaupt R.: Ethylene polymerization, on-line particle growth monitoring, and *in situ* nanocomposite formation using catalysts supported on arylsulfonic acid-modified boehmites. Macromolecules, **41**, 3136–3143 (2008).
DOI: 10.1021/ma702623e

[15] Halbach T. S., Thomann Y., Mülhaupt R.: Boehmite nanorod-reinforced-polyethylenes and ethylene/1-octene thermoplastic elastomer nanocomposites prepared by *in situ* olefin polymerization and melt compounding. Journal of Polymer Science Part A: Polymer Chemistry, **46**, 2755–2765 (2008).
DOI: 10.1002/pola.22608

[16] Halbach T. S., Mülhaupt R.: Boehmite-based polyethylene nanocomposites prepared by in-situ polymerization. Polymer, **49**, 867–876 (2008).
DOI: 10.1016/j.polymer.2007.12.007

[17] Wunderlich B., Dole M.: Specific heat of synthetic high polymers. VIII Low pressure polyethylene. Journal of Polymer Science, **24**, 201–212 (1957).
DOI: 10.1002/pol.1957.1202410604

[18] Focke W. W., van der Westhuizen I.: Oxidation induction time and oxidation onset temperature of polyethylene in air. Journal of Thermal Analysis and Calorimetry, **99**, 285–293 (2010).
DOI: 10.1007/s10973-009-0097-1

[19] Chmela S., Fiedlerová A., Borsig E., Erler J., Mülhaupt R.: Photo-oxidation and stabilization of sPP and iPP/boehmite-disperal nanocomposites. Journal of Macromolecular Science Part A: Pure and Applied Chemistry, **44**, 1027–1034 (2007).
DOI: 10.1080/10601320701424461

[20] Zou D. Q., Yoshida H.: Size effect of silica nanoparticles on thermal decomposition of PMMA. Journal of Thermal Analysis and Calorimetry, **99**, 21–26 (2010).
DOI: 10.1007/s10973-009-0531-4

[21] Durmus A., Kasgoz A., Macosko C. W.: Linear low density polyethylene (LLDPE)/clay nanocomposites. Part I: Structural characterization and quantifying clay dispersion by melt rheology. Polymer, **48**, 4492–4502 (2007).
DOI: 10.1016/j.polymer.2007.05.074

[22] Rezanavaz R., Razavi Aghjeh M. K., Babaluo A. A.: Rheology, morphology, and thermal behavior of HDPE/clay nanocomposites. Polymer Composites, in press (2010).
DOI: 10.1002/pc.20889

[23] Dorigato A., Pegoretti A., Penati A.: Linear low-density polyethylene/silica micro- and nanocomposites: Dynamic rheological measurements and modeling. Express Polymer Letters, **4**, 115–129 (2010).
DOI: 10.3144/expresspolymlett.2010.16

[24] Chow W. S., Mohd Ishak Z. A., Karger-Kocsis J.: Morphological and rheological properties of polyamide 6/poly(propylene)/organoclay nanocomposites. Macromolecular Materials and Engineering, **290**, 122–127 (2005).
DOI: 10.1002/mame.200400269

eXPRESS Polymer Letters Vol.4, No.5 (2010) 275–283
Available online at www.expresspolymlett.com
DOI: 10.3144/expresspolymlett.2010.35

Preparation of cationic polyacrylamide by aqueous two-phase polymerization

*J. Xu, W. P. Zhao, C. X. Wang, Y. M. Wu**

College of Chemical Engineering, Qingdao University of Science and Technology, Qingdao 266042, P. R. China

Received 7 January 2010; accepted in revised form 4 March 2010

Abstract. Cationic polyacrylamide (CPAM) was synthesized by aqueous two-phase polymerization technique using acrylamide (AM) and dimethylaminoethyl methacrylate methyl chloride (DMC) as raw materials, aqueous polyethylene glycol 20000 (PEG 20000) solution as dispersant, 2,2′-azobis(2-amidinopropane) dihydrochloride (V-50) as initiator and poly(dimethylaminoethyl methacrylate methyl chloride) (PDMC) as stabilizer. The polymer was characterized by infrared (IR) spectroscopy, ^{1}H-NMR spectrum and transmission electron microscopy (TEM). The copolymer composition was analyzed. The effect of monomers concentration, PEG 20000 concentration and stabilizer concentration on copolymer were investigated, respectively. The optimum reaction conditions for obtaining a stable CPAM aqueous two-phase system were monomers concentration 8~15%, PEG 20000 concentration 15~25%, and PDMC concentration 0.5~1.5%. Finally, the formation process of copolymer particles was investigated by optical microscope.

Keywords: *polymer synthesis, aqueous two-phase polymerization, cationic polyacrylamide, dimethylaminoethyl methacrylate methyl chloride, polyethylene glycol 20000*

1. Introduction

Cationic polyacrylamides (CPAM) are a kind of important cationic polyelectrolyte and extensively used as flocculants for liquid/solid separation, retention and drainage aids in papermaking, flotation aids and demulsifiers for oil/water clarification, as soil improvers and drainage aids, etc. [1–3]. Various types of methods for producing CPAM have been developed, such as homogeneous aqueous solution polymerization, inverse emulsion polymerization, inverse suspension polymerization and dispersion polymerization, and so on [4, 5].

For homogeneous aqueous solution polymerization, the reaction heat was difficult to remove because the material became gel which can not flow. For the sake of transportation and dissolution easily, CPAM gel was used to be handled as dry powder instead of aqueous solution. However, these polymers in dry-powder form not only required consumption of energy in drying process at elevated temperature but also were subjected to degradation through shear or three-dimensional polymer crosslinking. For the inverse emulsion polymerization and inverse suspension polymerization, some surfactants and organic solvents were used in the course of syntheses, definitely resulting in the problems of environmental pollution and recycling [4–6]. Recently, aqueous dispersion polymerization was used to prepare cationic polymerization, which could be carried out in aqueous tert-butyl alcohol media [7–9] or in the aqueous inorganic salt media [6, 10, 11]. Especially, the dispersion polymerization in aqueous solution of ammonium sulfate attracted considerable attention because of its organic-free solvent. However, the use of an amount of inorganic salt would restrict its development and the extensive applications. For example, if the cationic polymerization was used as retention aid in paper-

*Corresponding author, e-mail: wuyumin001@126.com

making industry, excessive ammonium sulfate likely made paper become brittle.

The concept of aqueous two-phase system was presented in the 1950s, and the technique of aqueous two-phase separation was mature in the field of biotechnology for the separation and purification of valuable biomolecules [12–15]. Aqueous two-phase polymerization may be defined as a type of aqueous dispersion polymerization. In aqueous two-phase polymerization, the inorganic salt used in the aqueous dispersion polymerization was replaced by a water-soluble polymer. Polymerization reaction started from a homogeneous mixture of the water-soluble monomers, initiator, another water-soluble polymer and a stabilizer. The solvent was selected on the basis of solubility of monomers and stabilizer and insolubility of the polymer [16]. Polymerization was initiated in the aqueous solution by an initiator that was soluble in both the solvent and monomer. It may be used to prepare the water-soluble (co)polymers dispersion with good stability and high molecular weight which could be directly diluted to use. Aqueous two-phase polymerization overcame the problems of heat release of aqueous solution polymerization and avoided the environmental pollution and recycling questions of organic solvents in inverse suspension polymerization, water-in-oil inverse emulsion polymerization and precipitation polymerization [4–6]. Aqueous two-phase polymerization was an attractive alternative to other polymerization processes. However, to our knowledge, there were a few works on the preparation of water-soluble polymers by aqueous two-phase polymerization technique. Only Shan *et al.* successfully prepared the nonionic polyacrylamide by aqueous two-phase polymerization in the presence of PEG by using ammonium persulfate as the initiator and sodium dodecylsulfate or polyoxyethylene(20) sorbitan monolaurate as the emulsifier [17]. The stability of dispersion system with surfactants was weak and its viscosity was large. Until now, there are few works on synthesis of cationic polyacrylamide via aqueous two-phase polymerization without emulsifier.

Based on the theory above mentioned, the aqueous two-phase copolymerization of acylamide (AM) and dimethylaminoethyl methacrylate methyl chloride(DMC) was carried out in aqueous polyethylene glycol 20000 (PEG 20000) solution with 2,2′-azobis(2-amidinopropane) dihydrochloride (V-50) as initiator. And the poly(dimethylaminoethyl methacrylate methyl chloride) (PDMC), which acted as polymeric stabilizer, was first applied to lower dispersion viscosity and improve the stability of the synthetic system. Comparing to the system without PDMC as the polymeric stabilizer, some different results were obtained.

2. Experimentals

2.1. Materials

Acrylamide (AM, A. R. Grade) was purchased from Dia-Nitrix Co. Ltd. (Japan) and was used as received. Dimethylaminoethyl methacrylate methyl chloride (DMC, 78% aqueous solution, industrial grade) was from Mitsubishi Gas Chemical Company, INC and used without further purification. Polyethylene glycol 20000 (PEG) and 2,2′-azobis(2-amidino-propane) dihydrochloride (V-50; WAKO Pure Chemical Industries Ltd) were of analytical grade, and used as received. Poly(dimethylaminoethyl methacrylate methyl chloride) (PDMC), as 20% aqueous solution, was prepared from DMC in an aqueous solution using V-50 as initiator at 60°C. The molecular weight of PDMC was $3.9 \cdot 10^5$ g·mol^{-1}. Deionized water was used throughout this work. Other reagents were A. R. grade and used directly.

2.2. Preparation of CPAM by aqueous two-phase copolymerization

Varying quantities of ingredients containing monomers (AM and DMC), PEG, PDMC and deionized water were added to a 250 ml glass reactor fitted with a stirrer, a reflux condenser, a thermometer and a nitrogen inlet tube. After bubbling purified nitrogen through the solution for 30 minutes and controlling system temperature at 65°C by a water bath, the monomers were initiated by addition of V-50 solution into the reaction system under invariable stirring. The reactions were proceeded for 8~10 h to get a high overall conversion of monomers.

2.3. Characterization

The generated sample was precipitated repeatedly in a large quantity of acetone to remove the unreacted monomers and the PEG 20000. Then, the pre-

cipitated CPAM copolymer was dried to a constant weight at 45°C under vacuum. The dried sample was used to determine the intrinsic viscosity in 1.0 mol·l^{-1} NaCl at 30°C using an Ubbelohde viscometer [18]. The following Equation (1) was used to calculate the molecular weight of copolymer [10]:

$$[\eta] = 3.73 \cdot 10^{-4} [M_w]^{0.66} \quad (1)$$

The viscosity of the aqueous two-phase system was measured by Brookfiled DV-II+Viscometer at the room temperature. The average particle size and particle size distribution (PDI) was measured by a laser particle size analyzer (Zeta-Sizer 3000, Malvern, UK) after ultrasonic dispersion for 20 minutes in acetone. The particle morphology was observed by optical microscope and transmission electron microscopy (JEM-1200EX; JEOL, Japan). FT-IR spectra were recorded on a spectrophotometer (AVATAR 360, Nicolet, USA) using KBr pellets. The ^{1}H-NMR spectrum of AM/DMC copolymer was obtained in D_2O with a Bruker (500 MHz) ^{1}H-NMR spectrometer (Bruker Corporation, Bremen, Germany).

The overall monomer conversion could be obtained by determining the residual contents of AM and DMC with bromating method [6]. About 4.0 g of copolymer dispersion was weighed out in a weighing bottle, and then 100 ml of deionized water was added. After stirring adequately, the sample solution could be obtained. Excessive $KBrO_3$-KBr was added into the sample solution. In the presence of H^+, $KBrO_3$ reacted with KBr to produce Br_2, and then Br_2 could react with residual AM and DMC in the sample solution for addition reaction. Excessive KI was used to react with the residual Br_2, and I_2 was formed from the reaction mixture. By titrating I_2 with the standard solution of $Na_2S_2O_3$ and calculating the consumption of $Na_2S_2O_3$, the total residual contents of AM and DMC could be determined by means of the interrelationship of these ingredients.

3. Results and discussion

The concentrations of initiator and stabilizer were weight percent based on total monomers, and the content of monomers and dispersant were weight percent based on total raw reaction materials. The amount of each ingredient was kept constant in all experiments, except as indicated. X_{DMC} indicated the mole percentage of DMC based on the initial monomers composition.

3.1. Effect of monomers concentration

Figure 1 shows the monomers conversion versus time curves with different monomers concentrations. It was shown that the initial polymerization rate and the overall conversion increased with the increase of monomers concentration. As shown in Figure 1, when the monomers concentration was 8%, the overall monomers conversion was only 12% corresponding to the time at 30. However, when the monomers concentration was 20%, the overall conversion was 70% corresponding to the time at 30. This indicated that the lower the monomers concentration was, the stronger the shielding effect of aqueous PEG 20000 solution on monomers radicals was. So, the initiation efficiency of initiator decreased which resulted in decreasing of both the polymerization rate and the overall conversion. When the monomer concentration was higher than 20%, the dispersion was so unstable that coagulation occurred. As the monomers concentration increased, the initial polymerization rate increased and much more oligomers were formed in the aqueous PEG solution. Yet the phase separation effect of PEG and stabilization of PDMC were weakened. So, the stability of copolymer particles in the medium decreased and copolymer particles coagulated gradually.

The effects of the monomers concentration on the relative molecular weight, the average particle size

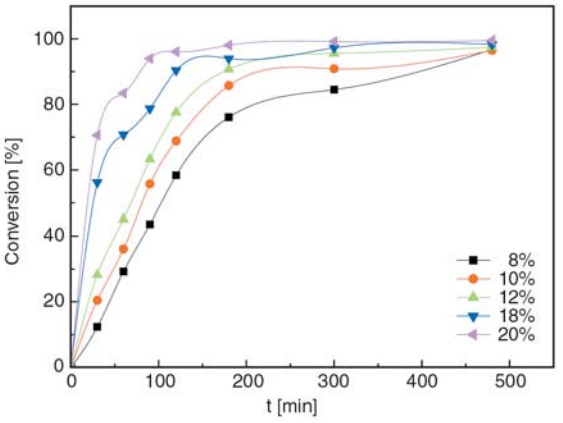

Figure 1. Conversion versus time curves with different monomers concentration. Polymerization conditions: X_{DMC} 10%, PEG 25%, V-50 0.009%, PDMC 1% and T 65°C.

Table 1. Effect of monomers concentration on aqueous two-phase system

Monomers [%]	M_w [10^{-6}·g·mol^{-1}]	P.D.[a] [nm]	η [mPa·s]	Characteristics
8	1.15	716.8	4567	Gray-white, good fluidity, and low viscosity dispersion
10	1.32	759.7	5065	Gray-white, good fluidity, and low viscosity dispersion
12	1.45	839.6	5723	Milky-white, good fluidity, and low viscosity dispersion
15	1.69	956.7	5998	Milky-white, good fluidity, and low viscosity dispersion
20	1.89	1168.5	7596	Milky-white, good fluidity, and high viscosity dispersion

[a]P.D. average of particle diameter;
Polymerization conditions: X_{DMC} 10%, PEG 25%, V-50 0.009%, PDMC 1% and T 65°C

and the apparent viscosity of dispersion were shown in Table 1. It was seen that the relative molecular weight, the average particle size and the apparent viscosity of dispersion all increased with the increase of monomers concentration, which conformed to the rules of typical free radical polymerization [19]. When the monomers concentration was up to 20%, the viscosity of dispersion drastically increased on such condition, the dispersion was so unstable that coagulation occurred.

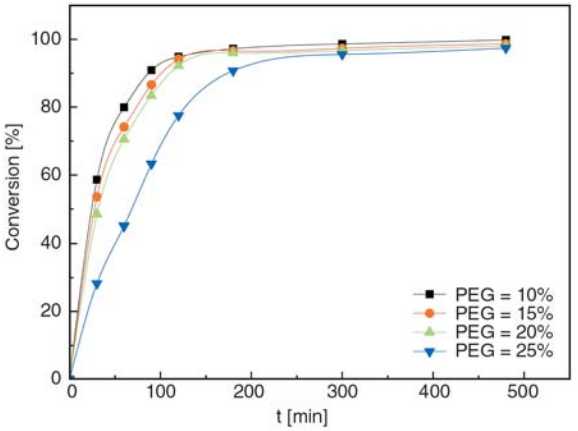

Figure 2. Conversion versus time curves with different PEG 20000 content. Polymerization conditions: total monomer 8%, X_{DMC} 10%, PEG 25%, V-50 0.009%, PDMC 1% and T 65°C.

3.2. Effect of PEG 20000 content

High molecular weight PEG 20000, which had a tendency to interact with water through hydrogen bonding, was chosen as the phase separation agent because it formed aqueous two-phase system at lower concentrations and hence of lower viscosities [12]. To investigate the effect of the PEG 20000 content on the aqueous two-phase copolymerization system, five different PEG 20000 content (i.e. 5, 10, 15, 20, and 25%) were examined. Figure 2 shows the relationship between the conversion and time in five different PEG 20000 concentrations. It was clear that high PEG 20000 content retarded the initial copolymerization rate and decreased the overall monomers conversion, which was contrary to the work that Shan and Cao reported [17]. It was due to that the following: as the PEG 20000 content increased, the viscosity of the continuous phase increased correspondingly, which prevented monomer radicals to be freely transferred between mature particles and continuous phase. So the growth of copolymer particles became slower. At the same time, the shielding effect to free radicals was improved by PEG 20000. Thus, the initial copolymerization rate and the final overall conversion were both reduced.

As shown in Table 2, the molecular weight of copolymers and the apparent viscosity of the system lowered with increasing the PEG content. The average particle size and PDI also decreased. The reason was that increasing the PEG content resulted in the critical chain length to phase-out shorter. Therefore, the viscosity of the continuous phase decreased and the particle size as well as particle size distribution became smaller [11]. Meanwhile, the PEG 20000 had active α-hydrogen atoms and

Table 2. Effect of PEG 20000 concentration on aqueous two-phase polymerization

w_{PEG} [%]	M_w [10^{-6}·g·mol^{-1}]	η [mPa·s]	P.D. [nm]	PDI	Characteristics
5	1.04	10450	969.6	0.519	High viscosity, large particles, and phase separation
10	0.99	6486	836.3	0.497	High viscosity, large particles, and phase separation
15	0.92	6070	814.9	0.480	Milky-white, good fluidity, and low viscosity dispersion
20	0.91	4946	801.5	0.430	Milky-white, good fluidity, and low viscosity dispersion
25	0.84	4736	716.8	0.369	Milky-white, good fluidity, and low viscosity dispersion

Polymerization conditions: total monomer 8%, X_{DMC} 10%, V-50 0.009%, PDMC 1% and T 65°C

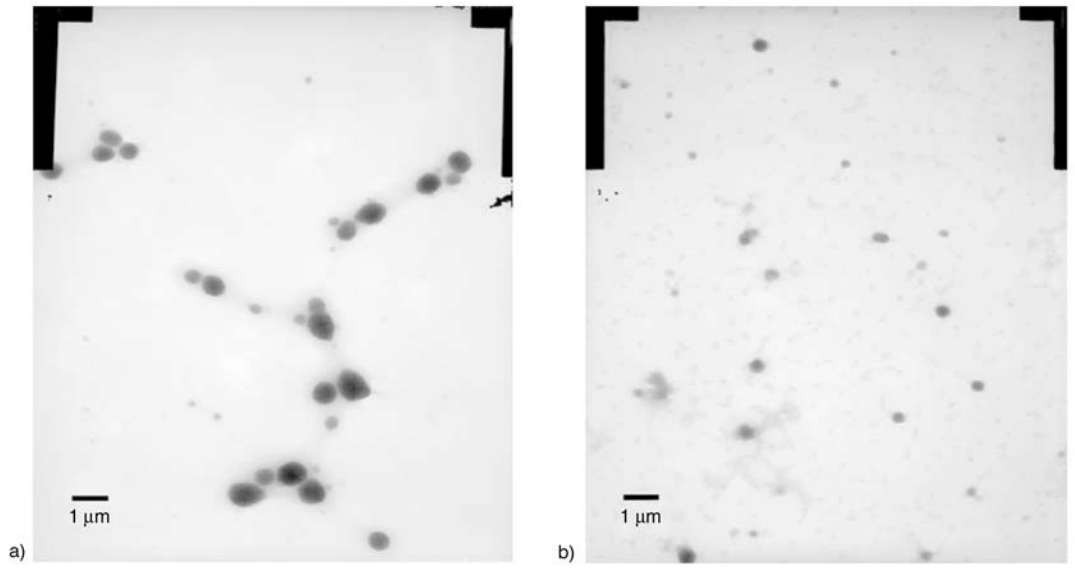

Figure 3. TEM photos of CPAM particles prepared in aqueous two-phase polymerization system with different PEG 20000 content: (a) 15%, (b) 25%

acted as chain transfer agent. Thus, the relative molecular weight decreased with PEG 20000 increasing. In addition, it was observed that the unstable dispersions were obtained when the PEG 20000 concentration was less than 10%. Under such conditions, the polymerization of most monomers occurred in the continuous phase because the ability of phase separation decreased.

Figure 3 shows the TEM photos of CPAM particles in aqueous two-phase polymerization system with different PEG 20000 contents. It revealed that the coalescence between polymer particles took place and the particle size was larger when the PEG 20000 content was 15%, to a certain extent. But, when the PEG content was 25%, no coalescence was observed and the particle size of polymer particles was smaller.

3.3. Effect of stabilizer concentration

In the system, a water-soluble homopolymer PDMC was used as a steric stabilizer. Figure 4 shows that there was a little effect of PDMC concentration on the initial polymerization rate and the overall conversion. The reason was that at the earlier stage of polymerization, monomers polymerization mainly took place in the dispersion media, adding a small amount of PDMC into the continuous phase had a little effect on the initiator.

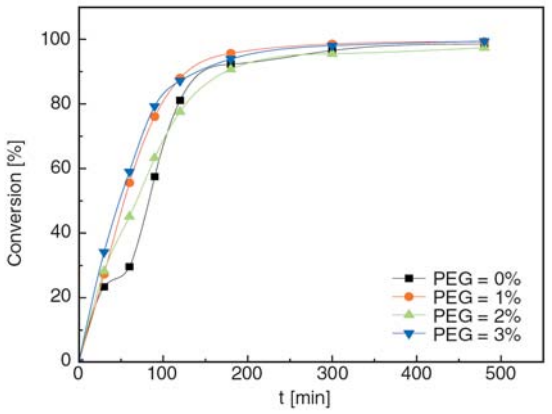

Figure 4. Conversion versus polymerization time curves with different PDMC concentrations. Polymerization conditions: Total monomers 8%, X_{DMC} 12%, V-50 0.009%, PEG 25% and T 65°C.

From the results of Table 3, it was revealed that the relative molecular weight increased with PDMC concentration, which was consistent with some works reported [1, 2]. With the increase of the sta-

Table 3. Effect of stabilizer PDMC concentration on CPAM aqueous two-phase system

PDMC [%]	M_w 10^{-6} [10^{-6}·g·mol^{-1}]	η [mPa·s]	P.D. [nm]	Characteristics
0.0	0.65	3280	773.1	Phase separation after 3 months
0.5	0.76	3217	763.2	Milky-white, smooth, still stable after 6 months
1.0	0.82	5065	758.5	Milky-white, smooth, still stable after 6 months
1.5	0.94	5156	843.6	Milky-white, smooth, still stable after 6 months
2.0	0.95	7615	931.5	Phase separation after 7 days

bilizer concentration, a greater number of smaller particles were stabilized for the high stability. The smaller particle can effectively capture growing oligomeric radicals initiated in continuous phase. Solid-phase polymerization occurred to yield the polymer of high molecular weight due to the gel effect. Meanwhile, both the apparent viscosity of dispersion and the average particle size decreased first and then increased, which was contrary to other works related to aqueous dispersion polymerization [1, 8]. The difference may be due to the absence of inorganic salt. Increasing the stabilizer concentration, the average particle size decreased. When PDMC concentration was 1%, the particles with the smallest particle size were obtained. However, beyond this point, the average particle size increased with PDMC concentration. Firstly, when PDMC concentration was below 1%, PDMC was mainly acted as stabilizer and protect particles from coalescence. As the PDMC concentration increased from 0 to 0.5%, both the average particle size and the viscosity of dispersion decreased. However, when the PDMC concentration was too high (1.0% and above), the viscosity of system and the average particle size increased, but the stability of dispersion became weak. This was probably due to that extra stabilizer molecules did not participate in stabilization, but they had bridging role between the particles, inducing agglomeration. So the apparent viscosity and the particle size both increased again.

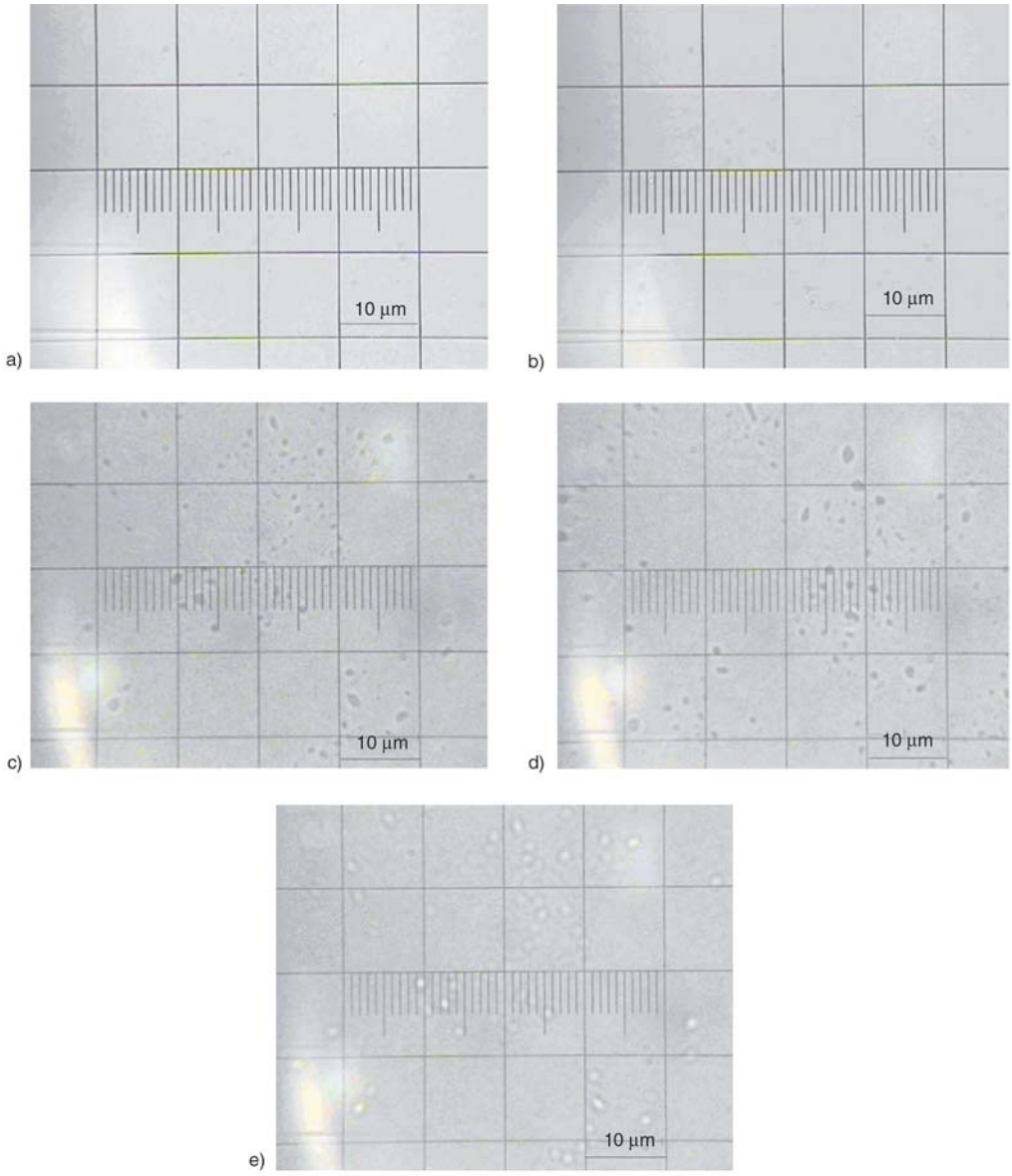

Figure 5. Microstructure of dispersed droplets in the aqueous two-phase polymerization system

3.4. Formation of dispersed droplets in aqueous two-phase polymerization

Figure 5 showed the microstructure of the dispersed droplets in the aqueous two-phase polymerization system. The system was homogeneous before the polymerization (Figure 5a). As soon as the polymerization started, the primary free radicals grew in the dispersion media by addition of initiator until they reached their critical chain length. Then, they precipitated from the dispersion media to form nuclei. These nuclei with higher surface energy were unstable and quickly aggregated each other to form mature particles (Figure 5b). As the polymerization proceeded, the number of the mature particles in media became larger. At the same time, the mature particles grew by capturing the monomers, oligomeric radicals and nuclei in the dispersion media (Figure 5c). Because the particles consumed an amount of oligomeric radicals and nuclei, the rate of formation of particle reduced. Particles continually captured monomers from the dispersion media to form larger particles (Figure 5d). Until the monomers were nearly used up, the volume of particles did not change any longer (Figure 5e).

3.5. Characteristics of CPAM aqueous two-phase

Figure 6 shows the FTIR spectra for the final copolymer. The peaks at 3300~3500 cm^{-1} were due to amine group, whereas the peak at 1659 and 952 cm^{-1} was due to amide group and quaternary

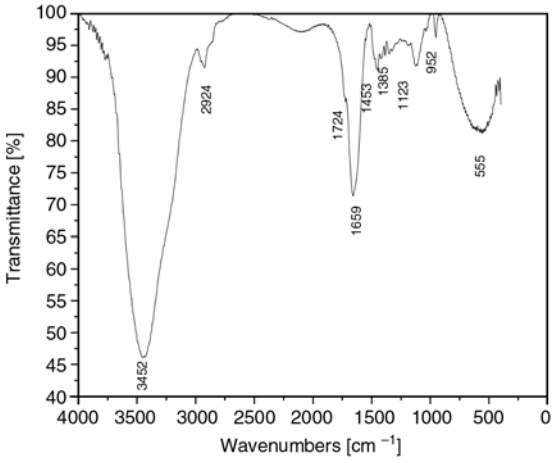

Figure 6. IR spectra of P(AM/DMC)

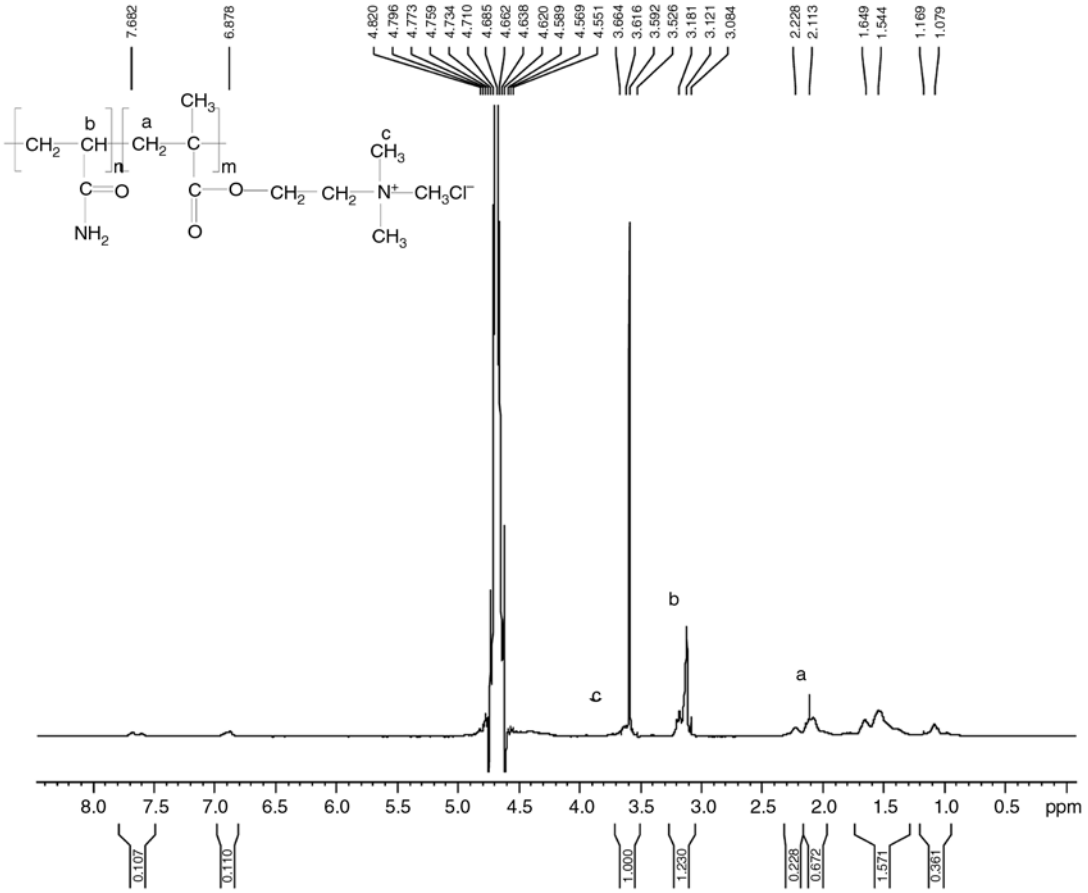

Figure 7. ^{1}H-NMR spectra of AM with DMC copolymer (X_{DMC} = 10%)

ammonium. The peaks at 2924, 1724 and 1453 cm^{-1} were assigned to υ–CH_3, υ–O–CO– and δ–CH_2–$N^+(CH_3)_3$, respectively. It was believed that the final formed copolymer was P(AM/DMC). Figure 7 represents ^{1}H-NMR spectra of the P(AM/DMC). Each proton was readily distinguished from the resonance peaks of the copolymer. According to the integral area of the resonance peaks of b and c proton (–CH of AM and –CH_3 of DMC), the approximate composition of the copolymer could be calculated. The molar ratio of AM to DMC in the copolymer is about 88/12, which was near to the ratio in the feed, 90/10. The copolymer composition determined via ^{1}H-NMR spectroscopy was in good agreement with the molar feed compositions and typically deviated no more than 2 mol% from the feed values.

4. Conclusions

In this work, cationic polyacrylamide (CPAM) was synthesized by aqueous two-phase polymerization technology. The initial polymerization rate, the overall conversion of monomers, the relative molecular weight, the average particle size, and the apparent viscosity of dispersion all increased with monomers concentration, contrary to PEG 20000 concentration. There was a little effect on initial polymerization rate and the overall conversion with PDMC concentration. As the PDMC concentration ranged from 0 to 0.5%, the relative molecular weight increased and both particle size and the viscosity of dispersion decreased. However, the relative molecular weight, particle size and the viscosity of dispersion both increased when the PDMC concentration was higher than 1%. The stable conditions for CPAM aqueous two-phase system were as follows: 8~15% for monomers concentrations, 15~25% for PEG 20000, 0.5~1.5% for PDMC. Meanwhile, the formation process was investigated by optical microscope.

Finally, it should be noted that keeping lower viscosity and avoiding the Wessenberg effect (when the system viscosity reached a certain value, the pole-climbing phenomenon would occur) during the CPAM aqueous two-phase polymerization was a key point to the dispersion polymerization in inorganic salt solution.

Acknowledgements

The authors would like to acknowledge financial supports by the National Natural Science Foundation of China (No. 20876081), Shandong Provincial Natural Science Foundation, China (No. Q2006B01) and Shandong Provincial Sci-Tech Plan Foundation(J08LC04).

References

[1] Cho M. S., Yoon K. J., Song B. K.: Dispersion polymerization of acrylamide in aqueous solution of ammonium sulfate: Synthesis and characterization. Journal of Applied Polymer Science, **83**, 1397–1405 (2002).
DOI: 10.1002/app.2300

[2] McCormick C. L., Blackmon K. P., Elliott D. L.: Water-soluble copolymers. XIII. Copolymers of acrylamide with sodium-3-acrylamido-3-methylbutanoate: Solution properties. Journal of polymer Science Part A: Polymer Chemistry, **24**, 2619–2634 (1986).
DOI: 10.1002/pola.1986.080241019

[3] Fan A., Turro N. J., Somasundaran P.: A study of dual polymer flocculation. Colloids and Surfaces A: Physicochemical and Engineering Aspects, **162**, 141–148 (2000).
DOI: 10.1016/S0927-7757(99)00252-6

[4] Yan R. X.: Water soluble polymer. Chemical Industry Press, Beijing (1998).

[5] Fang D. B., Guo R. W., Ha R. H.: Acrylamide polymer. Chemical Industry Press, Beijing (2006).

[6] Wu Y. M., Chen Q. F., Xu J., Bi J. M.: Aqueous dispersion polymerization of acrylamide with quaternary ammonium cationic comonomer. Journal of Applied Polymer Science, **108**, 134–139 (2008).
DOI: 10.1002/app.27464

[7] Guha S., Mandal B. M.: Dispersion polymerization of acrylamide: III. Partial isopropyl ester of poly(vinyl methyl ether-alt-maleic anhydride) as a stabilizer. Journal of Colloid and Interface Science, **271**, 55–59 (2004).
DOI: 10.1016/j.jcis.2003.10.023

[8] Song B. K., Cho M. S., Yoon K. J., Lee D. C.: Dispersion polymerization of acrylamide with quaternary ammonium cationic comonomer in aqueous solution. Journal of Applied Polymer Science, **87**, 1101–1108 (2003).
DOI: 10.1002/app.11559

[9] Ray B., Mandal B. M.: Dispersion polymerization of acrylamide: Part II. 2,2′-azobisisobutyronitrile initiator. Journal of Polymer Science Part A: Polymer Chemistry, **37**, 493–499 (1999).
DOI: 10.1002/(SICI)1099-0518(19990215)37:4<493::AID-POLA13>3.0.CO;2-Y

[10] Chen D., Liu X., Yue Y., Zhang W., Wang P.: Dispersion copolymerization of acrylamide with quaternary ammonium cationic monomer in aqueous salts solution. European Polymer Journal, **42**, 1284–1297 (2006).
DOI: 10.1016/j.eurpolymj.2005.12.007

[11] Ye Q., Zhang Z., Ge X.: Highly efficient flocculant synthesized through the dispersion copolymerization of water-soluble monomers induced by γ-ray irradiation: Synthesis and polymerization kinetics. Journal of Applied Polymer Science, **89**, 2108–2115 (2003).
DOI: 10.1002/app.12356

[12] Yankov D. S., Trusler J. P. M., Yordanov B. Y., Stateva R. P.: Influence of lactic acid on the formation of aqueous two-phase systems containing poly(ethylene glycol) and phosphates. Journal of Chemical and Engineering Data, **53**, 1309–1315 (2008).
DOI: 10.1021/je800016r

[13] Zhang Y., Trabbic-Carlson K., Albertorio F., Chilkoti A., Cremer P. S.: Aqueous two-phase system formation kinetics for elastin-like polypeptides of varying chain length. Biomacromolecules, **7**, 2192–2199 (2006).
DOI: 10.1021/bm060254y

[14] Hatti-Kaul R.: Aqueous two-phase systems: A general overview. Molecular Biotechnology, **19**, 269–272 (2001).
DOI: 10.1385/MB:19:3:269

[15] Schindler J., Lewandrowski U., Sickmann A., Friauf E.: Aqueous polymer two-phase syetem for the proteomic analysis of plasma membranes from minute brain samples. Journal of Proteome Research, **7**, 432–442 (2008).
DOI: 10.1021/pr0704736

[16] Kawaguchi S., Ito K.: Dispersion polymerization. Advances in Polymer Science, **175**, 299–328 (2005).
DOI: 10.1007/b14102

[17] Shan G. R., Cao Z. H.: A new polymerization method and kinetics for acrylamide: Aqueous two-phase polymerization. Journal of Applied Polymer Science, **111**, 1409–1416 (2009).
DOI: 10.1002/app.29167

[18] Xu J., Wu Y., Wang C., Wang Y.: Dispersion polymerization of acrylamide with 2-acrylamide-2-methyl-1-propane sulfonate in aqueous solution of sodium sulfate. Journal of Polymer Research, **16**, 569–575 (2009).
DOI: 10.1007/s10965-008-9261-8

[19] Colombani D.: Chain-growth control in free radical polymerization. Progress in Polymer Science, **22**, 1649–1720 (1997).
DOI: 10.1016/S0079-6700(97)00022-1

eXPRESS Polymer Letters Vol.4, No.5 (2010) 284–291
Available online at www.expresspolymlett.com
DOI: 10.3144/expresspolymlett.2010.36

Effect of solution-blended poly(styrene-co-acrylonitrile) copolymer on crystallization of poly(vinylidene fluoride)

Q. Xia[1], *X. J. Zhao*[1], *S. J. Chen*[1], *W. Z. Ma*[1], *J. Zhang*[1*], *X. L. Wang*[2]

[1]College of Materials Science and Engineering, Nanjing University of Technology, Nanjing, 210009, China
[2]Department of Chemical Engineering, Tsinghua University, Beijing 100084, China

Received 16 December 2009; accepted in revised form 5 March 2010

Abstract. Effect of solution-blended poly(styrene-co-acrylonitrile) (SAN) copolymer on crystallization of poly(vinylidene fluoride) (PVDF) was investigated by Fourier transform infrared spectroscopy (FTIR), differential scanning calorimetry (DSC) and wide angle X-ray diffraction (WAXD). Acrylonitrile segment in SAN copolymer was partially miscible with PVDF. Styrene segment in SAN reduced the copolymer's polarity and its miscibility with PVDF. FTIR and WAXD tests both showed as-prepared PVDF was mainly β-phase. We employed an index A_β divided by X_c, suggesting that blended SAN could decrease the content of β-phase of PVDF. By DSC, the smaller content of PVDF made the system more miscible so that the $T_{g,SAN}$ of pure SAN decreased from 86.6 to 81.6°C of sample PVDF/SAN = 20/80; further increase PVDF to 50/50, the $T_{g,SAN}$ had a relative increase to be 84.2°C. However, for SAN by melt molding, $T_{g,SAN}$ increased with the increase of PVDF content, which might be due to the incorporation of SAN into inter-spacing of PVDF lamellae, because PVDF molecular chains had not enough mobility to retreat from the SAN's embrace and crystallize despite of the exit of SAN.

Keywords: *polymer blends and alloys, poly(vinylidene fluoride), poly(styrene-co-acrylonitrile), solution crystallization, melt crystallization*

1. Introduction

Poly(vinylidene fluoride) (PVDF) is known for its polymorphism of five crystalline phases with different conformations, like all trans (TTTT) planar zigzag for β-phase, TGTG' for α- and δ-phases and T_3GT_3G' for γ- and ε-phases [1, 2]. If the PVDF chains pack in crystals to form parallel dipoles, the crystal possesses a net dipole moment as in polar form β-, γ- and δ-phases; whereas, in antiparallel chain dipoles, the net dipole moment vanishes as in non-polar α- and ε-phases [3]. α- and β-phases are most popular among the five. α-phase is obtained directly from the melt [4–6] and β-phase is usually obtained from solution under 70°C [7] or by the mechanical stretching of α-phase films to a certain percent elongation at a given temperature.

PVDF can be blended with hydrophilic or polar polymers, such as poly(methyl methacrylate) (PMMA) [8, 9], poly(vinylpyrrolidone) (PVP) [10], polyacrylonitrile (PAN) [11], poly(vinyl acetate) (PVAc) [12], poly(3-hydroxybutyrate) (PHB) [13] to improve its hydrophilicity. From an exclusively thermodynamic point of view, the blends may be classified as miscible, partially miscible, and immiscible systems [14]. Among these polymers, PMMA (at- or syn-) was miscible with PVDF; PAN was partially miscible with PVDF. Besides these homopolymers, more and more attention has been concentrated onto copolymers, like PMMA-b-PEO, or others. We also used poly(styrene-co-acrylonitrile) (SAN) copolymer to melt blend with PVDF in our previous works. The

*Corresponding author, e-mail: zhangjun@njut.edu.cn

miscibility of PVDF/SAN (acrylonitrile content = 26 wt%) blends, lamellar thickness, the crystallinity and the hydrophilicity of PVDF depended on the content of SAN, and only α-phase PVDF was obtained from the melt crystallization [15].

In this work, the solution casting method was used to prepare the PVDF/SAN blend with an acrylonitrile content of 33 wt% in solvent N,N-dimethylformamide (DMF). The effects of adding SAN on the crystallization behavior and crystal structure of PVDF was studied. Differential scanning calorimetry (DSC) was used to study the crystallization behaviors of PVDF in the blend. The crystal structures and forms were determined by wide angle X-ray diffraction (WAXD) and Fourier transform infrared spectroscopy (FTIR).

2. Experimental

2.1. Materials

PVDF ($\bar{M}_w$ = 371000, $\bar{M}_w/\bar{M}_n$ = 2.5) was supplied by Elf Atochem of North America Inc. (USA). SAN (acrylonitrile content is 33 wt%) was purchased from Zhenjiang Guoheng Chemical Co., Ltd (China). DMF was obtained from Sinopharm Chemical Reagent Co., Ltd (China). All the chemicals are used as received.

2.2. Film preparation

Homogeneous solutions were obtained by dissolving the blends with different PVDF content (100, 90, 80, 70, 50, 20 and 0 wt%) in DMF at 50°C. The initial polymer concentration of the solution was 5 wt%. After evaporation of the solvent for 24 h at 50°C in a vacuum oven, the films were peeled from the glass substrates. The melt blending of PVDF/SAN was prepared at 180°C using a torque rheogoniometer (Shanghai Kechuang Machinery XSS-300, China) with the rotor speed of 60 r/min for 5 min and with different PVDF content (100, 90, 80, 70, 50, 20 and 0 wt%).

2.3. Characterization techniques

FTIR spectroscopy was performed using spectrometer (Vector-22, Bruker, Germany) with a nominal resolution of 4 cm^{-1} at 32 scans. The content of β-phase was characterized by the absorbance ratio A_β of the FTIR absorption peaks at 839 cm^{-1} and peaks at 2980 cm^{-1} as Equation (1):

$$A_\beta = \frac{A_{839}}{A_{2980}} \tag{1}$$

where A_{839} represented the FTIR absorbance peak height at 839 cm^{-1}, characteristic of β-phase. The absorbance peak height at 2980 cm^{-1} (independent on the crystalline phase of PVDF [16] and SAN contents) was regarded as constant.

DSC was conducted using a TA Instruments Q-200 (USA) under a dry nitrogen atmosphere. The sample (10 mg) was first heated from room-temperature to 200°C at a rate of 10°C/min and kept at this temperature for 3 min to eliminate thermal history, followed by the scan to 0°C at a cooling rate of 5°C/min, finally a heating rate of 10°C/min to 200°C. The degree of crystallinity X_c was evaluated according to Equation (2) [17]:

$$X_c = \frac{\Delta H_f / \phi}{\Delta H_f^*} \cdot 100\% \tag{2}$$

where ΔH_f was the endothermic heat during the melting process and ΔH_f^* was the heat fusion of a perfect crystal, taken as 104.5 J/g [18] for PVDF. ϕ was the weight fraction of PVDF in the blend.

WAXD was done in a Shimadzu XRD-6000 diffractometer (Japan) with the current of 30 mA, the accelerating voltage of 40 kV, and the scanning velocity of 4°/min with 0.04° steps over the 2θ ranged from 5~50° using Cu-K_α radiation. For further analysis, the interplanar spacing d and the lamellar thickness L were calculated according to Equations (3) and (4) [19]:

$$d = \frac{\lambda}{2\sin\theta} \tag{3}$$

$$L = \frac{k\lambda}{\varphi\cos\theta} \tag{4}$$

where λ is the wavelength of the X-ray, taken as 0.1542 nm; θ is the half of the scanning angle; k is Scherrer constant, taken as 1; and φ is the full width at half maximum (FWHM) of the diffraction peak.

3. Results and discussion

3.1. FTIR

FTIR spectra of two major phases (α- and β-phases) of PVDF has been under intensive investigation recently [20–22]. Vibrational bands at around 530 cm^{-1} (CF_2 bending), 615 and 765 cm^{-1} (CF_2 bending and skeletal bending) and 795 cm^{-1} (CH_2 rocking) refer to α-phase. Vibrational bands at around 510 cm^{-1} (CF_2 bending) and 839 cm^{-1} (CH_2 rocking) correspond to β-phase [16, 23].

Figure 1 shows the FTIR spectra of PVDF blends with different weight fractions of SAN (PVDF/SAN: a) 100/0; b) 90/10; c) 80/20; d) 70/30; e) 50/50; f) 20/80; g) 0/100) crystallized in DMF at 50°C. For PVDF, 3020 and 2980 cm^{-1} were attributed to the symmetrical and asymmetrical stretching vibration of CH_2 [16, 24]. For SAN, two peaks at 2930 and 2850 cm^{-1} corresponded to the CH_2 vibration. The vibration of C≡N band of SAN appeared at 2237 cm^{-1} [25]. The existence of styrene segment in the blends was represented by the aromatic C–H stretching at around 3010–3100 cm^{-1}, the out-of-plane hydrogen vibration at the 759 cm^{-1}, and the benzene ring C=C out-of-plane bending at 699 cm^{-1} [25, 26]. For PVDF as prepared, there also existed weak absorption peaks at 530, 613 and 763 cm^{-1} corresponded to α-phase. However, the absorption peaks at 530 and 763 cm^{-1} were overlapped with other absorption peaks from SAN when SAN content was increased over 20 wt%. Thus, the detailed crystal forms seemed unobservable from the FTIR spectra when SAN content increased.

In Figure 2, we employed an index A_β to detect the crystal forms of PVDF with solution-blended SAN. According to Figure 2, it was obvious that the content of β-phase of PVDF has a tendency to decrease with the increasing content of SAN. However, there also was a possibility: the whole degree of crystallinity of PVDF decreased with the increasing content of SAN, so that the decrease of β-phase happened. Considering this hypothesis, we divided A_β by X_c from Table 1 (later in chapter 3.2). It was also supporting the conclusion that blended SAN could decrease the content of β-phase of PVDF.

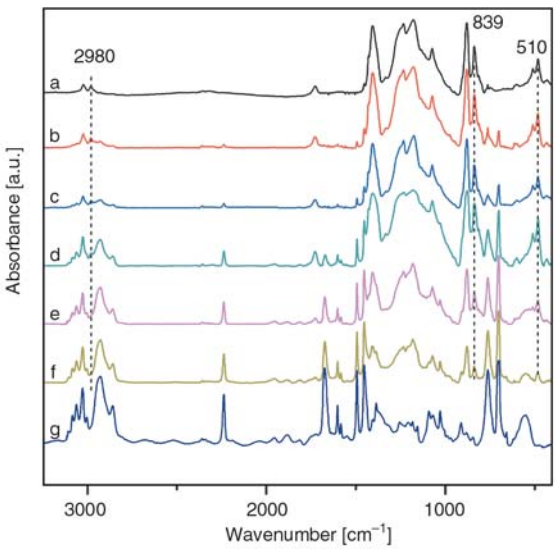

Figure 1. FTIR spectra of PVDF, SAN, and their blends with various mass ratios: a) 100/0; b) 90/10; c) 80/20; d) 70/30; e) 50/50; f) 20/80; g) 0/100

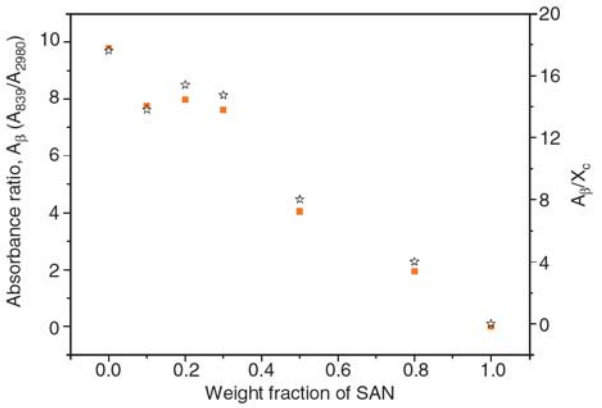

Figure 2. β phase content (■: A_β from Figure 1 and ★: A_β/X_c from Table 1) vs. SAN weight fraction of PVDF/SAN blends

Table 1. DSC data of melting traces of PVDF/SAN blends under solution molding with various mass ratios

Sample PVDF/SAN	$T_{g,SAN}$ [°C]	T_m^{on} [°C]	T_m^p [°C]	T_m^f [°C]	ΔT_m [°C]	ΔH_m [J/g]	X_c [%]
100/0	–	147.0	169.6	176.3	29.3	58.01	55.51
90/10	–	146.6	169.1	176.5	29.9	52.76	56.10
80/20	–	146.2	168.9	175.6	29.4	43.28	51.77
70/30	–	145.4	167.8	174.3	28.9	37.81	51.69
50/50	84.2	143.6	166.1	173.3	29.7	26.36	50.45
20/80	81.6	143.3	163.0	169.8	26.5	10.09	48.28
0/100	86.6	–	–	–	–	–	–

T_m^{on}: onset melting temperature of PVDF; T_m^p: peak melting temperature of PVDF; T_m^f: final melting temperature of PVDF; $\Delta T_m = T_m^f - T_m^{on}$; ΔH_m: melting enthalpy of blend; X_c: crystallinity of PVDF

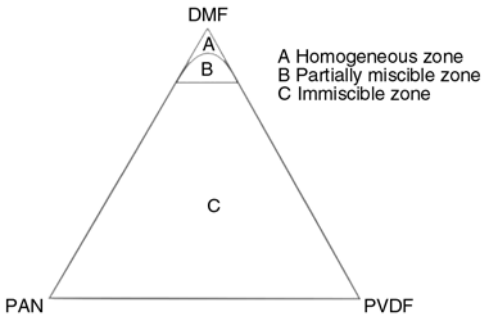

Figure 3. A schematic presentation of PVDF/PAN/DMF phase diagram [29]

In solution crystallization, dipoles of the mixtures had important effects on the crystallization of PVDF in the solution. The stronger dipolar interactions between PVDF and DMF might induce the *trans* conformation packing of CH_2–CF_2 dipoles of β-phase [27]. Mixtures with lower dipole moment resulted in the nonpolar α-phase [28]. Figure 3 is a schematic presentation of PVDF/PAN/DMF phase diagram which demonstrates that PAN and PVDF belong to partially miscible systems by adding small amount of PVDF or PAN into the solution [29]. SAN is a copolymer of styrene and acrylonitrile comonomer. The nonpolar styrene segment in SAN copolymer further reduces the homogenous and partially miscible zones. However, this nonpolar styrene also reduces the number of dipoles in the mixtures which favors the formation the nonpolar α-phase [28]. As used SAN has 33 wt% AN, in the sample of 10 wt% SAN blended PVDF mixture, there is 3.3 wt% AN which might have good miscibility with PVDF. So that nonpolar styrene around acrylonitrile comonomer has more effect on the crystallization of PVDF. In Figure 2, the observation that A_β has an abrupt decrease for 10 wt% SAN blended PVDF mixture could be interpreted by the above analysis.

3.2. DSC

Figure 4 presents DSC melting traces of PVDF/SAN blends obtained under solution molding with various mass ratios (a) 100/0; b) 90/10; c) 80/20; d) 70/30; e) 50/50; f) 20/80; g) 0/100). The detailed data derived from Figure 4 were listed in Table 1.

As shown in Figure 4, when SAN content exceeded 50 wt%, glass transition temperature of SAN ($T_{g,\mathrm{SAN}}$) became discernable. The glass transition

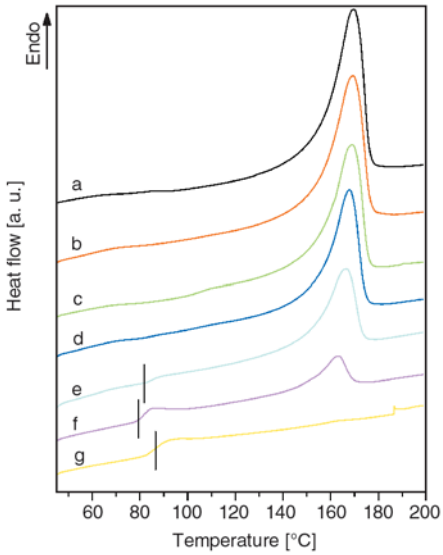

Figure 4. DSC melting traces of PVDF/SAN blends under solution molding with various mass ratios: a) 100/0; b) 90/10; c) 80/20; d) 70/30; e) 50/50; f) 20/80; g) 0/100

temperature of PVDF was –39°C [30]. The glass transition temperature of SAN was 86.6°C in Table 1. For the sample of PVDF/SAN = 20/80, the small content of PVDF also made the system partially miscible according to Figure 3, so that the $T_{g,\mathrm{SAN}}$ decreased to 81.6°C; but for sample of PVDF/SAN = 50/50, miscibility decreased so that the $T_{g,\mathrm{SAN}}$ had a relative increase to be 84.2°C compared with the sample of PVDF/SAN = 20/80.

For pure PVDF crystallized from 5 wt% DMF solution, the single melting peak at about 169.6°C can be attributed to the melting of β-phase with small amounts of α-phase [7, 23, 31, 32]. As SAN content increased in the blends, the melting enthalpy and melting point decreased. In Table 1, the influence of SAN component on PVDF crystallization was decreasing the onset of melting temperature (T_m^{on}), the final melting temperature (T_m^f) and the peak melting temperature (T_m^p). Small amount of SAN of 10 wt% did not show any effect on the crystallinity of PVDF. When SAN exceeded 20 wt%, it decreased X_c by about 4–5%. The crystallinity of PVDF had the tendency to decrease with increase of SAN content in the blends. However, the lower acrylonitrile content based PVDF/SAN (D-178, acrylonitrile content = 26 wt%) is a partially miscible system [15]. In this work, the higher acrylonitrile units in SAN (D-168, acrylonitrile content = 33 wt%) result in worse miscibility. In addition, the low concentration (5 wt%) solution,

which results in the good mobility of the PVDF molecular chains, also favors the crystallization of PVDF. PVDF can crystallize independently in a wide range of concentration. Therefore, the difference in the crystallinity of PVDF in the blends cannot be so remarkable. Likewise, the $\Delta T_m = T_m^f - T_m^{on}$ also had no distinct changes, which suggested that blending SAN did not decrease the crystal homogeneity of PVDF, except the sample with a SAN content of 80 wt%.

For comparability, DSC melting traces of PVDF/SAN blends after eliminating thermal history with various mass ratios (PVDF/SAN: a) 100/0; b) 90/10; c) 80/20; d) 70/30; e) 50/50; f) 20/80; g) 0/100) are shown in Figure 5. The detailed data derived from Figure 5 were listed in Table 2. These PVDF/SAN blends were prepared by melt molding as in our previous work [15].

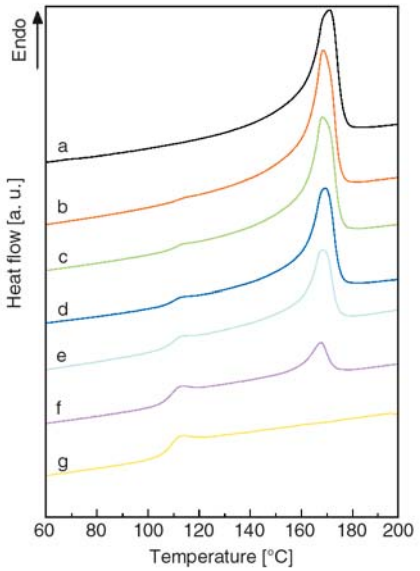

Figure 5. DSC melting traces of PVDF/SAN blends after eliminating thermal history with various mass ratios: a) 100/0; b) 90/10; c) 80/20; d) 70/30; e) 50/50; f) 20/80; g) 0/100.

For pure SAN by melt molding, $T_{g,SAN}$ was 109.3°C. For sample of PVDF/SAN = 80/20 by melt molding, $T_{g,SAN}$ was 111.2°C. As PVDF content increased, $T_{g,SAN}$ had an obvious increase. This situation is contrast to that obtained by solution casting. A reasonable explanation should consider the incorporation of SAN into inter spacing of PVDF lamellae, which was similar to the PVDF/PMMA system [9]. When PVDF/SAN blends were prepared by casting from 5 wt% DMF solution, viscosity was low and PVDF molecular chains had mobility to retreat from the SAN's embrace; however, when PVDF/SAN blends were prepared by melt molding, viscosity was high and PVDF molecular chains had less mobility to crystallize despite of the exit of SAN. So with decreasing of SAN content, the ratio of incorporated PVDF increased and the $T_{g,SAN}$ increased. Besides, $T_{g,SAN}$ by solution casting was much lower than $T_{g,SAN}$ by melt molding, which might be attributed to the entanglement which has been intensively studied [33, 34]. In Table 2, the addition of SAN did not show obvious effect on the melting temperatures of PVDF until SAN exceeded 20 wt%, which resulted in similar $\Delta T_m = T_m^f - T_m^{on}$. However, the crystallinity X_c of PVDF crystallized from the melt increases from 41.58 to 47.41% by a little incorporation of SAN (≤10 wt%). And at higher addition, it is reduced. The change of X_c in Table 2 could also be explained based on the hypothesis of incorporation of SAN into inter spacing of PVDF lamellae. The partially miscible SAN had mobility when PVDF began to crystallize before 111.2°C. In other words, SAN could be the diluent when PVDF began to crystallize, especially SAN was small amount of the blends because of the above-mentioned reason. Therefore, the crystallinity of PVDF in blends in Table 2 were mostly higher that that of the pure

Table 2. DSC melting results of PVDF/SAN blends after eliminating thermal history with different compositions

Sample PVDF/SAN	$T_{g,SAN}$ [°C]	T_m^{on} [°C]	T_m^p [°C]	T_m^f [°C]	ΔT_m [°C]	ΔH_m [J/g]	X_c [%]
100/0	–	160.7	171.0	176.4	15.7	43.45	41.58
90/10	–	161.2	168.4	175.1	13.9	44.59	47.41
80/20	111.2	160.9	168.1	175.2	14.3	38.85	46.47
70/30	110.6	160.4	169.1	175.0	14.6	33.57	45.89
50/50	110.0	160.3	168.1	174.3	14.0	22.22	42.53
20/80	109.6	158.4	167.6	172.8	14.4	8.47	40.52
0/100	109.3	–	–	–	–	–	–

T_m^{on}: onset melting temperature of PVDF; T_m^p: peak melting temperature of PVDF; T_m^f: final melting temperature of PVDF; $\Delta T_m = T_m^f - T_m^{on}$; ΔH_m: melting enthalpy of blend; X_c: crystallinity of PVDF

PVDF obtained by melt molding, except the sample of PVDF/SAN = 20/80, which was probably because too much SAN restricted the mobility of PVDF chains.

3.3. WAXD

The wide angle X-ray diffraction of PVDF/SAN blends are shown in Figure 6. The diffraction peak at 2θ of about 20.5° is corresponding to the (110) and (200) combined reflections of the β-form [23, 35] and the small peak at about 40° is assigned to the combined reflections of (201) and (111) planes of the β-phase [36]. It is demonstrated that all the solution cast samples, regardless of the various SAN weight fractions in the blend, present predominantly the β-phase. The two peaks here both decreased their intensity when the SAN was added, especially for the peak at 2θ of about 40°, when the content of SAN was larger than 20 wt%, it even disappeared. WAXD results further confirm that the addition of SAN hinders the crystallization of PVDF. According to the FTIR results, solution crystallized samples with a little incorporation of SAN (≤10 wt%) presents β-phase with a small amount of α-phase, but it is so little that it can just be detected by FTIR measurement. WAXD result demonstrates that β-phase of PVDF is present predominantly in solution crystallized samples.

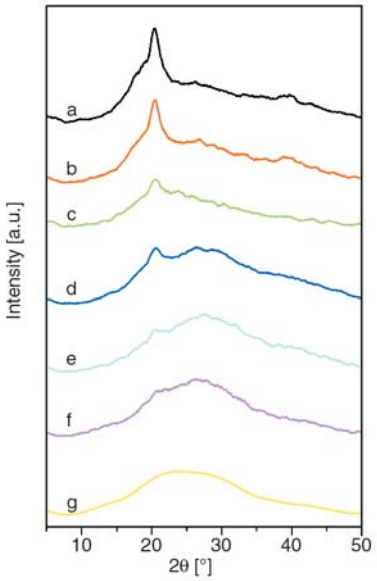

Figure 6. X-ray diffractograms of PVDF/SAN blends under solution molding with different mass ratios: a) 100/0; b) 90/10; c) 80/20; d) 70/30; e) 50/50; f) 20/80; g) 0/100.

Detailed data of WAXD are listed in Table 3. As shown in Table 3, there was no distinct change for *d* value between the different samples, i.e., the lattices parameter of the β-phase was not affected by SAN. All the observed *L* values were higher than that of the neat PVDF. The results were similar to those obtained from PVDF/PMMA blend [9]. In the miscible binary blend system including crystalline and non-crystalline component, the non-crystalline component can be sandwiched in the regions between lamella; that is the lamellar thickness *L* increases as the non-crystalline polymer composition increases [9, 37].

4. Conclusions

In this study, FTIR, DSC and WAXD were used to characterize the effect of solution-blended SAN with acrylonitrile content 33 wt% on the crystallization of PVDF. By FTIR, typical 510 and 839 cm^{-1} was corresponded to the β-phase of PVDF in the PVDF/SAN blends. There also existed weak absorption peaks at 530, 613 and 763 cm^{-1} corresponding to α-phase. Blended SAN could decrease the content of β-phase of PVDF from the index A_β/X_c. Nonpolar styrene reduced the dipoles of the mixtures which favored the formation the nonpolar α-phase. Through the DSC analysis, the smaller content of PVDF made the system more miscible so that the $T_{g,SAN}$ of pure SAN decreased

Table 3. WAXD data of PVDF/SAN blends under melt molding with various mass ratios

Sample PVDF/SAN	hkl (110, 200)			hkl (201, 111)		
	2θ [°]	d [Å]	L [Å]	2θ [°]	d [Å]	L [Å]
100/0	20.40	4.35	67.7	39.72	2.27	391.4
90/10	20.36	4.36	81.3	39.87	2.26	306.4
80/20	20.36	4.36	74.8	39.80	2.26	–
70/30	20.44	4.34	–	39.57	2.27	–
50/50	–	–	–	–	–	–
20/80	–	–	–	–	–	–
0/100	–	–	–	–	–	–

–: not observed; θ: bragg angle; *d*: the interplanar distance; *L*: the thickness of the lamellar crystal (1 Å = 10^{-10} m)

from 86.6 to 81.6°C of sample PVDF/SAN = 20/80; further adding PVDF to 50/50, the $T_{g,SAN}$ had a relative increase to be 84.2°C. However, for SAN obtained by melt molding, $T_{g,SAN}$ increased with the increase of PVDF content, which might be due to the incorporation of SAN into inter spacing of PVDF lamellae because PVDF molecular chains had not enough mobility to retreat from the SAN's embrace and crystallize despite of the exit of SAN. According to the WAXD analysis, all the solution casting samples, regardless of the various SAN weight fractions in the blend, present predominantly the β-phase.

Acknowledgements

This work is supported by the National Basic Research Program of China under contract No. 2009CB623404.

References

[1] Broadhurst M. G., Davis G. T., McKinney J. E.: Piezoelectricity and pyroelectricity in polyvinylidene fluoride – A model. Journal of Applied Physics, **49**, 4992–4997 (1978).
DOI: 10.1063/1.324445

[2] Lovinger A. J.: Annealing of poly(vinylidene fluoride) and formation of a fifth phase. Macromolecules, **15**, 40–44 (1982).
DOI: 10.1021/ma00229a008

[3] Salimi A., Yousefi A. A.: Analysis method: FTIR studies of β-phase crystal formation in stretched PVDF films. Polymer Testing, **22**, 699–704 (2003).
DOI: 10.1016/S0142-9418(03)00003-5

[4] Jungnickel B. J.: Poly (vinylidene fluoride). in 'Polymeric materials handbook' (ed.: Salamone J.C.) CRC Press Inc, NewYork, 7115–7122 (1999).

[5] El Mohajir B-E., Heymans N.: Changes in structural and mechanical behaviour of PVDF with processing and thermomechanical treatments. 1. Change in structure. Polymer, **42**, 5661–5667 (2001).
DOI: 10.1016/S0032-3861(01)00064-7

[6] Sajkiewicz P., Wasiak A., Goclowski Z.: Phase transitions during stretching of poly(vinylidene fluoride). European Polymer Journal, **35**, 423–429 (1999).
DOI: 10.1016/S0014-3057(98)00136-0

[7] Gregorio J. R., Cestari M.: Effect of crystallization temperature on the crystalline phase content and morphology of poly(vinylidene fluoride). Journal of Polymer Science Part B: Polymer Physics, **32**, 859–870 (1994).
DOI: 10.1002/polb.1994.090320509

[8] Huang C., Zhang L.: Miscibility of poly(vinylidene fluoride) and atactic poly(methyl methacrylate). Journal of Applied Polymer Science, **92**, 1–5 (2004).
DOI: 10.1002/app.13564

[9] Ma W., Zhang J., Wang X., Wang S.: Effect of PMMA on crystallization behavior and hydrophilicity of poly(vinylidene fluoride)/poly(methyl methacrylate) blend prepared in semi-dilute solutions. Applied Surface Science, **253**, 8377–8388 (2007).
DOI: 10.1016/j.apsusc.2007.04.001

[10] Chen N. P., Hong L.: Surface phase morphology and composition of the casting films of PVDF-PVP blend. Polymer, **43**, 1429–1436 (2002).
DOI: 10.1016/S0032-3861(01)00671-1

[11] Liu T-Y., Lin W-C., Huang L-Y., Chen S-Y., Yang M-C.: Surface characteristics and hemocompatibility of PAN/PVDF blend membranes. Polymers for Advanced Technologies, **16**, 413–419 (2005).
DOI: 10.1002/pat.592

[12] Chiu H-J.: Spherulitic morphology and crystallization kinetics of poly(vinylidene fluoride)/poly(vinyl acetate) blends. Journal of Polymer Research, **9**, 169–174 (2002).
DOI: 10.1023/A:1021387524243

[13] Liu J. P., Jungnickel B-J.: Crystallization and morphology of poly(vinylidene fluoride)/poly(3-hydroxybutyrate) blends. I. Spherulitic morphology and growth by polarized microscopy. Journal of Polymer Science Part B: Polymer Physics, **41**, 873–882 (2003).
DOI: 10.1002/polb.10454

[14] Linares A., Acosta J. L.: Compatibility studies of partially compatible blends through glass transition temperature and melting point depression analysis. Journal of Applied Polymer Science, **67**, 997–1004 (1998).
DOI: 10.1002/(SICI)1097-4628(19980207)67:6<997::AID-APP5>3.0.CO;2-H

[15] Ma W., Zhang J., Chen S., Wang X.: Crystallization behavior and hydrophilicity of poly (vinylidene fluoride) (PVDF)/poly (styrene-co-acrylonitrile) (SAN) blends. Colloid and Polymer Science, **286**, 1193–1202 (2008).
DOI: 10.1007/s00396-008-1889-8

[16] Bachmann M. A., Gordon W. L., Koenig J. L., Lando J. B.: An infrared study of phase-III poly(vinylidene fluoride). Journal of Applied Physics, **50**, 6106–6112 (1979).
DOI: 10.1063/1.325780

[17] Gu M., Zhang J., Wang X., Ma W.: Crystallization behavior of PVDF in PVDF-DMP system via thermally induced phase separation. Journal of Applied Polymer Science, **102**, 3714–3719 (2006).
DOI: 10.1002/app.24531

[18] Nakawa K., Ishida Y.: Annealing effects in poly(vinylidene fluoride) as revealed by specific volume measurements, differential scanning calorimetry, and electron microscopy. Journal of Polymer Science: Polymer Physics Edition, **11**, 2153–2171 (1973).
DOI: 10.1002/pol.1973.180111107

[19] Suryanarayana C., Grant N. M.: X-ray diffraction: A practical approach. Plenum Press, New York (1998).

[20] Gregorio R., Capitao R. C.: Effect of crystallization rate on the formation of the polymorphs of solution cast poly(vinylidene fluoride). Polymer, **49**, 4009–4016 (2008).
DOI: 10.1016/j.polymer.2008.07.010

[21] Buonomenna M., Macchi P., Davoli M., Drioli E.: Poly(vinylidene fluoride) membranes by phase inversion: The role the casting and coagulation conditions play in their morphology, crystalline structure and properties. European Polymer Journal, **43**, 1557–1572 (2007).
DOI: 10.1016/j.eurpolymj.2006.12.033

[22] Abdelrazek E. M., Elashmawi I. S., Soliman M. A., Aly A.: Physical properties of $MnCl_2$ fillers incorporated into a PVDF/PVC blend and their complexes. Journal of Vinyl and Additive Technology, **15**, 171–177 (2009).
DOI: 10.1002/vnl.20188

[23] Gregorio R.: Determination of the α, β, and γ crystalline phases of poly(vinylidene fluoride) films prepared at different conditions. Journal of Applied Polymer Science, **100**, 3272–3279 (2006).
DOI: 10.1002/app.23137

[24] Narula G. K., Rashmi, Pillai P. K. C.: Investigations of solution-mixed PVDF/PMMA polyblends by thermal, structural, and dielectric techniques. Journal of Macromolecular Science Part B: Physics, **28**, 25–49 (1989).
DOI: 10.1080/00222348908212326

[25] Choi Y. S., Xu M., Chung I. J.: Synthesis of exfoliated poly(styrene-co-acrylonitrile) copolymer/silicate nanocomposite by emulsion polymerization; Monomer composition effect on morphology. Polymer, **44**, 6989–6994 (2003).
DOI: 10.1016/j.polymer.2003.08.020

[26] Sun Y-P., Lawson G. E., Bunker C. E., Johnson R. A., Ma B., Farmer C., Riggs J. E., Kitaygorodskiy A.: Preparation and characterization of fullerene-styrene copolymers. Macromolecules, **29**, 8441–8448 (1996).
DOI: 10.1021/ma960579e

[27] He X., Yao K.: Crystallization mechanism and piezoelectric properties of solution-derived ferroelectric poly(vinylidene fluoride) thin films. Applied Physics Letters, **89**, 112909/1–112909/3 (2006).
DOI: 10.1063/1.2352799

[28] Benz M., Euler W. B., Gregory O. J.: The role of solution phase water on the deposition of thin films of poly(vinylidene fluoride). Macromolecules, **35**, 2682–2688 (2002).
DOI: 10.1021/ma011744f

[29] Olabisi O., Robeson L. M., Shaw M. T.: Polymer-polymer miscibility. Academic Press, New York, (1979).

[30] Seiler D. A.: PVDF in the chemical process industry. in 'Modern fluoropolymers' (ed.: Scheirs J.) Wiley, Chichester, 487–505 (1997).

[31] Campos J. S. C., Riberio A. A., Cardoso C. X.: Preparation and characterization of PVDF/$CaCO_3$ composites. Material Science and Engineering: B, **136**, 123–128 (2007).
DOI: 10.1016/j.mseb.2006.09.017

[32] Ma W., Zhang J., Chen S., Wang X.: Crystalline phase formation of poly(vinylidene fluoride) from tetrahydrofuran/N,N-dimethylformamide mixed solutions. Journal of Macromolecular Science Part B: Physics, **47**, 434–449 (2008).
DOI: 10.1080/00222340801954811

[33] Huang D. H., Yang Y. M., Zhuang G. Q., Li B. Y.: Influence of entanglements on the glass transition and structural relaxation behaviors of macromolecules. 1. Polycarbonate. Macromolecules, **32**, 6675–6678 (1999).
DOI: 10.1021/ma990581g

[34] Huang D. H., Yang Y. M., Zhuang G. Q., Li B. Y.: Influence of intermolecular entanglements on the glass transition and structural relaxation behaviors of macromolecules. 2. Polystyrene and phenolphthalein poly(ether sulfone). Macromolecules, **33**, 461–464 (2000).
DOI: 10.1021/ma990786p

[35] Davis G. T., McKinney J. E., Broadhurst M. G., Roth S. C.: Electric-field-induced phase changes in poly(vinylidene fluoride). Journal of Applied Physics, **49**, 4998–5002 (1978).
DOI: 10.1063/1.324446

[36] Lovinger A. J., Davis D. D., Cais R. E., Kometani J. M.: The role of molecular defects on the structure and phase transitions of poly(vinylidene fluoride). Polymer, **28**, 617–626 (1987).
DOI: 10.1016/0032-3861(87)90478-2

[37] Martuscelli E., Canetti M., Vicini L., Seves A.: First results of small and wide angle X-ray scattering of poly(ethylene oxide)/poly(methyl methacrylate) binary blends. Polymer, **23**, 331–334 (1982).
DOI: 10.1016/0032-3861(82)90328-7

eXPRESS Polymer Letters Vol.4, No.5 (2010) 292–299
Available online at www.expresspolymlett.com
DOI: 10.3144/expresspolymlett.2010.37

Influence of carbon nanotube clustering on the electrical conductivity of polymer composite films

J. O. Aguilar[1,2], *J. R. Bautista-Quijano*[1], *F. Avilés*[1*]

[1]Centro de Investigación Científica de Yucatán, Unidad de Materiales, Calle 43 No. 130 Col. Chuburná de Hidalgo, 97200, Mérida Yucatán, México
[2]Universidad de Quintana Roo, División de Ciencias e Ingeniería, Boulevard Bahía s/n esq. Ignacio Comonfort, Col. Del Bosque, 77019 Chetumal Quintana Roo, México

Received 6 January 2010; accepted in revised form 9 March 2010

Abstract. Electrical conductivity of 150–200 μm thick polysulfone films loaded with 0.05–0.75% w/w multiwall carbon nanotubes was systematically investigated for two types of dispersion states, uniformly dispersed and agglomerated at the micro-scale. The percolation threshold was found at 0.11% and 0.068% w/w for the uniformly dispersed and agglomerated films, respectively. Overall, the conductivity of the films with agglomerated nanotubes was higher than that of the uniformly dispersed ones, with marked differences of 2 to 4 orders of magnitude for carbon nanotubes loadings in the upper vicinity of the percolation threshold (0.1–0.3% w/w). The increased conductivity of the agglomerated state is explained by the increased nanotube-to-nanotube contact after the percolating network has formed, which facilitates electron transfer.

Keywords: *polymer composites, electrical conductivity, MWCNT, percolation, clustering*

1. Introduction

Carbon nanotube (CNT)-polymer composites have been aggressively investigated for more than a decade, given the extraordinary physical properties of CNTs and the versatility of polymeric materials. In recent years, a great deal of attention has been paid to the electrical properties of such composites, given the great promises that these materials hold as multifunctional materials in the area of electronics, sensors, and actuators [1–4]. Electrical conductivity of CNT-polymer nanocomposites using very low CNT weight loadings typically reaches the level of semiconductors (~0.001–0.1 S/m) [4–7]. The conductivity of these composites can reach up to several hundreds of S/m when CNTs are aligned or decorated [8, 9]. The critical CNT content required to form a percolation network depends mainly on the CNT type (single-wall carbon nanotube, SWCNT, or multi-wall carbon nanotube, MWCNT), intrinsic CNT quality (amorphous carbon content and ratio metallic/semi-conductive tubes), aspect ratio (*L*/*d*), morphology, polymer matrix and dispersion state, and hence the range of reported percolation thresholds for CNT-polymer systems is vast, see e.g. [4–11]. For the same polymer and CNT intrinsic quality, dispersion state and CNT aspect ratio have been recognized as the critical factors governing composite conductivity [11]. Using an epoxy-MWCNT system, Li *et al.* [11] found that when the CNT aspect ratio is larger than ~100, dispersion becomes the main factor controlling electrical percolation. Conventionally, it is accepted that a good CNT dispersion within the polymer enhances the physical properties of the composite [12, 13]. However, a few studies suggest that CNT agglomeration could favor the formation of a percolating network [11, 14, 15]. The great majority of these studies, however, are related to

*Corresponding author, e-mail: faviles@cicy.mx

bulk geometry, while the thin film configuration has been scarcely investigated. Conductive CNT composites in film geometry show a great potential in micro- and nano-electronics, micro-electro-mechanical systems (MEMS), nano-electro-mechanical systems (NEMS), and photoelectronics, among many others [16]. We report in this work compelling experimental evidence that shows that MWCNT agglomeration at the micro-scale significantly favors electrical conductivity of CNT-polymer composite films, especially for weight loadings in the upper vicinity of the percolation threshold.

2. Experimental

2.1. Synthesis of PSF-CNT films

Multiwall carbon nanotubes grown by chemical vapor deposition were supplied by Bayer Material Science[1] ('Baytubes C150P®'). The nanotubes have average inner and outer diameters of ~4 and ~13 nm, respectively, and length of 1–4 μm. SEM images of the MWCNTs employed can be found in a previous work [17]. Commercial polysulfone, PSF (UDEL P-1700®, volume resistivity = $3 \cdot 10^{16}$ Ω·cm), obtained from Solvay Advanced Polymers[2] was used to fabricate the polymer films. Prior to film fabrication PSF was dried in a convection oven at 150°C for 3.5 h. For film fabrication, approximately 2 g of PSF was dissolved in 10 ml of chloroform and stirred for 2 hours. Separately, a range of weight fractions (0.05–0.75% w/w) of the as-received MWCNTs were dispersed in chloroform using a conventional ultrasonic bath for 3–11 hours, depending on the MWCNT content. Details of solvent content and sonication time employed to disperse the CNTs in chloroform are listed in Table 1. The long sonicating times employed promote disentanglement of the CNT bundles at the nanoscale, see e.g. [11, 18]. Both solutions were then mixed and mechanically stirred for 30 min. The polymer/chloroform/CNT solution was then sonicated for 1 h and finally stirred again for 10 min prior to casting the viscous solution. Polymer films were cast onto a Petri dish and covered to slow the solvent evaporation rate, to form an homogeneous, well dispersed film with a uniform thickness of 150–200 μm. The group of films fabricated in this way will be hereafter referred to as 'uniformly dispersed'. To obtain the uniformly dispersed films, about 75% wt. of the employed chloroform was evaporated prior to solution casting, which yielded a rather viscous solution during casting. For the second group of PSF-CNT films ('agglomerated') reduced viscosity of the CNT/polymer/chloroform solution was achieved by decreasing the proportion of chloroform evaporated prior to casting to about 50% wt. This technique reduced the viscosity of the solution poured on the Petri dish and hence promoted CNT re-agglomeration right after casting. Apart from controlling the viscosity of the solution, the rest of the fabrication procedure and processing times employed for the 'agglomerated' films were identical to those used for the 'uniformly dispersed'ones. All films were dried at room temperature for 1 day after casting, and further dried in a vacuum oven at 100°C for 1 day. The final product was a composite film with a thickness of ~150–200 μm with randomly distributed MWCNTs. It is important to point out that, in the context of this work, the terms 'uniformly dispersed' and 'agglomerated' refer to a dimensional scale ranging from centimeters (macroscopic) to a few hundreds of microns. Below that dimensional scale, small clusters of CNTs are visible for both groups of films, as it will be further discussed.

Table 1. Amount of solvent and sonication time employed for composite film fabrication

% CNT	MWCNTS [mg]	Chloroform [ml]	Sonication time [h]
0.050	1.0	7	3
0.075	1.5	7	3
0.100	2.0	10	5
0.200	4.0	13	7
0.300	6.0	15	9
0.500	10.0	20	11
0.750	15.0	20	11

2.2. Electrical properties

Electrical conductivity of PSF-CNT films loaded with different weight fractions (0.05–0.75% w/w) of MWCNTs was measured at room temperature using a Fluke electrometer[3]. The electrometer is capable of measuring DC electrical resistance up to

[1]Bayer Material Science, Leverkusen, Germany. www.baytubes.com

[2]Solvay Advanced Polymers, LLC, Alpharetta, Georgia. www.solvayadvancedpolymers.com

[3]Fluke 1550B MegOhmMeter, Fluke Corporation, Everett, Washington

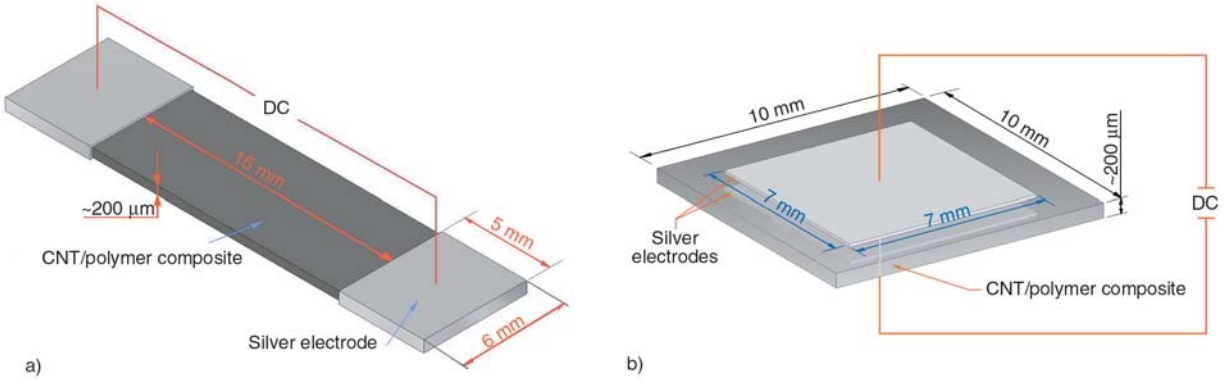

Figure 1. Schematic illustrations of the test specimens employed: a) CNT loadings >0.1% w/w, voltage is applied through the specimen length, b) CNT loadings 0.05–0.1% w/w, voltage is applied across the specimen thickness

1 TΩ. DC volumetric resistance (R) was measured using two silver paint[4] electrodes of 5 mm length painted on the film edges of 25 mm long specimens, leaving an effective span (L) of 15 mm between the silver electrodes, see Figure 1a. Specimen width was 6 mm and film thickness ~150–200 µm. To reduce surface effects in the measurements, silver paint electrodes were painted completely covering the ends of the sample. A DC voltage was applied through the length of the specimen and the conductivity (σ) was calculated using Equation (1):

$$\sigma = \frac{L}{AR} \tag{1}$$

where A is the cross sectional area of the sample and R the measured electrical resistance.

For specimens with CNT loadings <0.1% w/w the measured resistance exceeded the capacity of the electrometer (R > 1 TΩ) and a different method had to be employed for those samples. For those cases, measurements were conducted across the specimen thickness with back-to-back silver paint electrodes covering top and bottom square areas of 7 mm and leaving a non-painted trim of 3 mm along the edge of the samples, to minimize surface effects along the edges, see Figure 1b. Since the film thickness (~150–200 µm) is substantially larger than the largest CNT agglomerate (~20 µm), this configuration should yield bulk values of resistance, although small surface contributions may not be neglected. The application of a voltage through the film thickness allowed measurement of electrical resistance (R < 1 TΩ), which were converted into conductivity using Equation (1) with L as the film thickness and A as the 7×7 mm^2 in-plane area. Schematic representations of both specimens are depicted in Figure 1. Voltages employed in the resistivity measurements were 1000 V for 0.05 to 0.1% w/w, 500 V for 0.2–0.3% w/w and 250 V for 0.5–0.75% w/w. The percolation threshold was calculated using the well-known scaling law describing the statistical percolation behavior in the vicinity of the percolation limit (see Equation (2)), which refers to a situation where randomly distributed elongated rods form percolating paths:

$$\sigma = \sigma_0(\phi - \phi_c)^t \tag{2}$$

where σ_0 is a scaling factor that may be comparable to the effective conductivity of the filler [19, 20], ϕ is the CNT weight fraction, and ϕ_c is the percolation critical concentration. The parameter t is a critical exponent that governs the scaling law in the vicinity of percolation and has been associated to the dimensionality of the system, although its physical meaning is still controversial [10, 19]. The parameters t and ϕ_c were calculated by plotting logσ vs. log(ϕ–ϕ_c) and varying ϕ_c until the best linear fit is obtained, see e.g. [10, 19].

All properties of the composite films were measured after evaporation of the solvent, i.e. over a solid film. Thus, the percolation measured is a static (statistical) one, where CNTs cannot easily move inside the matrix. It has been reported that very low percolation limits can be achieved when the matrix posses a fluid-like state of low viscosity, where particles are able to move inside the polymeric matrix [21, 22]. This phenomenon is called dynamic (or kinetic) percolation and needs to be described by dynamic colloid theory [10, 21, 22].

[4]Pelco® conductive silver 187, Ted Pella. Inc. CA, USA

3. Results and discussion

The final dispersion state of CNTs within the polymer results from a competition between van der Waals interactions among the CNTs and the viscous forces acting within the polymer solution. Low viscosity facilitates dispersion during film processing but also promotes CNT re-agglomeration right after pouring the polymer in the mold, i.e., as soon as the external energy supplied for dispersion is suspended. On the other hand, high viscosity may make processing difficult but prevents CNT re-agglomeration after casting. Therefore, the dispersion state of the CNTs within the polymer film can be controlled by modifying the viscosity of the polymer/chloroform solution, as performed in this work.

The state of CNT dispersion at the macro- and micro-scales within the composite films was evaluated here using optical observations. Figure 2 shows photographs of the PSF-CNT films for selected weight fractions (columns) and the two examined dispersion states (rows), viz. uniformly dispersed (upper row) and agglomerated (lower row). Only selected weight loadings are shown in Figure 2 to depict the dispersion states. At the macro-scale, uniformly dispersed films appear as homogeneous materials with an optical transparency that decreases with increased CNT content. Agglomerated films, on the other hand, show CNT clusters with an apparent inter-cluster distance which diminishes with increased CNT content. The cluster distribution is rather uniform, with clusters in the sub-millimeter scale which tend to coalesce as the CNT concentration is increased. At this scale (millimeters), the different dispersion state of both groups of films is evident, even by naked eye.

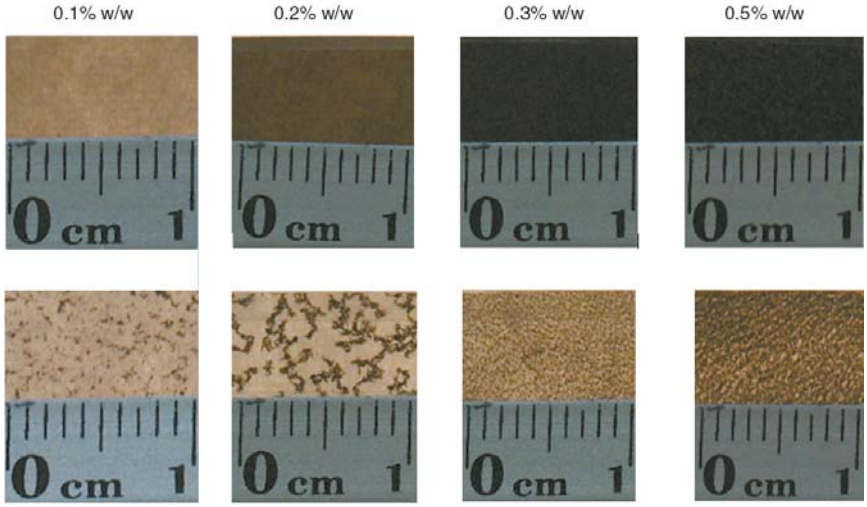

Figure 2. Millimeter-scale photographs of PSF-CNT films loaded with 0.1–0.5% w/w MWCNTs for two dispersion states: uniformly dispersed (upper row) and agglomerated (lower row)

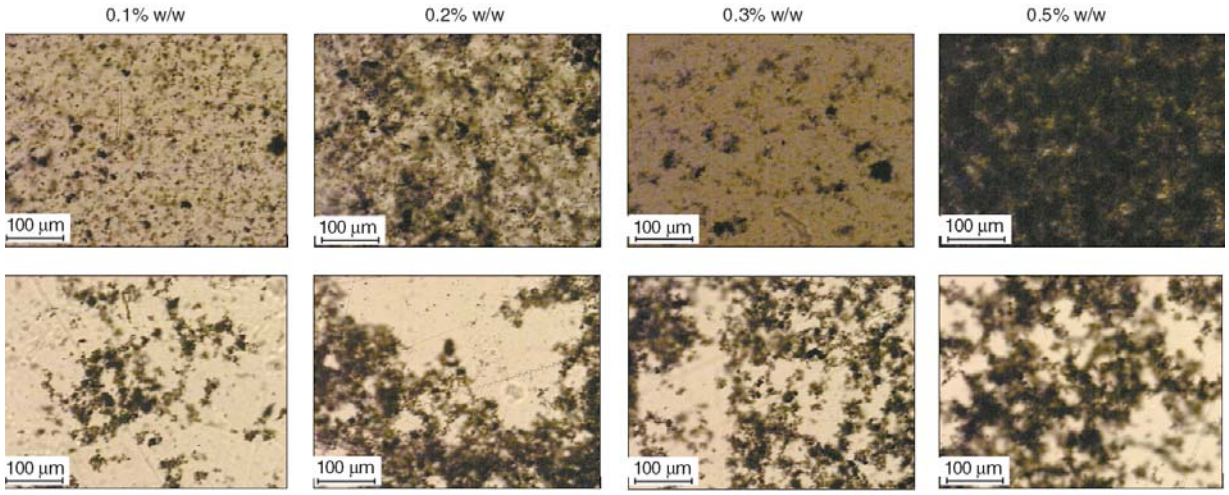

Figure 3. Optical microscopies of PSF-CNT films loaded with 0.1–0.5% w/w MWCNTs for two dispersion states: uniformly dispersed (upper row) and agglomerated (lower row)

Figure 3 presents optical micro-scale images of films with the same weight loadings as in Figure 2. At this scale (micrometers), small CNT clusters are observed. Interestingly, even the films that appear as homogeneous and uniformly dispersed at the macro-scale, show fine clusters at the micrometer scale, but cluster size is significantly larger for the agglomerated films when compared to the uniformly dispersed ones. For example, for 0.1% w/w loading the individual cluster size is about 10 μm for the uniformly dispersed films and about 25 μm for the agglomerated ones. Cluster size increases with increased CNT loading.

As observed from these figures, agglomeration promotes CNT-to-CNT interactions through surface contact (or tunneling) and hence it should increase the electrical conductivity of the composite, as it will be further discussed. In fact, as a parallel experiment, it was observed that when the film thickness is reduced to the order of the cluster size (~20 μm), relatively high electrical conductivity (~0.6 S/m) is achieved through the film thickness even for films loaded with only 0.05% w/w, which are not conductive in the in-plane (length) direction. This observation may lead to ultra-low percolation levels in the through-thickness direction of the film, especially for agglomerated films, but a detailed systematic investigation of this phenomenon falls beyond the scope of the present work. A similar phenomenon has been recently reported by Fu *et al.* [16], which states the percolation threshold can be reduced significantly if the film thickness is reduced to the length range of the CNTs. In that case, very low CNT loadings would be required to form a conductive path across the film thickness. In our case, the film thickness (~150–200 μm) is substantially larger than the CNT length (1–4 μm) and CNT agglomerate size (~20 μm), so through-thickness conduction does not occur for low CNT weight loadings.

Figure 4 shows electrical conductivity of the composite films as a function of weight loading for uniformly dispersed and agglomerated films. Overall, the conductivity of the agglomerated films is larger than that of the uniformly dispersed ones, irrespective of the CNT loading. At low CNT loadings (<0.1% w/w) the film is still an isolating material and the difference in conductivity between both dispersion states is almost indistinguishable. Around 0.1% w/w a sharp increase in conductivity

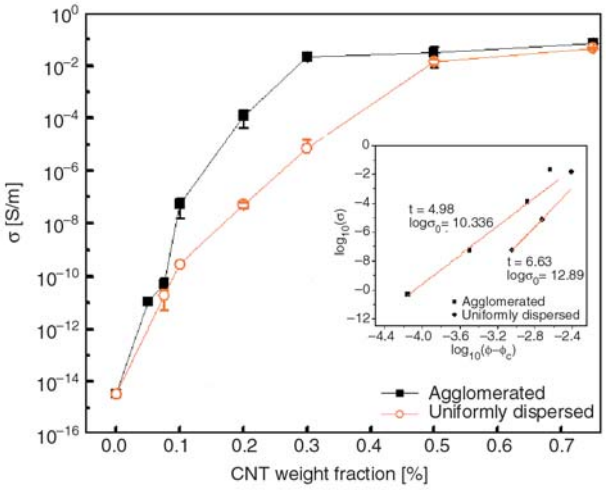

Figure 4. Electrical conductivity vs. CNT loading for uniformly dispersed and agglomerated films

is observed, indicating the formation of a percolation network. Percolation thresholds were calculated for both dispersion states fitting the measured data to the power law expression for conductivity of statistical percolation theory, Equation (2). For uniformly dispersed films, the percolation threshold (ϕ_c) and critical exponent (t) were found as 0.11% w/w and 6.63, respectively. On the other hand, for films with agglomerated CNTs, ϕ_c and t were found as 0.068% w/w and 4.98. Slightly above the percolation threshold (0.1–0.3% w/w), the difference in electrical conductivity between both dispersion states is large (2 to 4 orders of magnitude). At higher loadings (≥0.5% w/w), the conductivity of both dispersion states is again similar, since the conductive network has been well defined and no further drastic changes are expected according to percolation theory. Notice that the aspect ratio of the employed CNTs is in the range of ~80–300 and therefore the CNT dispersion state should be the most influential factor on the composite electric conductivity, according to a previous investigation by Li *et al.* [11].

Typical values of t reported for CNT-polymer composites are in the range of 1.3–4, see [10], although a few works report values of t of ~4.9 [23] and even higher than 7 [24]. Mathematically, since ϕ–ϕ_c is a small fraction (<1), a lower value of t in Equation (2) means more abrupt increments in electrical conductivity in the vicinity of percolation. The physical interpretation of the critical exponent t is more complex, and still a matter of controversy, as stated in a recent review by Bauhofer and Kovacs [10]. This exponent is frequently associated to the

system dimensionality, with values of $t \approx 1.3$ (or slightly higher) representing a two-dimensional network and $t \approx 2$ (or slightly higher) a three-dimensional one [10, 16, 20, 25]. However, the use of a scaling law for statistical percolation is limited to a concentration range very close to the percolation threshold and the use of this law to extract geometrical information about the CNT network from experimentally determined values of t is controversial, as stated by several authors [10, 18, 20]. In our case, the relatively high values of t obtained are due to the 'moderate' (2–4 orders of magnitude) changes in electrical conductivity in the vicinity of percolation, which might be related to geometrical constrains imposed by the limited thickness of the film and/or to the specific polymer employed.

The higher conductivity of the films in the agglomerated state compared to the 'uniformly dispersed' ones may be related to the increased CNT-to-CNT contact/junctions in the agglomerated state. The tunneling distance allowed for electron hopping has been reported between 5–30 nm [11, 26, 27]. Agglomeration may not significantly improve the conductivity of the composite before the CNT-to-CNT distance has reached at least this tunneling separation. Thus, the percolation threshold observed for both dispersion states investigated herein is somewhat similar. However, once the percolation network has been formed, CNT agglomeration increases the surface contact among CNTs (CNT-to-CNT junctions) and hence facilitates the electrons flow through the formed CNT network. Recent studies suggest that the electrical conductivity of CNT polymer composites can be improved by increasing the number of CNT-CNT junctions per unit area, which will improve the transport of free carriers between the nanotubes [28, 29].

For higher CNT loadings the conductive network is densely packed and no further increases in electrical conductivity are expected to be caused by this mechanism. Our experimental observations are also supported by a continuum micromechanics model developed by Seidel and Lagoudas [27], which suggests that increased CNT bundling promotes the formation of conductive networks and such a networks are primarily responsible for the conductivity in MWCNT composites.

4. Conclusions

The influence of CNT clustering on the electrical properties of polymer composite films was investigated using two dispersion states: uniformly dispersed and agglomerated at the micro-scale. For uniformly dispersed films, the percolation threshold (ϕ_c) and critical exponent (t) were found as 0.11% w/w and 6.63, respectively. On the other hand, for films with agglomerated CNTs, ϕ_c and t were found as 0.068% w/w and 4.98. It was found that films with micrometer-size agglomerations have a slightly lower percolation threshold and higher electrical conductivity than films with uniformly dispersed MWCNTs, especially for CNT loadings in the upper vicinity of the percolation threshold (0.1–0.3% w/w). The increased conductivity of the agglomerated state is explained by the increased density of CNT-to-CNT junctions after the percolating network has formed, which favors the formation of conductive networks.

Acknowledgements

This work was supported by CONACyT (Mexico) Grant No. 79609 of Dr. F. Avilés. J. O. Aguilar is thankful to CONACyT for the granted postdoctoral fellowship at CICY. Raw PSF was kindly provided by 'Solvay Advanced Polymers', through Dr. Javier Leal. Technical assistance of Alejandro May (CICY) with sample preparation and Oscar Ceh (CINVESTAV) with electrical conductivity measurements is also strongly appreciated. We also thank Dr. Juan Cauich and Dr. Manuel Aguilar for their insightful comments.

References

[1] Li C., Thostenson E. T., Chou T. W.: Sensors and actuators based on carbon nanotubes and their composites: A review. Composites Science and Technology, **68**, 1227–1249 (2008). DOI: 10.1016/j.compscitech.2008.01.006

[2] Park C., Ounaies Z., Watson K. A., Pawlowski K., Lowther S. E., Connell J. W., Siochi E. J., Harrison J. S., St. Clair T. L.: Polymer single-walled carbon nanotube composites for potential aircraft applications. NASA ICASE report No. 2002-36, NASA/CR-2002-211940 (2002).

[3] Abraham J. K., Philip B., Witchurch A., Varadan V. K., Redy C.C.: A compact wireless gas sensor using a carbon nanotube/PMMA thin film chemiresistor. Smart Materials and Structures, **13**, 1045–1049 (2004). DOI: 10.1088/0964-1726/13/5/010

[4] Curran S. A., Talla J., Dias S., Zhang D., Carroll D., Birx D.: Electrical transport measurements of highly conductive carbon nanotube/poly(bisphenol A carbonate) composite. Journal of Applied Physics, **105**, 073711/1–073711/5 (2009).
DOI: 10.1063/1.3073938

[5] Singh I., Bhatnagar P. K., Mathur P. C., Kaur I., Bharadwaj L. M., Pandey R.: Optical and electrical characterization of conducting polymer-single walled carbon nanotube composite films. Carbon, **46**, 1141–1144 (2008).
DOI: 10.1016/j.carbon.2008.04.013

[6] Wang T., Lei C-H., Dalton A. B., Creton C., Lin Y., Fernando K. A. S., Sun Y-P., Manea M., Asua J. M., Keddie J. L.: Waterborne, nanocomposite pressure-sensitive adhesives with high tack energy, optical transparency, and electrical conductivity. Advanced Materials, **18**, 2730–2734 (2006).
DOI: 10.1002/adma.200601335

[7] Grossiord N., Kivit P. J. J., Loos J., Meuldijk J., Kyrylyuk A. A., van der Schoot P., Koning C. E.: On the influence of the processing conditions on the performance of electrically conductive carbon nanotube/polymer nanocomposites. Polymer, **49**, 2866–2872 (2008).
DOI: 10.1016/j.polymer.2008.04.033

[8] Peng H., Sun X.: Highly aligned carbon nanotube/polymer composites with much improved electrical conductivities. Chemical Physics Letters, **471**, 103–105 (2009).
DOI: 10.1016/j.cplett.2009.02.008

[9] Ma P. C., Tang B. Z., Kim J-K.: Effect of CNT decoration with silver nanoparticles on electrical conductivity of CNT-polymer composites. Carbon, **46**, 1497–1505 (2008).
DOI: 10.1016/j.carbon.2008.06.048

[10] Bauhofer W., Kovacs J. S.: A review and analysis of electrical percolation in carbon nanotube polymer composites. Composites Science and Technology, **69**, 1486–1498 (2009).
DOI: 10.1016/j.compscitech.2008.06.018

[11] Li J., Ma P. C., Chow W. S., To C. K., Tang B. Z., Kim J-K.: Correlations between percolation threshold, dispersion state, and aspect ratio of carbon nanotubes. Advanced Functional Materials, **17**, 3207–3215 (2007).
DOI: 10.1002/adfm.200700065

[12] Xie X-L., Mai Y-W., Zhou X-P.: Dispersion and alignment of carbon nanotubes in polymer matrix: A review. Materials Science and Engineering R: Reports, **49**, 89–112 (2005).
DOI: 10.1016/j.mser.2005.04.002

[13] Song Y. S., Youn J. R.: Influence of dispersion states of carbon nanotubes on physical properties of epoxy nanocomposites. Carbon, **43**, 1378–1385 (2005).
DOI: 10.1016/j.carbon.2005.01.007

[14] Martin C. A., Sandler J. K. W., Shaffer M. S. P., Schwarz M-K., Bauhofer W., Schulte K., Windle A. H.: Formation of percolating networks in multi-wall carbon-nanotube-epoxy composites. Composites Science and Technology, **64**, 2309–2316 (2004).
DOI: 10.1016/j.compscitech.2004.01.025

[15] Seidel G. D., Boehringer K. L., Lagoudas D. C.: Analysis of clustering and interphase region effects on the electrical conductivity of carbon nanotube-polymer nanocompistes via computational micromechanics. in 'Proceedings of SMASIS 2008 Ellicott City, USA' p.7 (2008).

[16] Fu M., Yu Y., Xie J. J., Wang L. P., Fan M. Y., Liang S. L., Zeng Y. K.: Significant influence of film thickness on the percolation threshold of multiwall carbon nanotube/low density polyethylene composite films. Applied Physics Letters, **94**, 012904/1–012904/3 (2009).
DOI: 10.1063/1.3056055

[17] Avilés F., Cauich-Rodríguez J. V., Moo-Tah L., May-Pa A., Vargas-Coronado R.: Evaluation of mild acid oxidation treatments for MWCNT functional. Carbon, **47**, 2970–2975 (2009).
DOI: 10.1016/j.carbon.2009.06.044

[18] Liao Y-H., Marietta-Tondin O., Liang Z., Zhang C., Wang B.: Investigation of the dispersion process of SWNTs/SC-15 epoxy resin nanocomposites. Materials Science and Engineering A, **385**, 175–181 (2004).
DOI: 10.1016/S0921-5093(04)00857-3

[19] Hernández J. J., García-Gutiérrez M. C., Nogales A., Rueda D. R., Kwiatkowsa M., Szymczyk A., Roslaniecb Z., Conchesoc A., Guineac I., Ezquerra T. A.: Influence of preparation procedure on the conductivity and transparency of SWCNT-polymer nanocomposites. Composites Science and Technology, **69**, 1867–1872 (2009).
DOI: 10.1016/j.compscitech.2009.04.002

[20] Chang L., Friedrich K., Ye L., Toro P.: Evaluation and visualization of the percolating networks in multi-wall carbon nanotube/epoxy composites. Journal of Materials Science, **44**, 4003–4012 (2009).
DOI: 10.1007/s10853-009-3551-3

[21] Sandler J. K. W., Kirk J. E., Kinloch I. A., Shaffer M. S. P., Windle A. H.: Ultra-low electrical percolation threshold in carbon-nanotube epoxy composites. Polymer, **44**, 5893–5899 (2003).
DOI: 10.1016/S0032-3861(03)00539-1

[22] Kovacs J. Z., Velagala B. S., Schulte K., Bauhofer W.: Two percolation thresholds in carbon nanotube epoxy composites. Composites Science and Technology, **67**, 922–928 (2007).
DOI: 10.1016/j.compscitech.2006.02.037

[23] Antonucci F., Faiella G., Giordano M., Nicolais L., Pepe G.: Electrical properties of single walled carbon nanotube reinforced polystyrene composites. Macromolecular Symposia, **247**, 172–181 (2007).
DOI: 10.1002/masy.200750120

[24] Ha M. L. P., Grady B. P., Lolli G., Resasco D. E., Ford T. W.: Composites of single-walled carbon nanotubes and styrene-isoprene copolymer latices. Macromolecular Chemistry and Physics, **205**, 446–456 (2007). DOI: 10.1002/macp.200600521

[25] Kymakis E., Alexandou I., Amaratunga G. A. J.: Single-walled carbon nanotube-polymer composites: Electrical, optical and structural investigation. Synthetic Metals, **127**, 59–62 (2002). DOI: 10.1016/S0379-6779(01)00592-6

[26] Du F., Guthy C., Kashiwagi T., Fischer J. E., Winey K. I.: An infiltration method for preparing single-wall nanotube/epoxy composites with improved thermal conductivity. Journal of Polymer Science B: Polymer Physics, **44**, 1513–1519 (2006). DOI: 10.1002/polb.20801

[27] Seidel G. D., Lagoudas D. C.: A micromechanics model for the electrical conductivity of nanotube-polymer nanocomposites. Journal of Composite Materials, **43**, 917–941 (2009). DOI: 10.1177/0021998308105124

[28] Xiao G., Tao Y., Lu J., Zhang Z.: Highly conductive and transparent carbon nanotube composite thin films deposited on polyethylene terephthalate solution dipping. Thin Solid Films, **518**, 2822–2824 (2010). DOI: 10.1016/j.tsf.2009.11.021

[29] Blackburn J. L., Barnes T. M., Beard M. C., Kim Y-H., Tenent R. C., McDonald T. J., To B., Coutts T. J., Heben M. J.: Transparent conductive single-walled carbon nanotube networks with precisely tunable ratios of semiconducting and metallic nanotubes. ACS Nano, **2**, 1266–1274 (2008). DOI: 10.1021/nn800200d

eXPRESS Polymer Letters Vol.4, No.5 (2010) 300–310
Available online at www.expresspolymlett.com
DOI: 10.3144/expresspolymlett.2010.38

Influence of silver ion reduction on electrical modulus parameters of solid polymer electrolyte based on chitosan-silver triflate electrolyte membrane

*S. B. Aziz**, *Z. H. Z. Abidin, A. K. Arof*

Center for Ionics, University Malaya, Physics Department, Faculty of Science, 50603 Kuala Lumpur, Malaysia

Received 9 January 2010; accepted in revised form 11 March 2010

Abstract. The electric modulus properties of solid polymer electrolyte based on chitosan: $AgCF_3SO_3$ from 303 to 393 K have been investigated by using impedance spectroscopy. The shift of the M'' peak spectra with frequeny depends on the dissociation and association of ions. The lowest conductivity relaxation time τ_σ, was found for the sample with the highest conductivity. The real part of electrical modulus shows that the material is highly capacitive. The asymmetric peak of the imaginary part of electric modulus M'', predicts a non Debye type relaxation. The distribution of relaxation times was indicated by a deformed arc form of Argand plot. The increase of M' and M'' values above 358 K can be attributed to the transformation of silver ions to silver nanoparticles. The complex impedance plots and ultraviolet-visible (UV-vis) absorption spectroscopy indicate the temperature dependent of silver nanoparticles in chitosan-silver triflate solid electrolyte. The formation of silver nanoparticles was confirmed by transmission electron microscopy (TEM). The scaling behavior of M'' spectra shows that the dynamical relaxation processes is temperature independent for aparticular composition. The β exponent value indicate that the conductivity relaxation is highly non exponential.

Keywords: *polymer membranes, electrical modulus, impedance analysis, UV-vis analysis, transmission electron microscopy*

1. Introduction

Polymer electrolytes represent a fascinating class of solid-state coordination compounds, which support ionic conductivity in flexible, yet solid membranes [1]. It has been reported that [2] chain polymers, carrying an electro-negative atom (oxygen or nitrogen) in their repeat unit, can act as solvents for certain salts as a consequence of the attractive interaction between chains and cations. Previous studies have proven the existence of both atoms in chitosan polymer [3]. Polymer electrolytes have been studied for their application in batteries, fuel cells, sensors and electrochromic displays [4, 5]. Although these studies revealed many of the properties of these complex systems, the conductivity mechanism is still not fully understood [6]. Usually both crystalline and amorphous phases are present in polymer electrolytes but conductivity mainly occurs in the amorphous phase [7]. The coupling between the polymer segmental relaxation and the ion transport in polymer electrolytes is fascinating; although it is not completely understood, it still holds the key to the development of new energy sources [8].

It has been reported, that the frequency dependent conductivity and relaxation dynamic are both sensitive to the motion of charge species and dipoles of the polymer electrolytes [9]. For close inspection of the relaxation dynamics, the dielectric relaxation can be studied in electric modulus formalism M'' [10]. This modulus representation has been motivated by M'' displaying a pronounced peak and

*Corresponding author, e-mail: shujaadeen78@yahoo.com

thereby associating a time scale τ with the extent of conductivity. On the other hand the modulus representation is still a matter of debate [11], although the relations among the different quantities are well defined. From the physical point of view, the electrical modulus corresponds to the relaxation of the electric field in the material when the electric displacement remains constant [12]. The usefulness of modulus representation is to suppress the signal intensity associated with electrode polarization or to emphasize small features at high frequencies [11]. Thus, the electric modulus spectra provide an opportunity to investigate conductivity and its associated relaxation in ionic conductors and polymers [13].

In this work chitosan has been used as the base polymer for preparation chitosan-silver triflate polymer electrolyte thin films. A monomer of chitosan consists of hydroxyl and amine functional groups which have lone pair electrons that are suitable for the preparation of solid polymer electrolytes [14]. The silver-based polymer electrolytes are prepared by dissolving silver salts such as $AgBF_4$, $AgClO_4$, $AgCF_3SO_3$ and $AgSbF_6$ into polymer hosts such as poly(2-ethyl-2-oxazoline) (POZ), poly(ethylene oxide) (PEO) and poly(vinyl pyrrolidone) (PVP) due to coordination interaction between polar groups and silver ions [15, 16]. The oxygen and nitrogen atoms of polar polymers play an essential role in facilitated olefin transport. However, they also reduce silver ions and create silver metal nanoparticles [17]. This is because silver ions are easily reduced by the lone pair electrons of the nitrogen and oxygen atoms [18]. Each of the nitrogen and oxygen atoms of the functional groups in chitosan has lone pair electrons for occurring complexation as well as reduction of silver ions.

Due to the above reasons the main aim of the present work is to study the influence of silver ion reduction to silver nanoparticle on the electrical modulus properties of chitosan-silver triflate solid electrolyte over a wide range of frequency and temperature.

2. Experimental

2.1. Preparation of SPE thin films

Chitosan from crab shells (≥75% deacetylated, Sigma Aldrich, USA, CAS No. 9012-76-4) and silver triflate ($AgCF_3SO_3$) with a molecular weight 256.94 (supplied by Fluka, ≥99 purity, Germany, CAS No. 2923-28-6) have been used as the raw materials in this study. The solid polymer electrolyte (SPE) films were prepared by the solution cast technique with acetic acid (1%) as solvent. In the present system 1 g of chitosan was fixed and dissolved in acetic acid solution. To this system silver triflate ($AgCF_3SO_3$) was added and varied from 2 to 10 wt% in steps of 2 wt% to prepare various composition of chitosan-silver triflate electrolyte in weight percent ratios; 100:0 for pure chitosan acetate, 98:2, 96:4, 94:6, 92:8 and 90:10 for chitosan:$AgCF_3SO_3$. The mixture were stirred continuously until homogeneous solution were obtained. After casting in different Petri dishes, the solutions were left to dry at room temperature for films to form. The films were transferred into a dessicator for continuous drying. This procedure yields mechanically stable and solvent-free films.

2.2. Complex Impedance measurement

The complex impedance spectroscopy is used to characterize the electrical properties of the materials. The SPE films were cut into small discs of 2 cm diameter and sandwiched between two identical circular smooth and cleaned stainless steel electrodes under spring pressure to ensure good electrical contacts between the electrodes and the sample; this enables us to avoid the parasite capacitance induced by the presence of air interstices at the interfaces between the sample and the electrodes. The impedance of the films was measured using the HIOKI 3531 Z Hi-tester (made in Japan, No. 1036555) that was interfaced to a computer in the frequency range from 50 Hz to 1000 kHz. The software controls the measurements and calculates the real and imaginary parts of impedance too. The real (Z') and imaginary (Z'') part of complex impedance (Z^*) were used for the evaluation of the real (M') and imaginary (M'') parts of complex electric modulus (M^*) using the Equations (1) and (2) [19]:

$$Z^* = Z' - jZ'' \tag{1}$$

$$M^* = j\omega C_0 Z^* = M' + jM'' \tag{2}$$

From Equation (1) and Equation (2) one can get the following Equations (3) and (4):

$$M' = \omega C_0 Z'' \quad (3)$$

$$M'' = \omega C_0 Z' \quad (4)$$

Here C_0 is the vacuum capacitance and given by $\varepsilon_0 A/t$, where t is the thickness and A is the area of the film. ω is the angular frequency and equal to $\omega = 2\pi f$, f is the frequency of the applied field.

2.3. UV-vis and TEM characterization

The UV-vis spectra of the chitosan-silver triflate electrolyte film have been recorded using a Jasco V-570 UV-Vis-NIR spectrophotometer (Japan, Jasco SLM-468) in the absorbance mode. Transmission electron microscopy (TEM) images of the electrolyte were recorded using a LEO LIBRA (Germany, 120 EFTEM, accelerating voltage 120 kV) instrument. A drop of the solution of chitosan-silver triflate electrolyte was placed on a carbon coated copper grid and dried at room temperature after removal of excess solution using a filter paper.

3. Results and discussions

3.1. Concentration dependence of M″ spectra

Figure 1 shows the frequency dependence of M'' spectra for different salt concentrations at a fixed temperature. It is clear that the maximum M'' peak spectra for the highest conducting sample shifts to higher frequency compared to other compositions. The appearance of more than one peaks for pure chitosan and chitosan-silver triflate (98:2) especially at low frequency may be due to polar group relaxations. However, these peaks disappear for the samples with higher salt concentration which

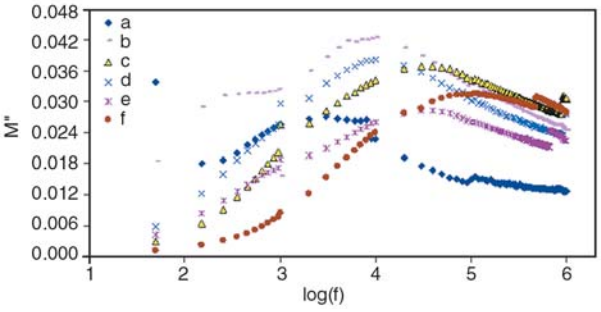

Figure 1. Concentration dependence of M'' for (a) pure chitosan acetate (100:0), (b) 98:2, (c) 96:4, (d) 94:6, (e) 92:8 and (f) 90:10 for chitosan:$AgCF_3SO_3$ at 303 K

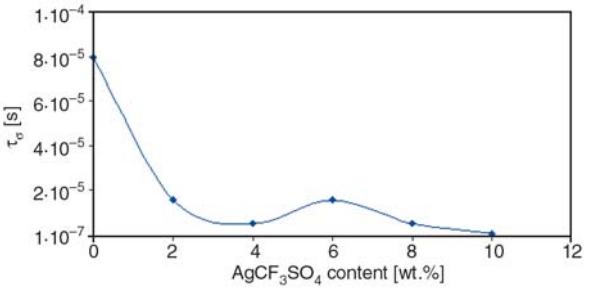

Figure 2. Concentration dependence of conductivity relaxation time (τ_σ) at 303 K

can be ascribed to the large amount of free charge carrier concentration and their motions within the material. Consequently a high DC conductivity is produced which can mask the low frequency relaxation.

These peaks represent the conductivity relaxation peak for the distribution of relaxation times of the free charges and the broadening of the peaks suggests a non-Debye type of relaxation in the material [20]. The peak shifts to higher frequency as the conductivity increases indicating that the relaxation time decreases as conductivity increases [21]. The conductivity relaxation times can be calculated from the relation, $2\pi f_{max} = 1/\tau_\sigma$, were τ_σ is the conductivity relaxation time and f_{max} is a frequency corresponding to M''_{max}. The variation of τ_σ, as a function of siver triflate concentration is shown in Figure 2. It can be seen that the conductivity relaxation times decrease with increasing salt concentration up to 4 wt% $AgCF_3SO_3$. From the results it can be inferred that there is competition between ion dissociation and association especially from four to eight weight percentage of salt. The steep decrease in conductivity relaxation time from 8 wt% $AgCF_3SO_3$ to 10 wt% $AgCF_3SO_3$ can be explained by an increase in charge carriers concentration, i.e., an increase of conductivity within the sample as a result of increase of a number of mobile charge carriers.

3.2. Frequency dependence of M′ and M″ at selected temperatures

Figures 3 and 4 show the frequency dependence of real and imaginary parts of complex modulus at several temperatures for the sample with the highest conductivity (90:10). The real and imaginary part of complex modulus were calculated by using Equations (3) and (4). The conductivity behavior in

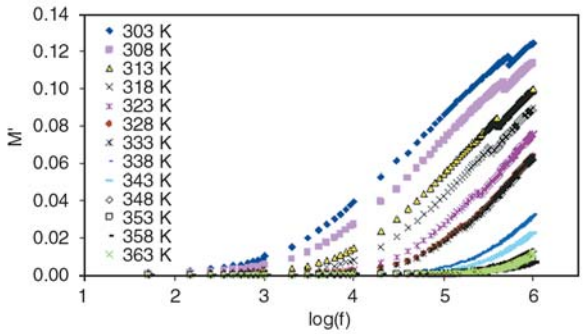

Figure 3. Frequency dependence of M' at different temperature for chitosan-silver triflat (90:10)

the frequency domain is more conveniently interpreted in terms of conductivity relaxation time, τ_σ, using electrical modulus (M^*) representation. The M^* representation is now widely used to analyze ionic conductivities by associating a conductivity relaxation time with the ionic process [22]. From Figure 3, it is obvious that at lower frequencies M' values are very small, tend to be zero indicating the removal of electrode polarization, [23, 24] while the increase of M' with increasing frequency and reaching a maximum value M_∞ at high frequency, may be due to the distribution of relaxation processes over a range of frequencies [25]. The observed dispersion is mainly due to conductivity relaxation spreading over a range of frequencies and indicates the presence of a relaxation time, which should be accompanied by a loss peak in the diagram of the imaginary part of electric modulus versus frequency. The absence of peak in M' diagram is due to the fact that M' in complex electric modulus (M^*) is equivalent to ε' in complex permittivity (ε^*) i.e., M' represents the ability of the material to store the energy. The reduction in the values of M', at increasing temperature results from the increase in the mobility of the polymer segment and charge carriers with the temperature. It is well known that the orientation of the charge carriers and molecular dipoles becomes easier at high temperatures.

The formation of loss peaks is clearly observed in Figure 4. It is obvious that at lower frequencies M'' exhibits low value, which might be due to the large value of capacitance associated with the electrode polarization effect [26]; as a result of accumulation of a large amount of charge carriers at the electrode/solid polymer electrolyte interface. However, at high frequencies well-defined peaks are observed. The broad and asymmetric of peaks on both sides of the maxima predicts the non-Debye behavior. The region on the left of the peak determines the range in which charge carriers are mobile over long distances, while region to the right is where carriers are confined to potential wells being mobile over short distance [24]. The disappearance of M'' peak spectra at higher temperatures is due to experimental frequency limitation.

It can be observed that both M' and M'' increase above 358 K, which can be attributed to the reduction of silver ions to silver nanoparticles at these higher temperatures. The reduction of silver ions to silver nanoparticles could be more manifested in the study of M' and M'' as a function of temperature at a fixed frequency.

The frequency associated with each peak is known as relaxation frequency and gives the most probable conductivity relaxation time τ_σ for ions. The reciprocal temperature variation of log (f_{max}) is shown in Figure 5. The figure satisfies the Arrhenius behavior with the activation energy, E_a = 1.16 eV.

The rise in temperature causes the drop in relaxation time due to the increased mobility of ionic carriers. The regression value R^2 is 0.996 indicating that all points lie on almost straight line.

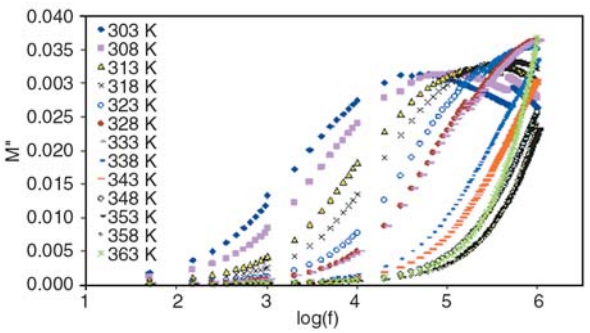

Figure 4. Frequency dependence of M'' at different temperature for chitosan-silver triflate (90:10)

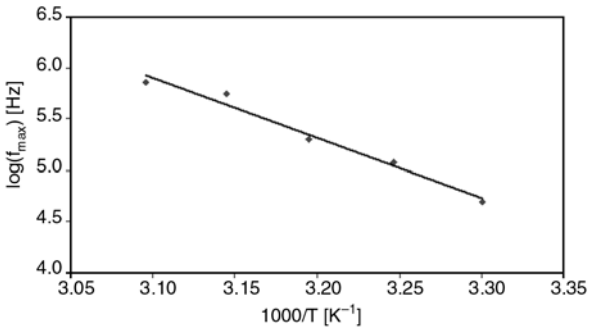

Figure 5. Temperature dependence of relaxation frequency

3.3. Argand plots analysis

The study of Argand plot at different temperatures can be use to demonstrate the nature of relaxation processes in the present polymer electrolyte. Figure 6 shows the temperature dependence of Argand plots.

It is obvious from Figure 6, that the curves of Argand plot are incomplete half semicircle which can not be explained by Debye model (i.e., single relaxation time). In this case a distribution of relaxation time is necessary to interpret the experimental data especially in polymers. Many reasons exist for the relaxation times to be distributed in solids, such as ellipsoidal shape of polar groups, hopping, space charge polarization and the most obvious being the presence of inhomogeneties [27]. Our Argand plots appeared as deformed arcs at low temperatures with their centers positioned below the horizontal axis. This position, in principle, corresponds to the electric relaxation in materials with both the relaxation time and activation energy distributed and intercorrelated [28]. It can be seen (Figure 6) that with increasing temperature the Argand curves shifts towards the origin. This is can be ascribed to the increase of conductivity resulting of increasing of ionic mobility with temperature and thus decreasing of both Z' and Z''. The increase of M''–M' curve at 363 K can be attributed to the increase of resistance within the sample due to the reduction of large amount of silver ions to silver nanoparticles.

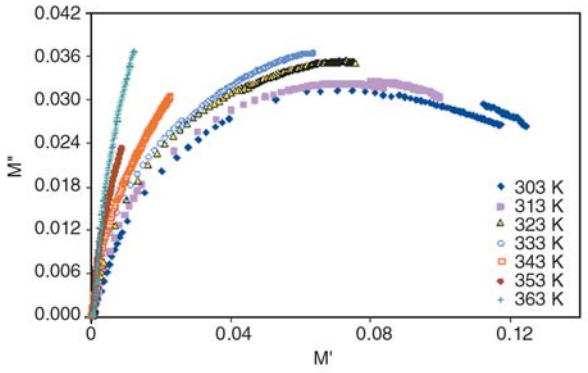

Figure 6. Argand plots for chitosan-silver triflate (90:10) at different temperatures

3.4. Temperature dependence of M′ and M″ at selected frequencies

Figure 7a and 7b shows the temperature dependence of M' and M'' at selected frequencies. It is clear from the figure that both M' and M'' decrease with increasing of temperature until 358 K, due to the increase of ionic conductivity, i.e., silver ions are dominant. However the increase of M' and M'' can be observed with increasing temperature above 358 K, which can be attributed to the transformation of a large amount of silver ions to silver nanoparticles within the sample. These silver nanoparticles are able to increase the resistance within sample and consequently hinders the ionic motions.

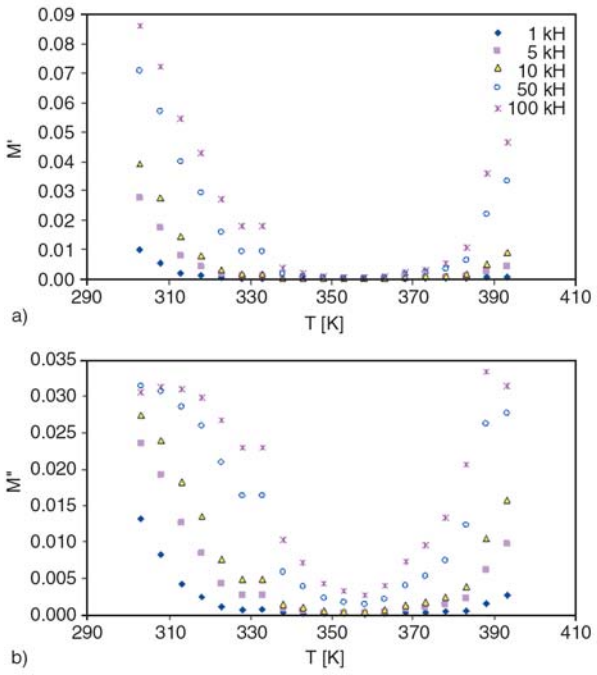

Figure 7. Temperature dependence of (a) M' and (b) M'' at selected frequencies for chitosan-silver triflate (90:10)

The complex impedance plots can be used as a method to detect the presence of silver nano-particles and their temperature dependence within the present sample. This is due to the powerful ability of electrochemical impedance spectroscopy for the investigation of molecular mobility, phase transitions, conductivity mechanisms and interfacial effects in polymers and complex systems [29].

The complex impedance plots at different temperatures which are shown in Figure 8, are strongly support the above explanation for the increase of M' and M''. The complex impedance plots (Z'' *vs.* Z') are commonly used to separate the bulk material (depressed semicircle) and the electrode surface polarization phenomena (tilted spike) [30]. The electrode polarization phenomena (tilted spike)

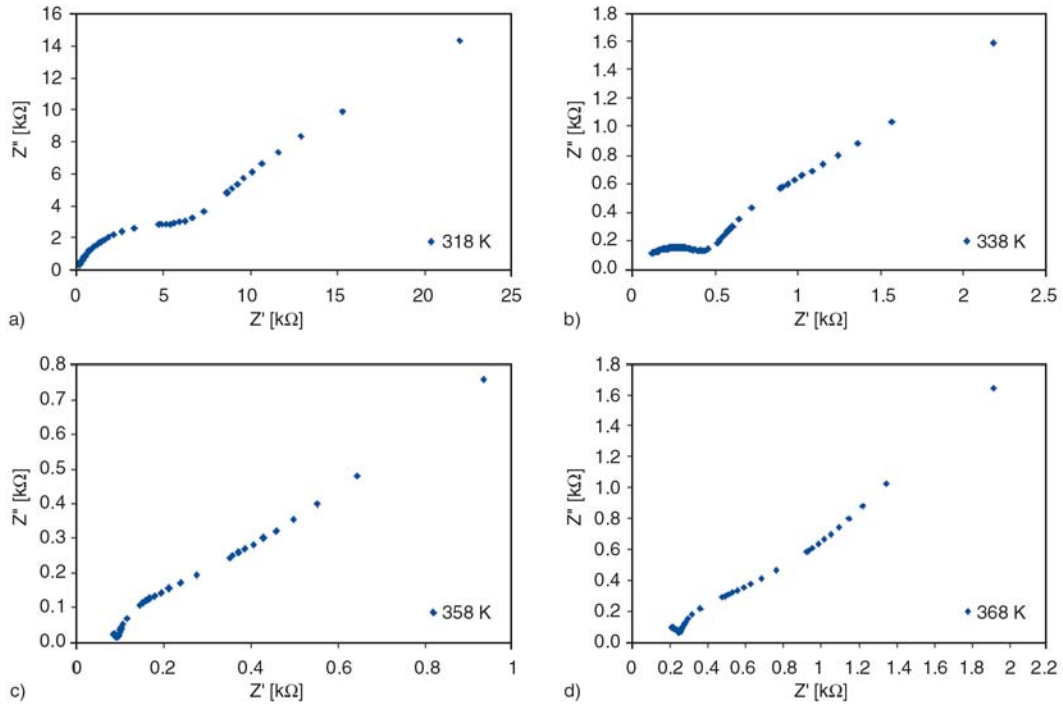

Figure 8. Complex impedance plots of chitosan-$AgCF_3SO_3$ (90:10) at selected temperatures

occurs due to formation of electric double layer (EDL) capacitances by the free charges build up at the interface between the electrolyte and the electrode surfaces in plane geometry [30, 22]. The appearance of second semicircle at different temperatures can be attributed to silver nanoparticles that acts as grain boundaries in the present system (Figure 8). Thus, there is a competition between silver ions and silver nanoparticles within the same system. It can be noticed that, the bulk resistance decrease with rise in temperature from 303 to 358 K, which indicate the dominance of silver ions, i.e., the system is almost ionic conductor. The increase of bulk resistance after 358 K demonstrates that with increasing temperature more silver ions converted to silver metal nanoparticles. Thus, transformation from silver ions (Ag^+) to silver nanoparticles (Ag^0) reduce the number of silver ions that contribute to polarization as well as conduction mechanisms and consequently increase both the M' and M''. This behaviour can be easily deduced from Equation (3) and Equation (4), because above 358 K, both the Z' and Z'' values increases. Consequently both M' and M'' increased. In this case the polymer electrolyte almost exhibits nanocomposite behavior rather than ionic behaviour. However for pure chitosan the second semicircle can not be observed as depicted in Figure 9. The transformation of silver ion to silver nanoparticle can be understood more obviously when we studying the UV-vis absorption spectra of pure chitosan and chitosan-silver triflate (90:10) solid electrolyte.

Figure 9 shows the complex impedance plots of pure chitosan at different temperatures. It is interesting to note that the bulk resistance of pure chitosan is higher than the bulk resistance of chitosan-silver triflate (90:10) solid electrolyte. In addition the bulk resistance of pure chitosan decrease continiously with increase in temperature untill 393 K, which is completely different as compared to Z''–Z' plot of chitosan-silver triflate (90:10) solid electrolyte. It is interesting to note that the Z''–Z' plot of pure chitosan dosen't exhibit any second semicircle at different temperature as manifested in chitosan-silver triflate solid electrolyte.

To investigate the formation of Ag nanoparticles and their temperature dependence in chitosan-silver triflate system, UV-vis spectroscopy was used as a common characterizing method. This is due to the fact that silver nanoparticles and their clusters exhibit a characteristic UV-vis absorption band in the ultraviolet-visible (UV-vis) region [31]. Figure 10 shows the UV-vis absorption spectra of pure chitosan and chitosan-silver triflate (90:10) solid

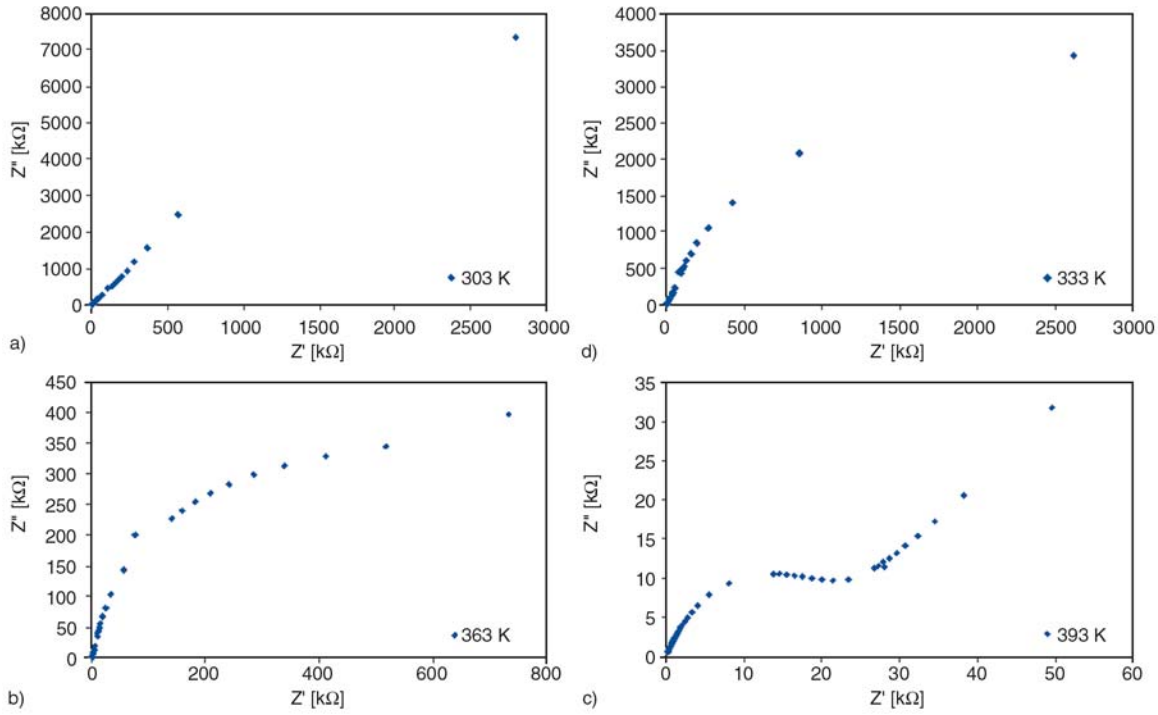

Figure 9. Complex impedance plots of pure chitosan at selected temperatures

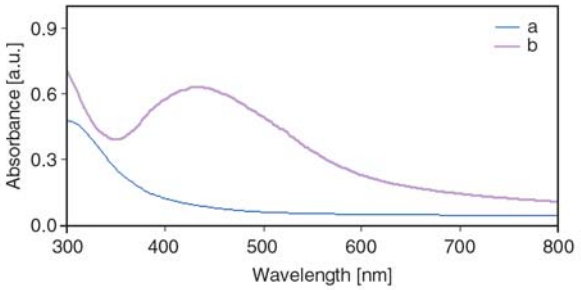

Figure 10. UV-vis absorption spectra of (a) pure chitosan and (b) chitosan-$AgCF_3SO_3$ (90:10) at room temperature (303 K)

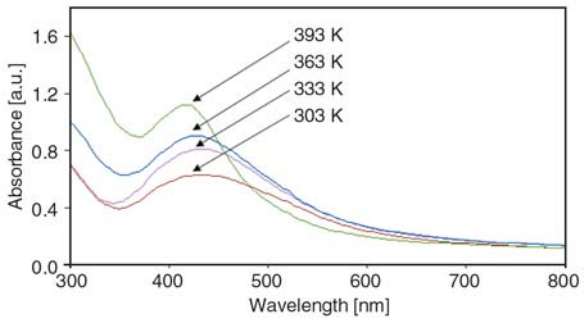

Figure 11. UV-vis spectra of chitosan-$AgCF_3SO_3$ (90:10) solid electrolyte at different temperatures

electrolyte at ambient temperature (303 K). It can be seen from the figure that pure chitosan has no absorption peak in the region 400 to 500 nm, while a broad absorption peak with a maximum at 426 nm was observed for chitosan-silver triflate (90:10) solid electrolyte which can be attributed to the surface plasmon band of silver nanoparticles. It is generally accepted that the absorption peak whose maximum occurs at around 420 to 520 nm is related to the formation of silver metal nanoparticles and its height gives information on the concentration of silver metal nanoparticles [32, 33].

Figure 11 shows the UV-vis absorption spectra for chitosan:$AgCF_3SO_3$ (90:10) solid electrolyte at different temperatures. It can be seen that the height of the peaks increases from 0.61 at 303 K to 1.2 at 393 K with increasing temperature, implying an increasing amount of Ag nanoparticles because reduction of silver ions to silver nanoparticles occurs more rapidly at a high temperature [34]. It has been reported that polymers which contain hydroxyl, carboxyl, and imide groups are responsible for Ag^+ ion reduction [35, 36]. This is due to strong affinity of N and O atoms of polar groups for silver ion and metallic silver [36].

The formation of silver nanoparticles in the present system is also indicated by the change in the color of the solid membranes from yellow to dark brown, this phenomenon is also reported by Kang *et al.* [37] for PVP-silver salt electrolyte. The origin of the intense colour of chitosan-silver triflate is attributed to the surface plasmon resonance (SPR), collective oscillation of free conduction electrons induced by an interacting electromagnetic field

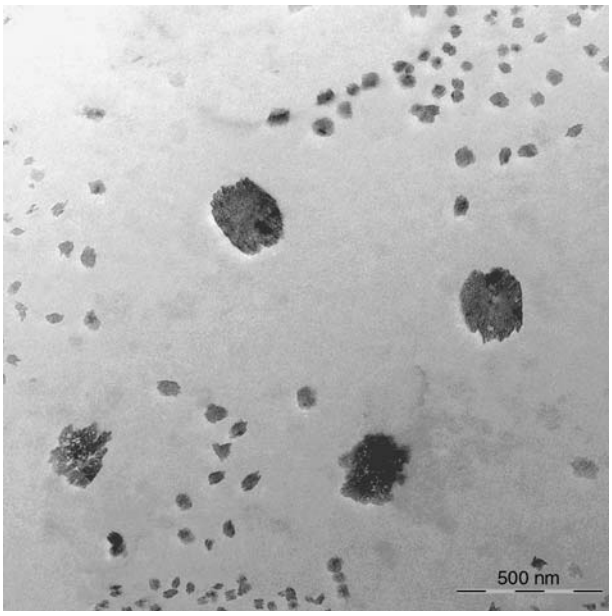

Figure 12. TEM micrograph of silver nanoparticles for chitosan-$AgCF_3SO_3$ (90:10) at room temperature

[38]. The colour of metal nanoparticles depends on the shape and size of the nanoparticles and dielectric constant of the surrounding medium. However, only electrons with free electron posses plasmon resonance in the visible spectrum, which give rise to such intense color [39].

Transmission electron microscopy (TEM) was used for visual observation of silver nanoparticles in the present system. Figure 12 shows the TEM image of the silver nanoparticles within chtosan-silver triflate (90:10) solid electrolyte. The TEM image indicates that the silver nanoparticles are dispersed and agglomerated. Generally particle agglomeration occurs as a result of larger attraction energy than repulsion energy between the particles [40].

Thus, the increase of M' and M'' at higher temperatures are strongly supported by impedance and UV-vis analysis. To our knowledge, this is the first report which discuss the effect of reduction of silver ions to silver nanoparticles on electrical modulus properties of solid polymer electrolyte (SPE).

3.5. Scaling behavior of M″

Scaling of the electric modulus can give further information about the dependence of the relaxation dynamics on the temperature, structure, and also on the concentration of the charge carriers [41]. We have scaled the imaginary part of electric modulus at different temperatures for chitosan:$AgCF_3SO_3$ (90:10) as shown in Figure 13. The M''_{max} and f_{max} are used as the scaling parameters for M'' and f respectively.

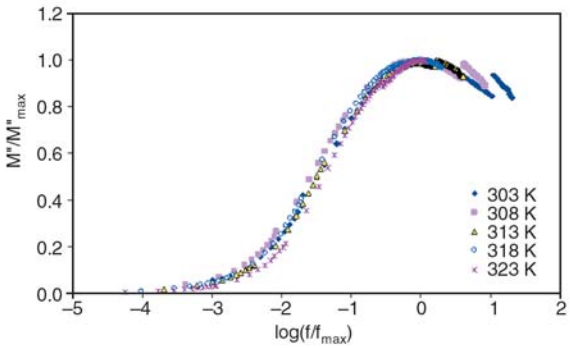

Figure 13. Scaling of M'' for chitosan-$AgCF_3SO_3$ (90:10) at different temperatures

It can be seen (Figure 13) that all modulus spectra merge on a single master curve. This indicates that the dynamical relaxation processes occurring at different temperatures are independent of temperature for a particular composition [42]. The asymmetric shape of the plot is a strong evidence that the dielectric relaxation process deviates from the pure Debye behaviour, and a non-symmetric distribution of relaxation times exists [43]. It is obvious from Figure 13, that the normalized modulus plot is non symmetric, in agreement with the non exponential behavior of the electrical function, which is well described by the Kohlrausch-William-Watts exponential function [44], see Equation (5):

$$\phi = \exp\left[\left(-\frac{t}{\tau}\right)^{\beta}\right] \quad 0 < \beta < 1 \tag{5}$$

were β is an exponent indicating departure from the Debye relaxation. In the present system, the value of full width half height (*FWHH*) for chitosan:$AgCF_3SO_3$ (90:10) is about 2 decades, which is greater than 1.14 decades for the ideal Debye behavior. The value of β is calculated by Equation (6):

$$\beta = \frac{1.14}{FWHH} \tag{6}$$

The small value of β (0.57) for the present system indicates that the conductivity relaxation is highly non-exponential [42]. The smaller the value of β larger is the deviation of relaxation with respect to Debye type relaxation (β = 1). The value of β for a practical solid electrolyte is clearly less than 1 [20].

4. Conclusions

Chitosan-silver triflate electrolytes were prepared by solution casting technique. The M'' spectra shift to higher frequency for the sample with the highest conductivity due to the increase of mobile charge carriers. The long tail of M' in the low frequency range indicates the capacitive nature of the system. The broadness of M'' spectra peaks showing the non Debye type relaxation. The deformed arc shape of Argand plots is due to the distribution of relaxation times. The increase of M' and M'' at elevated temperatures can be ascribed to the reduction of a large amount of silver ions to silver nanoparticles. The appearance of second semicircles in complex impedance plots and their temperature dependence confirms the silver nanoparticles and their growth. The UV/vis spectra show that the number of silver nanoparticles increases with increasing temperature which can be ascribed to the strong interaction of hydroxyl and amine groups of chitosan to silver ions. The formation of silver nanoparticles was confirmed by transmission electron microscopy (TEM). The scaling behavior of spectra shows that the dynamical relaxation processes is temperature independent for aparticular composition. The β exponent value indicate that the conductivity relaxation is highly non exponential.

Acknowledgements

The authors gratefully acknowledge the financial support from University of Malaya in the form of grant (grant No. PS214/2009A) for this research project. Shujahadeen B. Aziz wishes to thank the Kurdistan Regional Government for the scholarship awarded. The authors like to thank Fahmi Fariq for the UV-Vis measurements.

References

[1] Karan N. K., Pradhan D. K., Thomas R., Natesan B., Katiyar R. S.: Solid polymer electrolytes based on polyethylene oxide and lithium trifluoro- methane sulfonate (PEO-$LiCF_3SO_3$): Ionic conductivity and dielectric relaxation. Solid State Ionics, **179**, 689–696 (2008).
DOI: 10.1016/j.ssi.2008.04.034

[2] Dieterich W., Dürr O., Pendzig P., Bunde A., Nitzan A.: Percolation concepts in solid state ionics. Physica A: Statistical and Theoretical Physics, **266**, 229–237 (1999).
DOI: 10.1016/S0378-4371(98)00597-4

[3] Yahya M. Z. A., Arof A. K.: Studies on lithium acetate doped chitosan conducting polymer system. European Polymer Journal, **38**, 1191–1197 (2002).
DOI: 10.1016/S0014-3057(01)00290-7

[4] Bhargav P. B., Mohan V. M., Sharma A. K., Rao V. V. R. N.: Investigations on electrical properties of (PVA:NaF) polymer electrolytes for electrochemical cell applications. Current Applied Physics, **9**, 165–171 (2009).
DOI: 10.1016/j.cap.2008.01.006

[5] Baskaran R., Selvasekarapandian S., Kuata N., Kawamura J., Hattori T.: Ac impedance, DSC and FT-IR investigations on (x)PVAc-(1–x)PVdF blends with $LiClO_4$. Materials Chemistry and Physics, **98**, 55–61 (2006).
DOI: 10.1016/j.matchemphys.2005.08.063

[6] de Jonge J. J., Van Zon A., de Leeuw S. W.: Molecular dynamics study of the influence of the polarizability in PEO_x-NaI polymer electrolyte systems. Solid State Ionics, **147**, 349–359 (2002).
DOI: 10.1016/S0167-2738(02)00056-5

[7] Avellaned C. O. A., Vieira D. F., Al-Kahlout A., Leite E. R., Pawlicka A., Aegerter M. A.: Solid-state electrochromic devices with Nb_2O_5:Mo thin film and gelatin-based electrolyte. Electrochemica Acta, **53**, 1648–1654 (2007).
DOI: 10.1016/j.electacta.2007.05.065

[8] Natesan B., Karan N. K., Katiyar R. S.: Ion relaxation dynamics and nearly constant loss behavior in polymer electrolyte. Physical Review E, **48**, 042801/1–042801/4 (2006).
DOI: 10.1103/PhysRevE.74.042801

[9] Singh K. P., Gupta P. N.: Study of dielectric relaxation in polymer electrolytes. European Polymer Journal, **34**, 1023–1029 (1998).
DOI: 10.1016/S0014-3057(97)00207-3

[10] Chabchoub N., Khemakhem H.: Ac ionic conductivity investigations on the $CsK(SO_4)\cdot Te(OH)_6$ material. Journal of Alloys and Compounds, **370**, 8–17 (2004).
DOI: 10.1016/j.jallcom.2003.08.091

[11] Richert R.: The modulus of dielectric and conductive materials and its modification by high electric fields. Journal of Non-Crystalline Solids, **305**, 29–39 (2002).
DOI: 10.1016/S0022-3093(02)01085-2

[12] Molak A., Paluch M., Pawlus S., Klimontko J., Ujma Z., Gruszka I.: Electric modulus approach to the analysis of electric relaxation in highly conducting $(Na_{0.75}Bi_{0.25})(Mn_{0.25}Nb_{0.75})O_3$ ceramics. Journal of Applied Physics D: Applied Physics, **38**, 1450–1460 (2005).
DOI: 10.1088/0022-3727/38/9/019

[13] Migahed M. D., Ishra M., Fahmy T., Barakat A.: Electric modulus and AC conductivity studies in conducting PPy composite films at low temperature. Journal of Physics and Chemistry of Solids, **65**, 1121–1125 (2004).
DOI: 10.1016/j.jpcs.2003.11.039

[14] Majid S. R., Arof A. K.: Electrical behavior of proton-conducting chitosan-phosphoric acid-based electrolytes. Physica B: Condensed Matter, **390**, 209–215 (2007).
DOI: 10.1016/j.physb.2006.08.038

[15] Kim J. H., Min B. R., Wong J., Kang Y. S.: Anomalous temperature dependence of facilitated propylene transport in silver polymer electrolyte membranes. Journal of Membrane Science, **227**, 197–206 (2003).
DOI: 10.1016/j.memsci.2003.08.026

[16] Kang S. W., Kim J. H., Won J., Char K., Kang Y. S.: Effect of amino acids in polymer/silver salt complex membranes on facilitated olefin transport. Journal of Membrane Science, **248**, 201–206 (2004).
DOI: 10.1016/j.memsci.2004.08.028

[17] Kim J. H., Wong J., Kang Y. S.: Olefin-induced dissolution of silver salts physically dispersed in inert polymers and their application to olefin/paraffin separation. Journal of Membrane Science, **241**, 403–407 (2004).
DOI: 10.1016/j.memsci.2004.05.027

[18] Lim P. Y., Liu R. S., She P. L., Hung C. F., Shih H. C.: Synthesis of Ag nanospheres particles in ethylene glycol by electrochemical-assisted polyol process. Chemical Physics Letters, **420**, 304–308 (2006).
DOI: 10.1016/j.cplett.2005.12.075

[19] Padmasree K. P., Kanchan D. K.: Modulus studies of CdI_2–Ag_2O–V_2O_5–B_2O_3 system. Materials Science and Engineering B, **122**, 24–28 (2005).
DOI: 10.1016/j.mseb.2005.04.011

[20] Ram M., Chakrabarti S.: Dielectric and modulus studies on $LiFe_{1/2}Co_{1/2}VO_4$. Journal of Alloys and Compounds, **462**, 214–219 (2008).
DOI: 10.1016/j.jallcom.2007.08.001

[21] Yahya M. Z. A., Arof A. K.: Conductivity and X-ray photoelectron studies on lithium acetate doped chitosan films. Carbohydrate Polymer, **55**, 95–100 (2004).
DOI: 10.1016/j.carbpol.2003.08.018

[22] Pradhan D. K., Choudhary R. N. P., Samantaray B. K.: Studies of structural, thermal and electrical behavior of polymer nanocomposite electrolytes. Express Polymer Letters, **2**, 630–638 (2008).
DOI: 10.3144/expresspolymlett.2008.76

[23] Yakuphanoglu F.: Electrical conductivity and electrical modulus properties of α, ω-dihexylsexithiophene organic semiconductor. Physica B, **393**, 139–142 (2007).
DOI: 10.1016/j.physb.2006.12.075

[24] Dutta A., Sinha T. P., Jena P., Adak S.: Ac conductivity and dielectric relaxation in ionically conducting soda-lime-silicate glasses. Journal of Non-Crystalline Solids, **354**, 3952–3957 (2008).
DOI: 10.1016/j.jnoncrysol.2008.05.028

[25] Patro L. N., Hariharan K.: AC conductivity and scaling studies of polycrystalline SnF_2. Materials Chemistry and Physics, **116**, 81–87 (2009).
DOI: 10.1016/j.matchemphys.2009.02.056

[26] Patro L. N., Hariharan K.: Frequency dependent conduction characteristics of mechanochemically synthesized $NaSn_2F_5$. Material Science and Engineering: B, **162**, 173–178 (2009).
DOI: 10.1016/j.mseb.2009.04.003

[27] Kwan K. C.: Dielectric phenomena in solids. Elsevier, New York. (2004).

[28] Calleja R. D., Matveeva E. S., Parkhutik V. P.: Electric relaxation in chemically synthesized polyaniline: Study using electric modulus formalism. Journal of Non-Crystalline Solids, **180**, 260–265 (1995).
DOI: 10.1016/0022-3093(94)00470-6

[29] Psarras G. C., Gatos K. G., Karahaliou P. K., Georga S. N., Krontiras C. A., Karger-Kocsis J.: Relaxation phenomena in rubber/layered silicate nanocomposites. Express Polymer Letters, **1**, 837–845 (2007).
DOI: 10.3144/expresspolymlett.2007.116

[30] Sengwa R. J., Choudhary S., Sankhla S.: Low frequency dielectric relaxation processes and ionic conductivity of montmorillonite clay nanoparticles colloidal suspension in poly(vinyl pyrrolidone)-ethylene glycol blends. Express Polymer Letters, **2**, 800–809 (2008).
DOI: 10.3144/expresspolymlett.2008.93

[31] Lu J., Suarez J. J. B., Takahashi A., Haruta M., Oyama S. T.: In situ UV-vis studies of the effect of particle size on the epoxidation of ethylene and propylene on supported silver catalysts with molecular oxygen. Journal of Catalysis, **232**, 285–295 (2005).
DOI: 10.1016/j.jcat.2005.02.013

[32] Kim J. H., Kim C. K., Won J., Kang Y. S.: Role of anions for the reduction behavior of silver ions in polymer/silver salt complex membranes. Journal of Membrane Science, **250**, 207–214 (2005).
DOI: 10.1016/j.memsci.2004.10.032

[33] Liu Y., Chen S., Zhong L., Wu G.: Preparation of high-stable silver nanoparticle dispersion by using sodium alginate as a stabilizer under gamma radiation. Radiation Physics and Chemistry, **78**, 251–255 (2009).
DOI: 10.1016/j.radphyschem.2009.01.003

[34] Kim J. H., Min B. R., Kim H. S., Won J., Kang Y. S.: Facilitated transport of ethylene across polymer membranes containing silver salt: Effect of HBF_4 on the photoreduction of silver ions. Journal of Membrane Science, **212**, 283–288 (2003).
DOI: 10.1016/S0376-7388(02)00451-9

[35] Sharma V. K., Yngard R. A., Lin Y.: Silver nanoparticles: Green synthesis and their antimicrobial activities. Advances in Colloid and Interface Science, **145**, 83–96 (2009).
DOI: 10.1016/j.cis.2008.09.002

[36] Silvert P-Y., Herrera-Urbina R., Duvauchelle N., Vijayakrishnan V., Elhsissen K. T.: Preparation of colloidal silver dispersions by the polyol process. Part 1 – Synthesis and characterization. Journal of Materials Chemistry, **7**, 293–299 (1997).
DOI: 10.1039/JM9960600573

[37] Kang S. W., Kim J. H., Oh K., Won S. J., Char K., Kim H. S., Kang Y. S.: Highly stabilized silver polymer electrolytes and their application to facilitated olefin transport membranes. Journal of Membrane Science, **236**, 163–169 (2004).
DOI: 10.1016/j.memsci.2004.02.020

[38] Srivastava S., Haridas M., Basu J. K.: Optical properties of polymer nanocomposites. Bulletin Materials Science, **31**, 213–217 (2008).

[39] Zielińska A., Skwarek E., Zaleska A., Gazda M., Hupka J.: Preparation of silver nanoparticles with controlled particle size. Procedia Chemistry, **1**, 1560–1566 (2009).
DOI: 10.1016/j.proche.2009.11.004

[40] Lin H-W., Hwu W-H., Ger M-D.: The dispersion of silver nanoparticles with physical dispersal procedures. Journal of Materials Processing Technology, **206**, 56–61 (2008).
DOI: 10.1016/j.jmatprotec.2007.12.025

[41] Karmakar A., Majumdar S., Giri S.: Polaron relaxation and hopping conductivity in $LaMn_{1-x}Fe_xO_3$. Physical Review B, **79**, 094406/1–094406/7 (2009).
DOI: 10.1103/PhysRevB.79.094406

[42] Bhattacharya S., Gosh A.: Relaxation of silver ions in fast ion conducting molybdate glasses. Solid State Ionics, **176**, 1243–1247 (2005).
DOI: 10.1016/j.ssi.2005.03.002

[43] Psarras G. C., Manolakaki E., Tsangaris G. M.: Dielectric dispersion and ac conductivity in-Iron particles loaded-polymer composites. Composites Part A: Applied Science and Manufacturing, **34**, 1187–1198 (2003).
DOI: 10.1016/j.compositesa.2003.08.002

[44] Bhattacharya S., Gosh A.: Conductivity relaxation in some fast ion-conducting $AgI–Ag_2O–V_2O_5$ glasses. Solid State Ionics, **161**, 61–65 (2003).
DOI: 10.1016/S0167-2738(03)00277-7

eXPRESS Polymer Letters Vol.4, No.5 (2010) 311–320
Available online at www.expresspolymlett.com
DOI: 10.3144/expresspolymlett.2010.39

Starch-lignin foams

E. S. Stevens[1*], *A. Klamczynski*[2], *G. M. Glenn*[2]

[1]Department of Chemistry, State University of New York at Binghamton, Binghamton, NY 13902, USA
[2]Western Regional Research Center, Agricultural Research Service, United States Department of Agriculture, 800 Buchanan Street, Albany, CA 94710, USA

Received 29 January 2010; accepted in revised form 18 March 2010

Abstract. Although starch foams are well known as biodegradable alternatives to foamed polystyrene, starch-lignin foams have not previously been reported. Lignin is an abundant byproduct of paper manufacture usually burned as fuel for lack of higher-value uses. We have prepared novel starch-kraft lignin foams with a known technique similar to compression molding. Replacing 20% of the starch with lignin has no deleterious effect on density or morphology as indicated by scanning electron microscopy: a thin outer layer of approximately 100 μm encloses a region of cellular structure containing 100–200 μm voids, with the major internal region of the foam consisting of large voids of up to 1 mm in size. Powder X-ray diffraction shows residual structure in both starch and starch-lignin foams. Differential scanning calorimetry displays endothermic transitions in the starch foam but not in the starch-lignin foam, indicating that lignin stabilizes the residual starch structure. Lignin decreases water absorption; diffusion constants for the starch and starch-lignin foams are $2.68 \cdot 10^{-6}$ and $0.80 \cdot 10^{-6}$ cm^2/sec, respectively. The flexural strength of the starch-lignin foam is similar to that of foamed polystyrene, the strain at maximum stress is smaller, and the modulus of elasticity is larger.

Keywords: *biopolymers, biodegradable polymers, starch, lignin, water absorption*

1. Introduction

Biodegradable plastics made from renewable resources have received increased attention from polymer scientists, plastics manufacturers, and government agencies [1, 2]. The driving force for this interest derives from sustainability gains and environmental amelioration provided through a reduced dependence on petroleum reserves, increased disposal options, and lower levels of greenhouse gases. This development has accrued in spite of acknowledged challenges connected with material properties, recycling, and cost [3–5]. Most of the interest in biodegradable plastics is aimed at developing low cost composites that are economical in high-volume applications. Applications considered most relevant include packaging and consumer products.

Starch-based materials have been of particular interest [6–10] because of the generally low cost of starch, and because thermoplastic starch [6] can be processed with conventional means such as extrusion and injection molding.

Starch foams are one segment of starch-based materials. Interest in foams is based on their low density, relative to non-foamed materials, which leads to lower material costs. Also, starch foams are biodegradable, in contrast to foamed polystyrene which is recalcitrant. Starch foams have been produced by extrusion [11–14], solvent exchange [15], and molding by means of a compression/explosion process [16].

Starch foams can also be produced with a technique similar to compression molding, whereby a mixture of starch, water, and additives is deposited into

*Corresponding author, e-mail: stevens@binghamton.edu

heated molds [17]. Excess water is vented as steam as the mixture expands and fills the mold cavity. A small amount of the mixture tends to be forced through the vents, which builds pressure inside the mold and produces foaming [17, 18]. The properties of these foams and their dependence on composition and processing have been studied [18–21], largely with the aim of improving mechanical properties and moisture resistance.

There is also growing interest in lignin-based materials. Lignin is an abundant renewable natural resource. A byproduct of paper manufacture, lignin is considered a fairly intractable waste material and is usually burned as fuel for lack of higher-value uses. The properties and uses of lignin have recently been reviewed [22, 23]. Kumar *et al.* [24] have reviewed applications of lignin combined with other polymers.

Baumberger [25] has reviewed applications of lignin specifically in starch-lignin films. Stevens *et al.* [26] have examined thermoplastic starch-kraft lignin-glycerol blends prepared by film casting and by extrusion in a twin-screw extruder. Lignin is also produced as a byproduct in the refining process by which cellulose is isolated from lignocellulosic feedstocks. Starch-lignin materials can therefore be envisioned as becoming integrated into the production of bioethanol.

Starch-lignin foams have not previously been examined. The purpose of this study was to prepare and characterize starch-kraft lignin foams. The major applications for starch-lignin foams would be packaging containers for single or short-term use, as biodegradable alternatives to foamed polystyrene. Here the questions of interest were whether the presence of a significant amount of lignin would prevent foam formation or have any effect on water resistance and mechanical properties relative to starch foams.

2. Materials and sample preparation

Melojel cornstarch was purchased from National Starch and Chemical Company, Bridgewater, New Jersey. Indulin AT lignin (kraft pine lignin) was donated by MeadWestvaco, Charleston, South Carolina. Ammonium hydroxide (30% aqueous solution) was purchased from Fisher Scientific Company. Magnesium stearate was purchased from Aldrich Chemical Company.

Sample compositions are shown in Table 1. The water content of the starch, measured by heating at 130°C for 1 h and weighing at 20°C, was 11.6±0.1%. Sample 1 was a control, with a weight ratio of starch (dry weight) to water (total weight) equal to 1.00. In samples 2 and 3, 10 and 20% of the starch, respectively, was replaced with lignin. Water was added in an amount which kept the ratio of starch-plus-lignin to water equal to 1.00. Magnesium stearate was added as a release agent, at a level of 2.0% of the starch dry weight [19].

Lignin is soluble in aqueous solution only at high pH. In studies of starch-lignin cast films [26], ammonium hydroxide was used to raise the pH of the casting solution and was found to be a requirement for obtaining viable films. Preparing starch-lignin films by extrusion, on the other hand, had no significant high-pH requirement [26]. In the present study, samples were prepared both with and without ammonium hydroxide. In samples 2N and 3N, ammonium hydroxide was added as an aqueous solution (30%) in an amount equal to the estimated stoichiometric amount of OH protons in pine kraft lignin [27], 2.0 ml per 10 g lignin. The ammonium hydroxide is taken up by the starch-lignin mixture quickly so that after mixing there is no ammonia odor.

The dry ingredients were mixed manually. Water and, when used, ammonium hydroxide solution were added and the mixture again mixed manually. The mixture was placed in a 70°C water bath and

Table 1. Compositions

Sample	Starch[a] [g]	Water [g]	Lignin [g]	Mg stearate [g]	NH_4OH[b] [ml]
1	168	129	0	2.96	0
2	160	137	14.16	2.82	0
3	152	144	27.00	2.70	0
2N	160	137	14.16	2.82	2.83
3N	152	144	27.00	2.70	5.40

[a]The starch contained 11.6% water.

[b]Added as aqueous NH_4OH solution (30%)

heated with mixing for 10–15 minutes after which time it had thickened to a doughlike consistency.

Foam samples were prepared in an oven (Hebenstreit GmbH, Model ZQe, Germany) with rectangular 6.5 cm×11.1 cm molds. The mold was preheated to 170°C and 30 g samples were heated for 50–60 s. The resulting foam panels were approximately 0.2 cm thick. After cooling, the panels were cut into strips 2.5 cm×16.5 cm for density, water absorption, and flexural measurements.

3. Sample characterization

3.1. Morphology

For density measurements, samples were conditioned for 48 h at 20°C and 50% relative humidity. Density was determined by weighing the foam and calculating the volume from measured dimensions. Four specimens of each sample were used.

For scanning electron microscope (SEM) measurements, specimens of samples 1 and 3N were fractured in liquid nitrogen, dried, sputter-coated with Au-Pd, and examined with a Hitachi S-4700 scanning electron microscope.

For X-ray powder diffraction (XRD) analysis, specimens of samples 1 and 3N were ground to a powder with a mortar and pestle. Analysis was carried out with a Philips X-pert PW3040 MPD diffractometer operated at 40 kV and 20 mA using CuK_α radiation with a graphite diffracted beam monochromator. Data were acquired in steps of $2\theta = 0.04°$ and 4 s.

3.2. Differential scanning calorimetry (DSC)

Foam samples were first ground into a fine powder with a mortar and pestle to improve thermal contact with the aluminum DSC cells. The heating curve of kraft lignin alone was also obtained. DSC measurements were made with a Perking Elmer Jade instrument calibrated with indium (T, ΔH) and zinc (T). Samples (12.0–21.0 mg) were placed in cells and sealed at ambient temperature (23±2°C) and relative humidity (50±10%). Heating was from 30–130°C at 10°C/min. Measurements were made on 2–4 samples of each composition.

3.3. Water absorption

An immersion gravimetric method was used for measuring water absorption [28–30]. Specimens of samples 1 and 3N, 7.6×2.5×0.2 cm, were conditioned for 24 h at 50°C, weighed, then immersed in a 23°C water bath for specified times of 15 sec to 30 min. The foams were held vertically under water by two wires penetrating the foam and attached to a clamp, thereby maximizing exposure to water. After immersion, excess water was removed with absorbent paper and the specimens were reweighed. Two-to-four specimens were measured for each sample at each immersion time.

The amount of water that entered the sample per unit surface area at time t, m_t, was calculated. Different specimens were used for each immersion time, so values of m_t were normalized to a uniform sample weight (0.727 g), and divided by the surface area of a sample of that weight, calculated from the density measurements to be 35.4 cm^2.

3.4. Flexural properties

Before mechanical testing, samples were conditioned for 24 h at a temperature of 23±2°C and relative humidity of 53% using a saturated solution of $Mg(NO_3)_2$. Three-point flexural tests were carried out with an Instron Model 4500 testing machine according to ASTM Test Method D 790 [31]. Specimen width was 2.5 cm, span setting was 10.0 cm, and crosshead speed was 2.54 mm/min. The number of specimens of each sample was 6–8.

In this ASTM test method, flexural stress is calculated according to Equation (1):

$$\sigma_f = \frac{3PL}{2bd^2} \tag{1}$$

where σ_f is the flexural stress at the midpoint of the specimen, in MPa; P is the load at a given point on the load-deflection curve, in Newtons; L is the support span, in mm; b is the width of the specimen, in mm; and d is the thickness of the specimen, in mm. For the specimens used here, L = 100 mm, b = 25.4 mm, and d varied within a range near 2.0 mm. We report flexural strength, i.e., the maximum flexural stress, which uses the load (P) at the maximum on the load-deflection curve; e.g., for P = 2.0 N, σ_f = 3.0 MPa.

Flexural strain is calculated according to Equation (2):

$$\varepsilon_f = \frac{6Dd}{L^2} \quad (2)$$

where ε_f is the fractional change of an element of the outer surface of the specimen at the midpoint, in mm/mm; D is the maximum deflection of the center of the specimen, in mm; and L and d are as in Equation (1). We report flexural strain at maximum flexural stress, as a percent, $\varepsilon_f \cdot 100$; e.g., for D = 10 mm, ε_f = 1.2%.

The modulus of elasticity in bending is the ratio, within the elastic limit, of stress to corresponding strain, as in Equation (3):

$$E_b = \frac{L^3 m}{4bd^3} \quad (3)$$

where E_b is the modulus of elasticity in bending, in MPa; m is the slope of the tangent to the initial straight-line portion of the load-deflection curve, in N/mm of deflection; and L, b, and d are as in Equation (1).

4. Results and discussion

4.1. Morphology

Figure 1 shows optical scans of a starch and starch-lignin foam. Lignin imparts a brown color.

Foam densities are shown in Table 2. The density of the control sample is the same as that previously reported [19] for a similarly processed foam having a 1:1 starch:water composition (0.22 g/cm^3). Foam density is known to depend on starch source, water content, heating temperature, and heating time [18, 19].

Lignin has little effect on foam density. The difference between samples 2N and 3N is only marginally significant but suggests that the effect of ammonium hydroxide on density may depend on the amount of lignin present. For example, it may be that lignin has the effect of decreasing foam density, whereas ammonium hydroxide has the effect of increasing foam density.

Figure 1. Optical scans of starch foam (top) and starch-lignin foam (bottom)

Table 2. Sample densities[a]

Sample	Density [g/cm^3]
1	0.23 ± 0.02
2	0.24 ± 0.02
3	0.21 ± 0.01
2N	0.31 ± 0.07
3N	0.24 ± 0.03

[a]Average values ± estimated standard deviation (N = 4)

Typical densities of foamed polystyrene are 0.06–0.09 g/cm^3 [16, 18, 19], less than what is observed here. However, starch foams prepared by extrusion [13] have densities of approximately 0.06–0.07 g/cm^3, similar to foamed polystyrene. Extrusion may lead to lower densities in starch-lignin foams than foams obtained with the present method.

SEM images of samples 1 and 3N are shown in Figure 2. The features of starch foams (Figure 2a) have been observed previously [17, 18]. Below a thin surface 'skin' of approximately 100 μm in thickness, there is a region of cellular structure containing 100–200 μm voids. The major internal region of the foam consists of large voids of up to 1 mm in size. The boundaries separating these regions are not sharp, but the combined thickness of the outer skin and smaller voids in the present micrographs is approximately 0.045 cm, similar to what has been observed previously [17, 18].

Starch-lignin foams display the same features (Figure 2b). Lack of contrast makes the location of the dispersed lignin impossible. Nevertheless, the SEM images show that 20% lignin can be incorporated into starch foams without collapse of the foam and with no major change in morphology.

Figures 2c and 2d show enlarged images of samples 1 and 3N, respectively. The walls of the internal cells are approximately 10 μm thick, whether or not the foams contain lignin.

Therefore, SEM indicates that replacing 20% of the starch with lignin has no deleterious effect on overall morphology.

X-ray diffraction patterns of samples 1 and 3N are shown in Figure 3. The significant diffraction maximum at 19.4° and a weaker maximum at 12.7° in both samples indicate the presence of residual

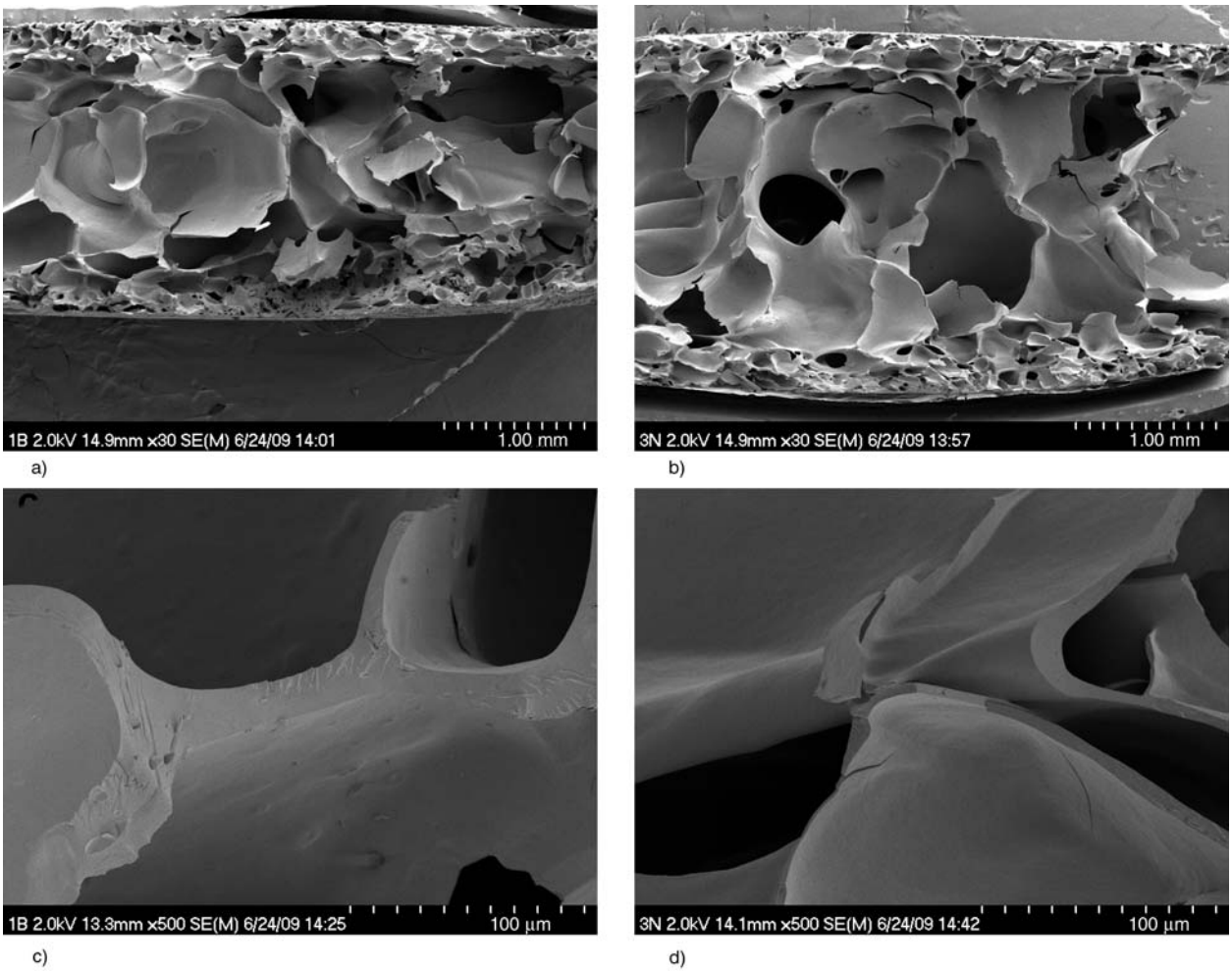

Figure 2. SEM images of (a) starch (sample 1), (b) starch-lignin (sample 3N), (c) starch (sample 1), and (d) starch-lignin (sample 3N)

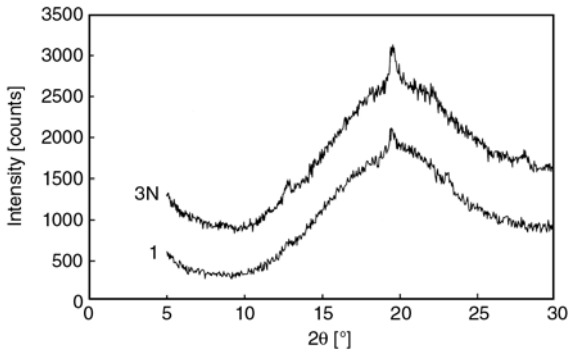

Figure 3. Powder X-ray diffraction patterns of foams of starch (sample 1) and starch-lignin (sample 3N)

structure of the V form of starch [13, 18, 32]. The absence of the B structure indicates that the native structure in the starch granule was destroyed during foam formation. Some of the amylose probably recrystallized into the V form during the cooling [32].

4.2. Differential scanning calorimetry

Figure 4 shows the heating curves of the five samples described in Table 1. The starch foam (curve 1) displays, within the measured temperature range, a broad endothermic peak and a second smaller feature. Peak temperatures, averaged over four specimens, were 85±1 and 95±2°C, respectively. The integrated area, including both features and averaged over four specimens, corresponds to ΔH = 2.0±0.1 J/g of dry starch.

DSC features observed with starch samples depend on water content, age, source plant, and sample history [32–34]. For our purposes, the thermal features in the starch foam (Figure 4, curve 1) need only be taken to indicate that heat treatment of starch during foam formation leaves some residual starch structure [32]. XRD analysis (above) indicates that structure to be the V form of amylose.

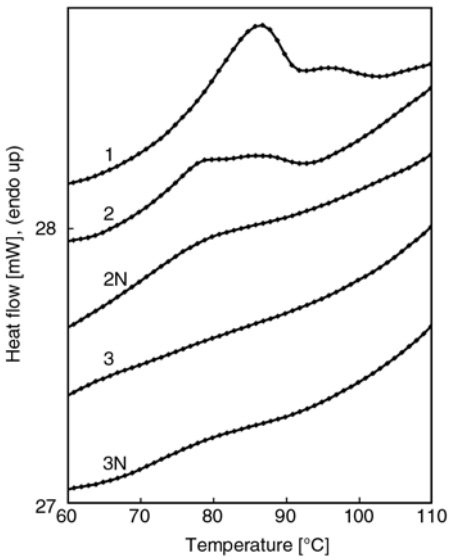

Figure 4. DSC curves for the samples described in Table 1. The curves have been displaced on the vertical axis for ease in viewing.

Sample 2, containing 10% lignin and prepared without ammonium hydroxide, similarly shows two thermal features but shifted to lower temperatures, approximately 78 and 86°C, and with a decreased enthalpy change of 0.91±0.02 J/g of starch. The remaining samples show no distinct thermal features ($\Delta H \leq 0.3$ J/g of starch).

X-ray diffraction analysis indicates the presence of residual structure in both samples 1 and 3N, but only sample 1 displays a thermal transition by DSC. This result indicates that, when lignin is present, starch-lignin interactions are sufficient to inhibit the thermal transition, as in sample 3N.

As a control experiment, the DSC of the lignin used in this work was measured (Figure 5). Upon first heating (curve a) there is a broad endothermic peak at 80±2°C with ΔH = 5.7±0.6 J/g. After cooling and reheating (curve b) the same sample shows no

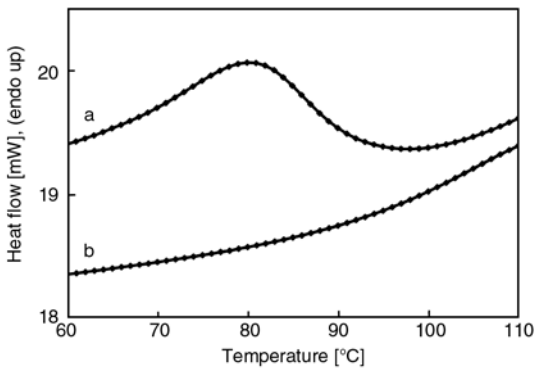

Figure 5. DSC curves for lignin; (a) first heating, (b) second heating. The curves have been displaced on the vertical axis for ease in viewing.

thermal features in the temperature range examined here. Therefore, following foam formation, lignin does not contribute to the DSC data displayed in Figure 4.

The data also suggest that the effect of ammonium hydroxide on thermal features, as with its effect on foam density (above), depends on the amount of lignin present: at 10% lignin the melting features are absent only when ammonium hydroxide is used, whereas at 20% lignin the melting features are absent whether or not ammonium hydroxide is used. This result could be a concentration dependent phenomenon related to the way in which lignin is dispersed throughout the foam.

A hypothesis for the action of ammonium hydroxide is that dissolution of lignin at high pH involves phenolate formation in the lignin component; the pK_a of phenol is 9.9. Phenolate ions then interact with hydroxyl groups of the starch through ion-dipole interactions, supplementing hydrogen-bonding dipole-dipole interactions. Some ammonium ions remain as phenolate counterions and excess ammonia escapes during the mixing and heating processes. By the time the foams are formed, there is no free ammonia and no ammonia odor.

4.3. Water absorption

An empirical power law model has often been used to describe polymer absorption dynamics [35, 36] (Equation 4):

$$m_t = kt^n \tag{4}$$

where m_t is the mass of absorbed water per unit area at time t; k is an empirical rate parameter proportional to $D^{1/2}$, where D is the diffusion constant; and n is a parameter related to the diffusion mechanism. When n is equal to 0.5 the dynamics are referred to as Fickian [29, 30, 35, 36].

Figure 6 shows a plot of m_t versus $t^{1/2}$ for samples 1 (starch) and 3N (starch-lignin), with m_t in units of g/cm^2 and t in seconds. The behavior is initially linear, but the slopes increase at longer times. The results of this empirical model indicate qualitatively that lignin impedes the absorption of water. The ratio of the limiting slopes, at short times, for samples 1 and 3N is approximately 2:1, indicating a ratio of effective diffusion constants of approximately 4:1. This simple empirical model, however, provides little insight into the mechanism of diffu-

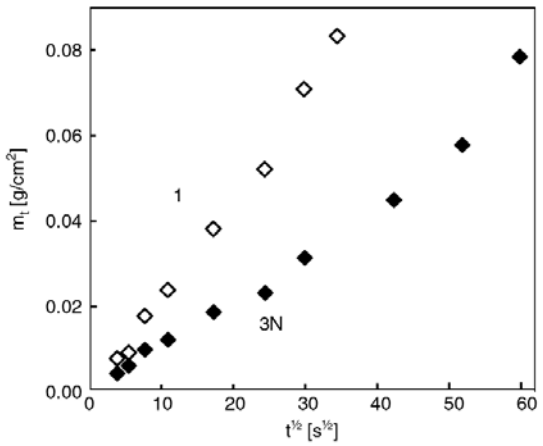

Figure. 6. Water absorption described by an empirical power law model (Equation 4). Sample 1, starch; sample 3N, starch-lignin.

sion and does not explain the departure from linearity in Figure 6 at long times.

Crank [37], on the other hand, provides a non-empirical, analytical solution to Fick's diffusion equations for boundary conditions appropriate to the present materials; i.e., diffusion into a slab having an outer layer of thickness, l, through which diffusion is determined by a diffusion constant, D. It is assumed that further movement of water into the core is unhindered.

The large voids in the present materials led us to examine that model. The specimens were cut from the original larger samples, exposing voids along the edges, but for the sample sizes used here, only 10% of the surface area was exposed.

In such a model, solutions to Fick's diffusion equations are obtained [37] as in Equation (5):

$$\frac{m_t}{2lc_0} = \left(\frac{Dt}{l^2}\right)^{1/2} \frac{1}{\sqrt{\pi}} \left\{1 + 2\sum_{n=1}^{\infty} \exp\left(-\frac{n^2 l^2}{Dt}\right)\right\} - 2\sum_{n=1}^{\infty} n\,\mathrm{erfc}\left(\frac{nl}{\sqrt{Dt}}\right) \quad (5)$$

where c_0 is the water concentration at the surface, 1.00 g/cm^3, and erfc is the error function complement. The thickness of the outer region, l, was estimated from the SEM images (Figure 2) to be 0.045 cm.

Equation (5) contains only the single fit parameter, D. Crank [37] points out that when $m_t/2lc_0$ is plotted as a function of $(Dt/l^2)^{1/2}$, the curve is expected to be linear for small times but that its gradient later increases steadily as t increases. When plotted as a function of Dt/l^2 the curve is initially parabolic, then becomes linear. Data for samples conforming to the model will be superimposed, with data for different samples being distinguished by different values of the fitted parameter, D.

Data for each of samples 1 and 3N were fit to Equation (5) by minimizing χ^2. For sample 1 (starch), $D = 2.68 \cdot 10^{-6}$ cm^2/sec, with a standard deviation for the fit of 0.036. For sample 3N (starch-lignin), $D = 0.80 \cdot 10^{-6}$ cm^2/sec, with a standard deviation for the fit of 0.026.

Figure 7 shows the present data plotted as a function of $(Dt/l^2)^{1/2}$, displaying the expected initial linear behavior and significant curvature at longer times. Figure 8 shows the data plotted as a function of Dt/l^2, displaying the initial parabolic behavior and the expected linear behavior at longer times.

Equation (5) accounts satisfactorily for the data of both samples. Lignin impedes diffusion into the outer layers of the foam but does not affect the diffusion mechanism. The ratio of the two effective diffusion constants is 3.4, indicating a significant improvement in water resistance in the starch-lignin foam.

Baumberger *et al*. [38], who studied starch-lignin films, also found that lignin improves water resistance, as long as no plasticizer is used. Stevens *et al*. [26] found that if glycerol is used to plasticize starch-lignin films, the effect of the glycerol is to reduce or eliminate the hydrophobic effect of lignin.

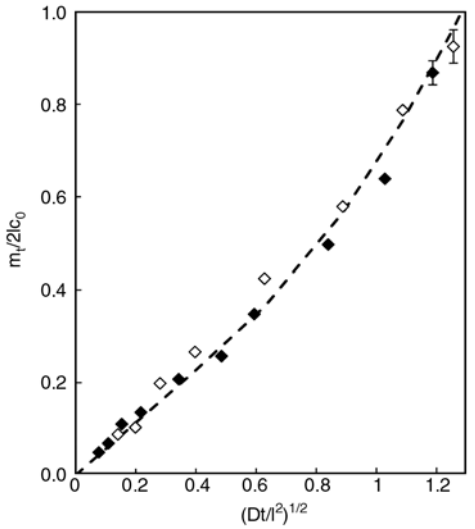

Figure 7. Water absorption as a function of $(Dt/l^2)^{1/2}$ as described by Equation (5); ◇, starch (sample 1); ◆, starch-lignin (sample 3N). The dashed line represents the best fit to Equation (5); the error bars show the standard deviation of the fit.

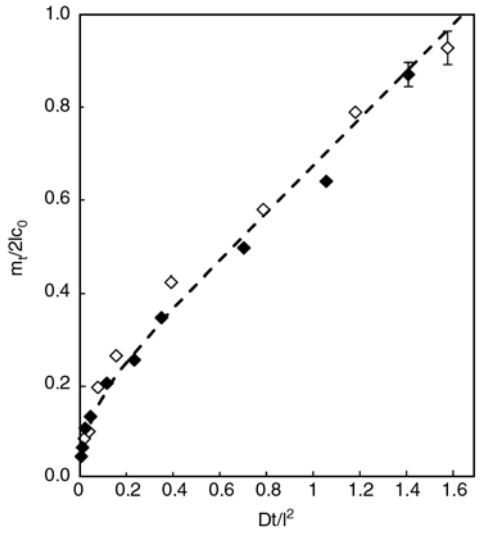

Figure 8. Water absorption as a function of $(Dt/l^2)^{1/2}$ as described by Equation (5); ◇, starch (sample 1); ◆, starch-lignin (sample 3N). The dashed line represents the best fit to Equation (5); the error bars show the standard error of the fit.

4.4. Flexural properties

The load deflection curves for the starch control samples showed an increase in strain beyond the point of maximum stress; they showed a yield. Beyond the yield, there was an additional strain of approximately 0.2% before the sample broke. On the other hand, foams containing lignin displayed no yield; they broke at the maximum measured stress.

Flexural properties are shown in Table 3. Shogren *et al*. [39] and Lawton *et al*. [40] have shown that starch content, plant source, and moisture content affect the mechanical properties of foams prepared by the present method. Results for the control sample can be compared with reported values [19] representing averages for corn, wheat, potato and tapioca starch foams and prepared with a 1:1 starch: water composition: flexural strength, 4.7 MPa; strain at maximum stress, 2.2%; modulus of elasticity, 281 MPa.

Table 3. Flexural properties[a]

Sample	N[b]	Flexural strength [MPa]	Strain at maximum stress [%]	Modulus of elasticity [MPa]
1	6	2.61 ± 0.32	1.4 ± 0.1	235 ± 37
2	8	2.20 ± 0.28	0.7 ± 0.1	348 ± 24
3	8	2.44 ± 0.30	0.6 ± 0.1	395 ± 32
2N	8	2.71 ± 0.55	0.7 ± 0.4	518 ± 149
3N	7	1.56 ± 0.56	0.6 ± 0.2	296 ± 55

[a]Average values ± estimated standard deviation.
[b]Number of specimens.

Foams with 10% lignin or 20% lignin, prepared without ammonium hydroxide (samples 2 and 3), displayed the same flexural strength as the starch control, a decreased strain at maximum stress, and a larger modulus of elasticity.

Foams with 10% lignin, prepared with ammonium hydroxide (sample 2N), displayed the same flexural strength and strain at maximum stress as foams prepared without ammonium hydroxide, but a larger modulus of elasticity; the increase in modulus between samples 2 and 2N is significant at the 99% confidence level.

In foams with 20% lignin and prepared with ammonium hydroxide (sample 3N), the ammonium hydroxide had the effect of significantly decreasing flexural strength (99% confidence level), but had no further effect on strain at maximum stress. The modulus of elasticity decreased relative to the other lignin-containing samples, but was larger than the value for the starch control (95% confidence level). Thus, the effect of ammonium hydroxide appears to depend on the amount of lignin present.

The present results can be compared with those of Baumberger *et al*. [38] who prepared starch-kraft lignin pre-extruded molded films containing only water as a plasticizer. They observed tensile elongations at break of 1.0–1.5%. Without additional plasticization, lignin increases the brittleness of both films and foams.

For comparison, the values for foamed polystyrene are: flexural strength, 1.3 MPa; strain at maximum stress, 1.7%; and modulus of elasticity, 105 MPa [19]. The flexural strength of starch-kraft lignin foams is, therefore, similar to that of foamed polystyrene; the strain at maximum stress is smaller, and the modulus of elasticity is larger.

Starch foams have also been produced by extrusion and other means [11–16], and the mechanical and other properties of starch-lignin foams are likely to depend on processing.

5. Conclusions

Replacing 20% of the starch with lignin does not prevent foam formation and has no deleterious effect on foam density or morphology. Lignin significantly decreases the rate of water absorption.

XRD and DSC together indicate that there are significant starch-lignin interactions that stabilize residual structure in the starch. Starch-lignin foams prepared by the present method have approximately the same flexural strength as foamed polystyrene, a smaller strain at maximum stress, and a larger modulus of elasticity.

Acknowledgements

We thank MeadWestvaco for donations of Indulin AT. The technical assistance of Tina Williams, Marie Cope, and David M. Jenkins is gratefully acknowledged.

References

[1] Chiellini E., Solaro R.: Biodegradable polymers and plastics. Plenum Press, New York (2003).

[2] Wool R. P., Sun X. S.: Bio-based polymers and composites. Elsevier, Amsterdam (2005).

[3] Zhang M. Q.: Polymeric materials from natural resources- Emerging as the times require. Express Polymer Letters, **1**, 406 (2007).
DOI: 10.3144/expresspolymlett.2007.57

[4] Krawczak P.: Plastics and composites based on renewable resources: End-of-life recycling and recovery issues. Express Polymer Letters, **2**, 237 (2008).
DOI: 10.3144/expresspolymlett.2008.28

[5] Karger-Kocsis J.: Thermoset polymers containing bio-based renewable resources. Express Polymer Letters, **3**, 676 (2009).
DOI: 10.3144/expresspolymlett.2009.84

[6] Avérous L.: Biodegradable multiphase systems based on plasticized starch: A review. Journal of Macromolecular Science Polymer Reviews, **44**, 231–274 (2004).
DOI: 10.1081/mc-200029326

[7] Tábi T., Kovács J. G.: Examination of injection moulded thermoplastic maize starch. Express Polymer Letters, **1**, 804–809 (2007).
DOI: 10.3144/expresspolymlett.2007.111

[8] Cao X., Chen Y., Chang P. R., Muir A. D., Falk G.: Starch-based nanocomposites reinforced with flax cellulose nanocrystals. Express Polymer Letters, **2**, 502–510 (2008).
DOI: 10.3144/expresspolymlett.2008.60

[9] Wittek T., Tanimoto T.: Mechanical properties and fire retardancy of bidirectional reinforced composite based on biodegradable starch resin and basalt fibres. Express Polymer Letters, **2**, 810–822 (2008).
DOI: 10.3144/expresspolymlett.2008.94

[10] Lu D. R., Xiao C. M., Xu S. J.: Starch-based completely biodegradable polymer materials. Express Polymer Letters, **3**, 366–375 (2009).
DOI: 10.3144/expresspolymlett.2009.46

[11] Lacourse N. L., Altieri P. A.: Biodegradable packaging material and the method of preparation thereof. U. S. Patent 4863655, USA (1989).

[12] Harper J. M., Tribelhorn R. E.: Expansion of native cereal starch extrudates. in 'Food extrusion science and technology' (eds.: Kokini J. L., Ho C., Karwe M. V.) Marcel Dekker, New York, 653–667 (1992).

[13] Willett J. L., Shogren R. L.: Processing and properties of extruded starch/polymer foams. Polymer **43**, 5935–5947 (2002).
DOI: 10.1016/S0032-3861(02)00497-4

[14] Glenn G., Klamczynski A., Holtman K. M., Chiou B-S., Orts W. J., Wood D.: Cellulose fiber reinforced starch-based foam compositions. Journal of Biobased Materials and Bioenergy, **1**, 360–366 (2007).
DOI: 10.1166/jbmb.2007.010

[15] Glenn G. M., Irving D. W.: Starch-based microcellular foams. Cereal Chemistry, **72**, 155–161 (1995).

[16] Glenn G. M., Orts W. J.: Properties of starch-based foam formed by compression/explosion processing. Industrial Crops and Products, **13**, 135–143 (2001).
DOI: 10.1016/S0926-6690(00)00060-1

[17] Tiefenbacher K. F.: Starch-based foamed materials – Use and degradation properties. Journal of Macromolecular Science, Pure and Applied Chemistry A, **30**, 727–731 (1993).

[18] Shogren R. L., Lawton J. W., Doane W. M., Tiefenbacher K.: Structure and morphology of baked starch foams. Polymer, **39**, 6649–6655 (1998).
DOI: 10.1016/S0032-3861(97)10303-2

[19] Glenn G. M., Orts W. J., Nobes G. A. R.: Starch, fiber and $CaCO_3$ effects on the physical properties of foams made by a baking process. Industrial Crops and Products, **14**, 201–212 (2001).
DOI: 10.1016/S0926-6690(01)00085-1

[20] Shogren R. L., Lawton J. W., Tiefenbacher K. F.: Baked starch foams: Starch modifications and additives improve process parameters, structure and properties. Industrial Crops and Products, **16**, 69–79 (2002).
DOI: 10.1016/S0926-6690(02)00010-9

[21] Lawton J. W., Shogren R. L., Tiefenbacher K. F.: Aspen fiber addition improves the mechanical properties of baked cornstarch foams. Industrial Crops and Products, **19**, 41–48 (2004).
DOI: 10.1016/S0926-6690(03)00079-7

[22] Glasser W. G., Northey R. A., Schultz T. P.: Lignin: Historical, biological, and materials perspectives. American Chemical Society, Washington (2000).

[23] Hu T. Q.: Chemical modification, properties, and usage of lignin. Plenum Press, New York (2002).

[24] Kumar M. N. S., Mohanty A. K., Erickson L., Misra M.: Lignin and its applications with polymers. Journal of Biobased Materials and Bioenergy, **3**, 1–24 (2009).
DOI: 10.1166/jbmb.2009.1001

[25] Baumberger S.: Starch-lignin films. in 'Chemical modification, properties, and usage of lignin' (ed.: Hu T. Q.) Plenum Press, New York, 1–19 (2002).

[26] Stevens E. S., Willett J. L., Shogren R. L.: Thermoplastic starch-kraft lignin-glycerol blends. Journal of Biobased Materials and Bioenergy, **1**, 351–359 (2007).

[27] McCarthy J. L., Islam A.: Lignin chemistry, technology, and utilization: A brief history. in 'Lignin: Historical, biological, and materials perspectives' (eds.: Glasser W. G., Northey R. A., Schultz T. P.) American Chemical Society, Washington, 2–99 (2000).

[28] ASTM D 570: Standard test method for water absorption of plastics (2007).

[29] Abacha N., Kubouchi M., Sakai T.: Diffusion behavior of water in polyamide 6 organoclay nanocomposites. Express Polymer Letters, **3**, 245–255 (2009).
DOI: 10.3144/expresspolymlett.2009.31

[30] Berketis K., Tzetzis D.: Long-term water immersion ageing characteristics of GFRP composites. Journal of Material Science, **44**, 3578–3588 (2009).
DOI: 10.1007/s10853-009-3485-9

[31] ASTM D 790: Standard test methods for flexural properties of unreinforced and reinforced plastics and electrical insulating materials (2007).

[32] Shogren R. L., Jasberg B. K.: Aging properties of extruded high-amylose starch. Journal of Environmental Polymer Degradation, **2**, 99–109 (1994).
DOI: 10.1007/BF02074778

[33] Shogren R. L.: Effect of moisture content on the melting and subsequent physical aging of cornstarch. Carbohydrate Polymers, **19**, 83–90 (1992).
DOI: 10.1016/0144-8617(92)90117-9

[34] Maaruf A. G., Che Man Y. B., Asbi B. A., Junainah A. H., Kennedy J. F.: Effect of water content on the gelatinisation temperature of sago starch. Carbohydrate Polymers, **46**, 331–337 (2001).
DOI: 10.1016/S0144-8617(00)00335-0

[35] Masaro L., Zhu X. X.: Physical models of diffusion for polymer solutions, gels and solids. Progress in Polymer Science, **24**, 731–775 (1999).
DOI: 10.1016/S0079-6700(99)00016-7

[36] Meinders M. B. J., von Vliet T.: Modeling water sorption dynamics of cellular solid food systems using free volume theory. Food Hydrocolloids, **23**, 2234–2242 (2009).
DOI: 10.1016/j.foodhyd.2009.05.007

[37] Crank J.: The mathematics of diffusion. Oxford University Press, New York (1975).

[38] Baumberger S., Lapierre C., Monties B., Della Valle G.: Use of kraft lignin as filler for starch films. Polymer Degradation and Stability, **59**, 273–277 (1998).

[39] Shogren R. L., Lawton J. W., Teifenbacher K. F., Chen L.: Starch poly(vinyl alcohol) foamed articles prepared by a baking process. Journal of Applied Polymer Science, **68**, 2129–2140 (1998).
DOI: 10.1002/(SICI)1097-4628(19980627)68:13<2129::AID-APP9>3.0.CO;2-E

[40] Lawton J. W., Shogren R. L., Tiefenbacher K. F.: Effect of batter solids and starch type on the structure of baked starch foams. Cereal Chemistry, **76**, 682–687 (1999).

eXPRESS Polymer Letters Vol.4, No.5 (2010) 321–327
Available online at www.expresspolymlett.com
DOI: 10.3144/expresspolymlett.2010.40

Effect of polyaspartic acid on hydroxyapatite deposition in silk fibroin blend films

*X. L. Ma, R. Li, L. Ru, G. W. Xu, Y. P. Huang**

School of Chemistry and chemical engineering, Key Laboratory of Environment-friendly Polymer Materials of Anhui Provinc, Anhui University; 230039 Hefei, Anhui Province, China

Received 28 December 2009; accepted in revised form 19 March 2010

Abstract. Polyaspartic acid/silk fibroin/hydroxyapatite (PASP/SF-HA) composites have been synthesized by biomimetic processing. SF solution was mixed with different contents of PASP to prepare the PASP/SF blend membranes. After ethanol treatment and premineralization process, the blend membranes were immersed into 1.5 simulated body fluid (1.5 SBF) for 24 h to induce apatite deposition at 37±0.5°C. Fourier transform infrared spectroscopy (FTIR) and X-ray diffraction (XRD) results revealed that a conformation transition of SF occurred after the addition of PASP and ethanol treatment. The FTIR and XRD results also confirmed that the main component of apatite deposition was HA. Scanning electron microscopy (SEM) showed that the content of HA increased with increasing PASP concentration .Inductively Coupled Plasma-Atomic Emission Spectrometry (ICP) results revealed that the Ca/P molar ratio could reach 1.45, which was close to the Ca/P ratio of apatite. It was appropriate to conclude that the increasing content of PASP had a distinct effect on HA deposition in the blend films.

Keywords: *biopolymers, biocomposites, hydroxyapatite, silk fibroin, conformation transition*

1. Introduction

Hydroxyapatite (HA) with the chemical formula of $Ca_{10}(PO_4)_6(OH)_2$, is the major mineral part of natural bones and teeth. HA is the most commonly used apatite-based biomaterial due to its excellent biocompatibility, osteoconductivity and bioactivity [1, 2]. In the past decades, many efforts have been focused on the biomimetic growth of nano-HA through the combination of biodegradable polymers or proteins for bone tissue engineering [3–6]. Among these polymers, collagen is the best known tissue-derived natural polymer and has been used as tissue-culture scaffolds. However, the practical problems with collagen are its cost, and a limited range of physical properties unless extensively crosslinked, which alters biological response [7, 8]. Silk fibroin (SF), used as an appealing alternative polymer, possesses impressive mechanical properties and appreciable bioactivity that make it attractive for artificial bones [9, 10]. Kong *et al.* [11] employed SF to regulate the mineralization of HA . The effects of SF content on the microstructure and physico-chemical properties of the composite had also been studied [12]. In order to expand its application in biomaterials, the water-insoluble SF films were also prepared by inducing the structure transition from unstable silk I to silk II. The transition was commonly studied through treatment of aqueous ethanol solution [13, 14]. At the same time, biodegradable polymers such as chitosan [15], cellulose [16] and sodium alginate [17] have been widely used in the conformation transition of SF. Recently, Kim *et al.* [18] used aqueous-derived porous SF scaffolds mixing with PASP to deposit apatite, which provided an appropriate osteogenic environment for tissue engineering. However, the

*Corresponding author, e-mail: yphuang2001@sina.com.cn

effect of PASP on the conformation transition of SF has not yet been studied in detail.

In this work, pure SF and various blend ratios of PASP/SF films were prepared. After a premineralization process, the films were immersed into 1.5 SBF for 24 h to synthesize PASP/SF-HA composite. FT-IR, SEM and XRD spectroscopy were used to study the conformation transition of SF and the morphology of the obtained composite films. After the addition of PASP and treatment of ethanol, the silk I conformation had been transformed to silk II, which enhanced the deposition of HA. The results reported here may provide some information about a new strategy for the synthesis of other composite materials.

2. Materials and methods

2.1. Materials

Na_2CO_3, LiBr, NaCl, $NaHCO_3$, KCl, $K_2HPO_4{\cdot}3H_2O$, $MgCl_2{\cdot}6H_2O$, HCl, $CaCl_2$, Na_2SO_4, NaOH, tris(hydroxymethyl) aminomethane (Tris) and ethanol used here were analytical grade and purchased from Huipu Chemical Agents Co. Ltd. (Hangzhou, China). B. mori silkworm cocoons were provided by Anhui Agricultural Research Institute.

2.2. Preparation of SF films and PASP/SF scaffolds

B. mori silkworm cocoons were boiled for 30 min in an aqueous solution of 0.5% (w/v) Na_2CO_3 and then rinsed thoroughly with distilled water to extract the glue-like sericin protein. The treatment was repeated two times to get the pure silk fibroin. The degummed silk fibroin was air-dried at ambient temperature and dissolved in 9.5M LiBr solution for 4 hours at 50°C followed by a dialysis (MWCO 14000) against distilled water for 3 days. The final concentration of aqueous silk fibroin solution was approximately 2.7% (w/v). Then the solutions were stored in a refrigerator at 7–8°C before being used. Then, aqueous SF solution was cast onto polytetrafluoroethylene plates and dried at room temperature for the preparation of SF films. For the preparation of the blend membranes different amounts of PASP solution were added to SF solution under mild stirring for 2 min. The mixing solutions were poured into the polytetrafluoroethylene plates and air-dried at room temperature. The formed PASP/SF films were then treated with 60% (v/v) ethanol aqueous solution for 20 min.

2.3. Premineralization and mineralization

The alternate soaking process was used to grow apatite on silk fibers. First, SF films and PASP/SF scaffolds were soaked in 50 ml of 0.2M $CaCl_2$ solution (buffered with 0.05M Tris·HCl, pH 7.4) for 1 min and washed two times with distilled water. The PASP/SF scaffolds were then transferred to 50 ml of 0.12M K_2HPO_4 solution, soaked for 1 min and washed two times with distilled water. The soaking cycles were repeated 3 times. The whole process performed at 37°C.

The premineralized PASP/SF scaffolds were subsequently immersed into 1.5 SBF (Table 1) at 37°C for 24 h, followed by rinsing with deionized water and air-drying at room temperature.

Table 1. Composition of 1.5 SBF (pH 7.4) and order of addition of the reagents to water [19]

Order	Reagent	Weight [g·l^{-1}]
1	NaCl	12.0540
2	$NaHCO_3$	0.5280
3	KCl	0.3375
4	$K_2HPO_4{\cdot}3H_2O$	0.3450
5	$MgCl_2{\cdot}6H_2O$	0.4665
6	1M HCl	15.00 ml
7	$CaCl_2$	0.4440
8	Na_2SO_4	0.1080
9	$C_4H_{11}NO_3$ (Tris)	9.0945
10	1M HCl	50.00 ml

2.4. Characterization

The FT-IR spectra of samples were measured with Fourier transform infrared spectroscopy (FTIR) (Nicolet NEXUS-870, USA), the apatite deposited SF films samples were mixed with KBr in the mass ratio of 1:20–30. Infrared spectra were taken in the range of 4000–400 cm^{-1} with 4 cm^{-1} resolution. To investigate the structure and crystallinity, the milled sample powder were analyzed on an X-ray powder diffractometer (XRD) (Philiphs X'Pert-Pros, Dutch) using a diffractometer equipped for Cu-K_α radiation ($\lambda = 0.15418$ nm) in the 2θ range of 10–60° at 40 kV and 30 mA. The morphology of apatite deposited SF films sputtered with gold was

examined using scanning electron microscopy (SEM) (S-4800, Hitachi, Japan) with an accelerating voltage of 5 kV. The content of Ca and P elements in the composites was analyzed by Inductively Coupled Plasma-Atomic Emission Spectrometry (ICP) (IRIS Intrepid II ICP-OES, Thermo ELECTRON CORPORPORATION, USA). The milled composites samples were dissolved with HNO_3 and $HClO_4$, then they were filled to constant volume, with distilled water to 25 ml.

3. Results and discussion

3.1. FTIR

The conformational transition of SF and the composite films were studied by FT-IR spectroscopy (Figure 1). Figure 1a shows the characteristic peaks of PASP, including the C=O peaks at 1733 cm^{-1} and the C–N stretching vibrational frequencies at 1398 cm^{-1}, the bands at 3358 and 1586 cm^{-1} corresponding to the stretching vibration and bending vibration of N–H bonds, respectively. The bands for pure SF (Figure 1b) at 1658 cm^{-1} (amide I), 1550 cm^{-1} (amide II), 1243 cm^{-1} (amide III) and 670 cm^{-1} (amide V) were attributed to silk I form. After the addition of PASP, the band at 1658 cm^{-1} showed an obvious shift, the 1550 and 1243 cm^{-1} bands shift to lower wave number, the shifts were 7 and 4 cm^{-1}, respectively. Furthermore, the shift of amide peaks was more evident after ethanol treatment. In order to clearly reflect conformation transition of the SF in the blend membranes, the spectral ranges of 1800–600 cm^{-1} were shown in Figure 1B. The amide I and amide II bands for the PASP/SF composite films were shifted from 1658 to 1662 and 1550 to 1542 cm^{-1}, respectively, and a small sharp peak at 1649 cm^{-1} appeared, indicating that a partial conformation transition from silk I to silk II structure occurred [11]. After treated with ethanol, the amide I bands were shifted to 1634 cm^{-1} with a shoulder at 1694 cm^{-1}, which could be assigned to β-turns [20, 21]. Amide II and amide III bands were shifted to 1526 and 1233 cm^{-1}, respectively. The shift of amide bands demonstrated that intermolecular interactions may be formed between the polymer functional groups, such as hydrogen bonding of carbonyl groups of PASP, hydroxyl groups of ethanol, amide groups of SF, which might be related to the conformational transition of SF. From the above results, it was obvious that the addition of PASP changed the structure of SF, and ethanol treatment can further promote this change.

Figure 2 shows the FT-IR spectra of the mineralized scaffolds prepared from various blend ratios of PASP/SF solutions. It could be seen that the spectra of the mineralized scaffolds displayed the absorption bands at 1040, 603 and 564 cm^{-1} (Figure 2: a, b, c, d), and the intensity of these peaks gradually enhanced with the increasing content of PASP. Compared with the infrared data of pure HA (Fig-

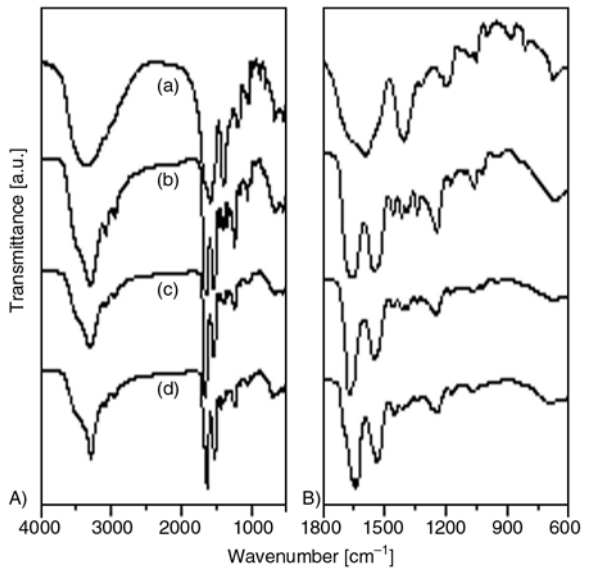

Figure 1. FT-IR spectra of (a) PASP, (b) SF, (c) PASP/SF and (d) PASP/SF treated with 60% (v/v) ethanol aqueous solution. The blend ratio of PASP/SF solution was 10% (w/w). (A) 4000–500 cm^{-1} range. (B) Detail of the 1800–600 cm^{-1} region.

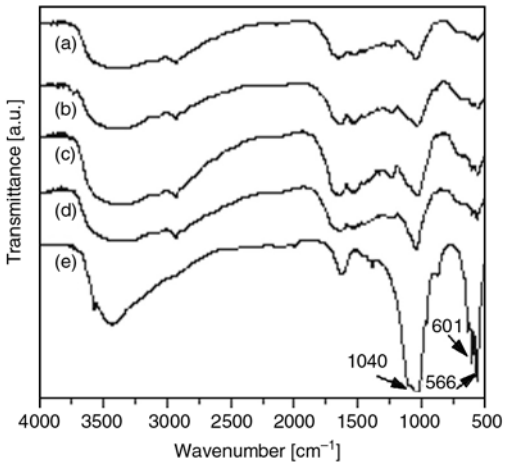

Figure 2. FT-IR spectra of the mineralized scaffolds prepared from various blend ratios of PASP/SF solutions (a: 0%; b: 5%; c: 10%; d: 15%) and (e) HA

ure 2e), the predominant component of the resultant inorganic phase was HA. The results indicated that HA had been successfully deposited on the surface of PASP/SF blend membranes and the carbonyl groups of PASP in the organic template induced the nucleation of HA [22].

3.2. XRD

Figure 3 displayed XRD patterns of the prepared scaffolds. For the pure SF film (Figure 3a), only a weak and wide halo pattern appeared, this exceedingly discrete powder diagram belonged to silk I [23, 24].According to the studies on silk fibroin molecular conformation [25], the X-ray diffraction patterns had been determined as follows, 11.5° (2θ) for α-helix structure, and 20.2° (2θ) for β-sheet structure. It could be seen from curve (b) that the composite sample showed two peaks around 11.8° (2θ) and 20.2° (2θ). Its molecular conformation exhibited a coexistence of α-helix and β-sheet structure, indicating that PASP partly induced the conformation of SF from silk I to silk II. The characteristic peaks (2θ = 20.2°) of β-sheet became more intensive with the treatment of 60% (v/v) ethanol aqueous solution (Figure 3b, 3c). It showed that the essential changes of silk fibroin molecular conformation have taken place during the treatment by ethanol.

Figure 3d displays XRD patterns of the PASP/SF-HA composite. As shown in Figure 3d, after soaking in 1.5 SBF for 24 h, the clear but weak diffraction peaks were detected at 25.9° (2θ) and 31.9° (2θ) corresponding to the (002) and (211) planes of HA crystal (verified by PDF Card No.09-0432). The result also confirmed that the predominant component of the inorganic phase was HA. The broadened peaks of the (002) and (211) crystal planes showed an imperfect crystallization of HA. This crystallographic structure of HA in the PASP/SF-HA composite was more similar to natural bone mineral. In addition, the organic components in the PASP/SF-HA composite also showed a diffraction peak at 20.2° (2θ) in Figure 3d, which assigned to the β-sheet structure of SF. These results were consistent with the analysis of FTIR.

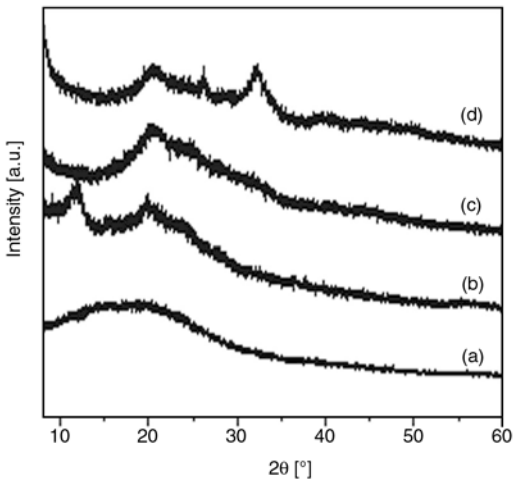

Figure 3. X-ray diffraction of (a) SF, (b) PASP/SF, (c) PASP/SF with the treatment of 60% (v/v) ethanol aqueous solution, and (d) the mineralized scaffolds at 37°C. The blend ratio of PASP/SF solution was 10% (w/w)

3.3. SEM

The surface morphology of the prepared materials is shown in Figure 4. After addition of PASP, the surface of SF films became rough (Figure 4A: b, c, d). Through the alternate soaking in $CaCl_2$ and K_2HPO_4 solutions at 37°C, some inorganic compounds attached to the film surface and much aggregation occurred with increasing content of PASP. When the blend ratio of PASP reached 15%, a smooth porous surface was formed (Figure 4B: d). Figure 4C shows the SEM images of the scaffolds soaked in 1.5 SBF at 37°C for 24 h. The scaffolds formed highly interconnected and porous structure. The general size of the pores got to the maximum with 5% (w/w) blend ratio of PASP and higher content PASP resulted in the formation of needle-like apatite assembled into clusters. These results indicated that the composite films could become more homogeneous along with the increasing content of PASP, which could enhance the deposition of apatite. The ICP results of PASP/SF-HA shown in Table 2 also demonstrated the Ca/P molar ratio in the scaffolds increased gradually along with addition of PASP. When HA deposited on the pure SF films, the Ca/P molar ratio was only 1.38. How-

Table 2. ICP results from the PASP/SF-HA composite

PASP/SF	Element contents in the sample solution*		
	Ca [mg/l]	P [mg/l)	Ca/P
100/0	43.28	24.24	1.38
95/5	53.16	41.20	1.39
90/10	56.74	30.50	1.44
85/15	56.81	30.37	1.45

*All samples are of the same quality

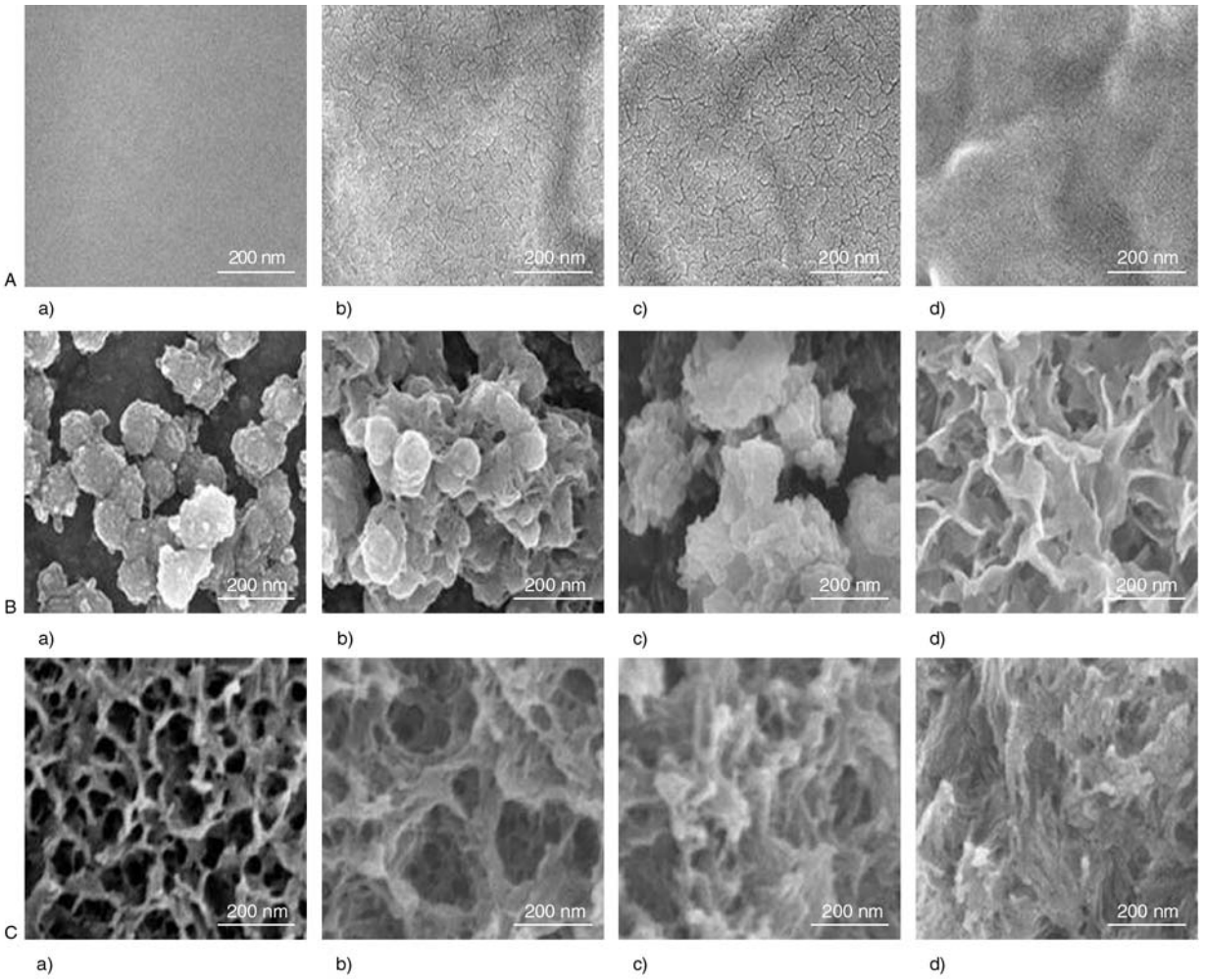

Figure 4. SEM images of the scaffolds (A) prepared from various blend ratios of PASP/SF solutions, (B) after soaking in $CaCl_2$ and K_2HPO_4 solutions at 37°C, and (C) followed by being soaked in 1.5 SBF at 37°C for 24 h (a: 0%; b: 5%; c: 10%; d: 15%)

ever, it increased to 1.45 when the blend ratio of PASP/SF reached 15% (w/w). As the proportion of PASP in the blend membranes increased, the content of Ca in the composite solution also increased clearly. These results in this study proved that apatite had been deposited on the SF substrates successfully. The carbonyl group of PASP enhanced apatite deposition on membranes [18, 26].

4. Conclusions

The PASP/SF-HA composites were fabricated through a simple pretreatment and biomimetic method. The addition of PASP and treatment of ethanol greatly influenced the molecular conformation of SF. Intermolecular hydrogen bonds between the carbonyl group of PASP and the polarity group of SF played important roles in the formation of the PASP/SF-HA composite. The present study may further enhance the understanding of biomineralization and promote the development of new biomaterials for bone tissue engineering.

Acknowledgements

The authors gratefully acknowledge the support of Natural Science Fund of Anhui Province (Grant Number: 070414193), and the fund support of Key Laboratory of Environment-friendly Polymer Materials of Anhui Province.

References

[1] Dorozhkin S. V., Epple M.: Biological and medical significance of calcium phosphates. Angewandte Chemie International Edition, **41**, 3130–3146 (2002). DOI: 10.1002/1521-3773(20020902)41:17<3130::AID-ANIE3130>3.0.CO;2-1

[2] Ducheyne P., Qiu Q.: Bioactive ceramics: The effect of surface reactivity on bone formation and bone cell function. Biomaterials, **20**, 2287–2303 (1999). DOI: 10.1016/S0142-9612(99)00181-7

[3] Sikavitsas V. I., Bancroft G. N., Mikos A. G.: Formation of three-dimensional cell/polymer constructs for bone tissue engineering in a spinner flask and a rotating wall vessel bioreactor. Journal of Biomedical Materials Research, **62**, 136–148 (2002). DOI: 10.1002/jbm.10150

[4] Ochi K., Chen G. P., Ushida T., Gojo S., Segawa K., Tai H., Ueno K., Ohkawa H., Mori T., Yamaguchi A., Toyama Y., Hata J-I., Umezawa A.: Use of isolated mature osteoblasts in abundance acts as desired-shaped bone regeneration in combination with a modified poly-DL-lactic-co-glycolic acid (PLGA)-collagen sponge. Journal of Cellular Physiology, **194**, 45–53 (2003). DOI: 10.1002/jcp.10185

[5] Yamada Y., Boo J. S., Ozawa R., Nagasaka T., Okazaki Y., Hata K., Ueda M.: Bone regeneration following injection of mesenchymal stem cells and fibrin glue with a biodegradable scaffold. Journal of Cranio-Maxillofacial Surgery, **31**, 27–33 (2003). DOI: 10.1016/S1010-5182(02)00143-9

[6] Rocha L. B., Goissis G., Rossi M. A.: Biocompatibility of anionic collagen matrix as scaffold for bone healing. Biomaterials, **23**, 449–456 (2002). DOI: 10.1016/S0142-9612(01)00126-0

[7] Pulapura S., Kohn J.: Tyrosine-derived polycarbonates: Backbone-modified 'pseudo'-poly(amino acids) designed for biomedical applications. Biopolymers, **32**, 411–417 (1992). DOI: 10.1002/bip.360320418

[8] Pins G. D., Huang E. K., Christiansen D. L., Silver F. H.: Effects of static axial strain on the tensile properties and failure mechanisms of self-assembled collagen fibers. Journal of Applied Polymer Science, **63**, 1429–1440 (1997). DOI: 10.1002/(SICI)1097-4628(19970314)63:11<1429::AID-APP5>3.0.CO;2-O

[9] Park S. J., Lee K. Y., Ha W. S., Park S. Y.: Structural changes and their effect on mechanical properties of silk fibroin/chitosan blends. Journal of Applied Polymer Science, **74**, 2571–2575 (1999). DOI: 10.1002/(SICI)1097-4628(19991209)74:11<2571::AID-APP2>3.0.CO;2-A

[10] Liu L., Liu J. Y., Wang M. Q., Min S. J., Cai Y. R., Zhu L. J., Yao J.M.: Preparation and characterization of nano-hydroxyapatite/silk fibroin porous scaffolds. Journal of Biomaterials Science, Polymer Edition, **19**, 325–338 (2008). DOI: 10.1163/156856208783721010

[11] Kong X. D., Cui F. Z., Wang X. M., Zhang W.: Silk fibroin regulated mineralization of hydroxyapatite nanocrystals. Journal of Crystal Growth, **270**, 197–202 (2004). DOI: 10.1016/j.jcrysgro.2004.06.007

[12] Wang L., Nemoto R., Senna M.: Changes in microstructure and physico-chemical properties of hydroxyapatite-silk fibroin nanocomposite with varying silk fibroin content. Journal of the European Ceramic Society, **24**, 2707–2715 (2004). DOI: 10.1016/j.jeurceramsoc.2003.09.006

[13] Nam J., Park Y. H.: Morphology of regenerated silk fibroin: Effects of freezing temperature, alcohol addition, and molecular weight. Journal of Applied Polymer Science, **81**, 3008–3021 (2001). DOI: 10.1002/app.1751

[14] Chen X., Knight D. P., Shao Z. Z.: β-turn formation during the conformation transition in silk fibroin. Soft Matter, **5**, 2777–2781 (2009). DOI: 10.1039/b900908f

[15] Chen X., Li W. J., Yu T. Y.: Conformation transition of silk fibroin induced by blending chitosan. Journal of Polymer Science Part B: Polymer Physics, **35**, 2293–2296 (1997). DOI: 10.1002/(SICI)1099-0488(199710)35:14<2293::AID-POLB9>3.0.CO;2-X

[16] Yang G., Zhang L., Peng T., Zhong W.: Effects of Ca^{2+} bridge cross-linking on structure and pervaporation of cellulose/alginate blend membranes. Journal of Membrane Science, **175**, 53–60 (2000). DOI: 10.1016/S0376-7388(00)00407-5

[17] Liang C. X., Hirabayashi K.: Improvements of the physical properties of fibroin membranes with sodium alginate. Journal of Applied Polymer Science, **45**, 1937–1943 (1992). DOI: 10.1002/app.1992.070451108

[18] Kim H. J., Kim U-J., Kim H. S., Li C. M., Wade M., Leisk G. G., Kaplan D. L.: Bone tissue engineering with premineralized silk scaffolds. Bone, **42**, 1226–1234 (2008). DOI: 10.1016/j.bone.2008.02.007

[19] Li Y. C., Cai Y. R., Kong X. D., Yao J. M.: Anisotropic growth of hydroxyapatite on the silk fibroin films. Applied Surface Science, **255**, 1681–1685 (2008). DOI: 10.1016/j.apsusc.2008.06.009

[20] Yang G., Zhang L. N., Liu Y. G.: Structure and microporous formation of cellulose/silk fibroin blend membranes: I. Effect of coagulants. Journal of Membrane Science, **177**, 153–161 (2000). DOI: 10.1016/S0376-7388(00)00467-1

[21] Simonetti M., Di Bello C.: New Fourier transform infrared based computational method for peptide secondary structure determination. I. Description of method. Biopolymers, **62**, 95–108 (2001). DOI: 10.1002/bip.1002

[22] Cai X., Tong H., Shen X. Y., Chen W. X., Yan J., Hu J. M.: Preparation and characterization of homogeneous chitosan-polylactic acid/hydroxyapatite nanocomposite for bone tissue engineering and evaluation of its mechanical properties. Acta Biomaterialia, **5**, 2693–2703 (2009). DOI: 10.1016/j.actbio.2009.03.005

[23] He S-J., Valluzzi R., Gido S. P.: Silk I structure in Bombyx mori silk foams. International Journal of Biological Macromolecules, **24**, 187–195 (1999). DOI: 10.1016/S0141-8130(99)00004-5

[24] Kratky O., Schauenstein E., Sekora A.: An unstable lattice in silk fibroin. Nature, **165**, 319–320 (1950). DOI: 10.1038/165319a0

[25] Tao W., Li M. Z., Zhao C. X.: Structure and properties of regenerated Antheraea pernyi silk fibroin in aqueous solution. International Journal of Biological Macromolecules, **40**, 472–478 (2007). DOI: 10.1016/j.ijbiomac.2006.11.006

[26] Garcia-Fuentes M., Giger E., Meinel L., Merkle H. P.: The effect of hyaluronic acid on silk fibroin conformation. Biomaterials, **29**, 633–642 (2008). DOI: 10.1016/j.biomaterials.2007.10.024